Development of Energy Efficient Membrane Distillation Systems

by

Edward K. Summers

S.M., Massachusetts Institute of Technology (2010)
S.B., Massachusetts Institute of Technology (2008)

ARCHIVES
MASSACHUSETTS INSTITUTE OF TECHNOLOGY
JUN 25 2013
LIBRARIES

Submitted to the Department of Mechanical Engineering
in partial fulfillment of the requirements for the degree of

Doctor of Philosophy

at the

MASSACHUSETTS INSTITUTE OF TECHNOLOGY

June 2013

© Massachusetts Institute of Technology 2013. All rights reserved.

Author .....
Department of Mechanical Engineering
May 16, 2013

Certified by .....
John H. Lienhard V
Collins Professor of Mechanical Engineering
Thesis Supervisor

Accepted by .....
David E. Hardt
Graduate Officer, Department of Mechanical Engineering

Development of Energy Efficient Membrane Distillation Systems

by

Edward K. Summers

Submitted to the Department of Mechanical Engineering
on May 16, 2013, in partial fulfillment of the
requirements for the degree of
Doctor of Philosophy

Abstract

Membrane distillation (MD) has shown potential as a means of desalination and water purification. As a thermally driven membrane technology which runs at relatively low pressure, which can withstand high salinity feed streams, and which is potentially more resistant to fouling, MD could be used for desalination where reverse osmosis is inadequate. The use of thermal energy, and the ease of construction at small scale, makes this technology attractive for off-grid or renewable power applications as well.

However, most research on MD has focused on maximizing purified water output per unit of membrane area as opposed to minimizing system energy consumption and cost. Current MD systems suffer from poor energy efficiency, with reported performance rarely exceeding that of a simple solar still.

This thesis explores means to optimize the design of MD for energy efficiency to make it competitive with existing thermal desalination systems, with particular focus on the Air Gap Membrane Distillation (AGMD) configuration. A detailed 1D numerical model to explore the effect of design parameters on energy efficiency was developed. Means to enhance energy recovery from hot discharge brine without additional brine concentration, and reduce diffusion resistance by means of reducing pressure in the air gap were explored. A novel configuration delivering solar flux directly to the membrane, and multi-stage, multi-pressure configurations comparable to MSF were also developed. A parameter to relate the performance of a bench-scale experiment with similar membrane and gap size to a production system was developed and validated.

Small scale experiments were conducted to verify performance for the novel solar powered configuration, reduced gap pressure, and capturing energy from hot discharge brine. Experiments demonstrated the efficacy of a solar absorbing membrane to provide heat to the cycle, and established a benefit of deforming the membrane

into the gap under hydraulic pressure; reducing gap size and measurably improving performance. Parametric studies have shown the effectiveness of using the model to design larger, more practical, competitive systems; establishing the importance of long flow lengths, low mean membrane flux, and large membrane area in the design of efficient MD systems.

Thesis Supervisor: John H. Lienhard V
Title: Collins Professor of Mechanical Engineering

Acknowledgments

Thank you to my advisor, Prof. John Lienhard V, for his guidance, and to my labmates, who were always willing to discuss ideas and offer advice.

Thank you to my thesis committee, Prof. Alexander Mitsos, Prof. Gregory Rutledge, and Prof. Hassan Arafat, for providing valuable feedback over the course of my research.

Also, to the Masdar Institute for funding this project and assuring I got a paycheck.

Thank you to our co-collabrators at Masdar, Prof. Hassan A. Arafat, Rasha Saffarini, Elena Guillen, and Mohamed Ali for contributing to this work in various respects.

And lastly to my friends and family for their patience and support throughout my time here at MIT.

Contents

List of Figures

List of Tables

Nomenclature

Roman Symbols

B	Membrane distillation coefficient or membrane flux coefficient [kg/m^{2}Pa s]
c	Vapor concentration [mol/m^3]
c_0	Speed of light [m/s]
c_p	Specific heat capacity at constant pressure [J/kg K]
d_{gap}	Air gap width [m]
dA	Differential area element [m^2]
dz	Differential module length [m]
g	Acceleration of gravity [m/s^2]
h	Enthalpy [J/kg]
h_t	Convective heat transfer coefficient [W/m^{2}K]
h_{fg}	Latent Heat of Evaporation [J/kg]
h_{pl}	Planck's constant [J s]
I	Irradiation [W/m^2]
I_r	Irradiance [W/m^2 nm]
J	Vapor flux [kg/m^{2}s]
k	Thermal conductivity [W/m·K]
k_b	Boltzmann's Constant [J/K]
K_{ext}	Glazing extinction coefficient [1/m]
$\dot{m}$	Mass Flow Rate [kg/s]
n	Index of refraction

P	Total pressure [Pa]
p	Partial pressure [Pa]
$\bar{q}_{loss}$	Average heat loss across a membrane module [W/m^2]
Q	Heat flow [W]
q	Heat flux [W/m^2]
RR	Recovery Ratio
r	Reflectance
S	Solar radiation flux absorbed by the membrane [W/m^2]
S_f	Solar radiation flux absorbed by the bulk feed stream [W/m^2]
TTD	Heat exchanger terminal temperature difference [K]
T	Temperature [K]
U_t	Overall heat loss coefficient [W/m^{2}K]
v	Specific volume [m^3/kg]
w	Membrane width [m]
x	Mole Fraction
z	Lengthwise Coordinate

Greek Symbols

$(\tau\alpha)$	Transmission-absorption product
α	Absorptivity
α	Thermal diffusivity [m^2/s]
ΔT_{flash}	Saturation temperature difference between stages [K]
ΔT_{htr}	Temperature rise across the heater [°C]
ΔT_{lm}	Log-mean temperature difference [K]
δ	Thickness [m]
ϵ	Heat exchanger effectiveness
λ	Wavelength [nm]
ν	Kinematic viscosity [m^2/s]

ω	Humidity ratio [kg water/kg dry air]
ρ	Density [kg/m^3]
ρ	Reflectivity
θ	Beam angle [rad]
τ	Transmissivity
ξ	Porosity

Subscripts

a	Air gap
abs	Absorber
air	Air
b	Bulk flow
bl	Blackbody
c	Condenser stream
$c1$	Inner cover
$c2$	Outer cover
$cond$	Condenser cooling water
$conv$	Convective heat transfer
exp	Isothermal expansion
f	Feed
gl	Glazing material
i	Condensate film interface
in	In
l	Liquid phase
m	Membrane
max	Maximum
out	Out
$\parallel$	Beam component parallel to surface

$\perp$	Beam component perpendicular to surface
p	Permeate
p, c	Condensed permeate in a liquid phase
rad	Radiative heat transfer
rej	Brine rejected to environment
sat	Saturation
$stack$	Glazing stack
SW	Seawater
v	Vapor
w	Water
$wall$	Condenser wall
WM	Warmed brine exiting regenerative heat exchanger

Chapter 1

Introduction

Currently many areas of the world suffer from a scarcity of fresh water. Despite the fact that the world is over 2/3 water, the vast majority of it is too salty for human consumption. According to the International Water Management Institute [1] many areas of the world have severe physical water scarcity, as shown in Figure 1-1 [1].

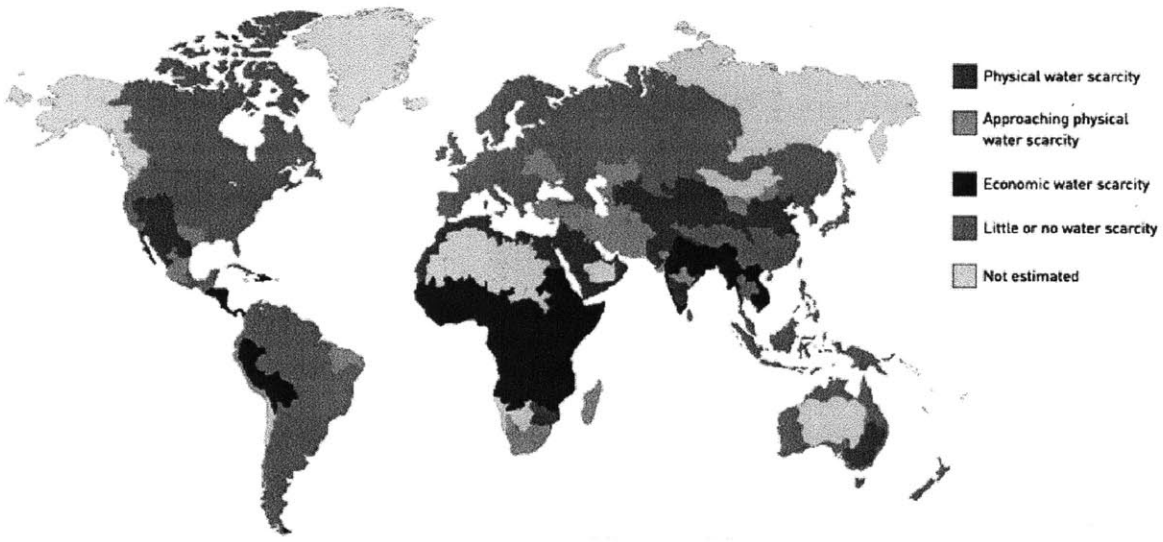

Figure 1-1: World map detailing physical and economic water scarcity in 2006 [1].

As the human population grows this problem is only going to be compounded. Desalination can provide a means of expanding the world's supply of fresh water. However, desalination technologies run up against myriad technical and economic challenges. The most common means of desalination, Reverse Osmosis [2] is gener-

ally considered the most efficient, and works by mechanically forcing water through salt-impermeable membranes against the osmotic pressure gradient. These systems, however, suffer from high complexity, high capital cost, and a limitation on feed stream salinity where feed streams generally do not exceed 45,000 ppm of dissolved solids [3]. Thermal technologies, popular in the Middle East [2] where thermal energy is more readily available can process a variety of brines, but suffer from fouling and scaling limitations [4].

Therefore, there is a need to develop desalination systems that overcome these barriers, but are also scalable in output and cost efficient, and can be deployed in a variety of areas that do not necessarily have access to large municipal water distribution infrastructure or the means to maintain a technically complex system. Technologies that can work in combination with existing desalination processes would also make desalination more accessible to areas suffering from both economic and physical water scarcity.

1.1 Membrane Distillation

Membrane Distillation (MD) is such a technology that could potentially increase the use and accessibility of desalination.

Membrane distillation is a separation process in which a hot feed stream is passed over a microporous hydrophobic membrane. The temperature difference between the two sides of the membrane leads to a vapor pressure difference that causes water to evaporate from the hot side and, pass through the pores to the cold side. The vapor is pure water which can be condensed. This process has application to desalting water. Compared to reverse osmosis, MD does not require a high pressure feed, and can process very high salinity brines. Compared to other large thermal processes, it can be easily scaled down. Demonstrated pilot plants have been used at a small scale (0.1 m^3/day), including stand-alone systems disconnected from municipal power or water networks [5, 6, 7].

MD systems can be used in many configurations, depending on how liquid is col-

lected from the permeate side. In direct contact MD (DCMD), the vapor is condensed on a pure water stream that contacts the other side of the membrane. In air gap MD (AGMD), an air gap separates the membrane from a cold condensing plate which collects vapor that moves across the gap. In sweeping gas MD (SGMD), a carrier gas is used to remove the vapor, which is condensed in a separate component. SGMD is typically used for removing volatile vapors and is typically not used in desalination [8]. In vacuum MD (VMD), the permeate side is kept at lower pressure to enhance the pressure difference across the membrane, and condensation may occur in the module, or in an external condenser. All the different configurations of MD can be applied to seawater and brackish water desalination [8, 9]; however, those most commonly used for desalination are DCMD, AGMD, and VMD.

Most research on MD desalination focuses on maximizing membrane flux, or vapor produced per unit area of membrane. However some studies have examined energy efficiency for experimental plants at the 0.1 m^3/day scale [5, 6]. Additionally, more recent MD desalination studies have also examined energy efficiency [5, 10, 11, 12]. Using membrane flux as a proxy for thermal performance may not lead to the correct conclusion about overall system performance, as fresh water output and energy consumption can be highly dependent on system configuration, membrane area, system top temperature, and heat recovery from hot brine and condensing vapor. In a complete cycle, the highest flux may not lead the best use of energy, as it often requires high heat inputs and the resulting high vapor flux can increase resistance to heat and mass transfer, driving up energy use.

Few direct comparisons have been made between the different configurations of MD: DCMD, AGMD, VMD. Studies that have compared different configurations have focused on the processes in the MD module, instead of full thermal cycle performance. Cerneaux et al. [13] compared heat and mass transfer processes and total flux over ceramic MD membranes in DCMD, AGMD, and VMD. Alkalibi and Lior compared flux over different MD configurations (including SGMD) [14] and expanded their analysis to include heat and mass transfer characteristics [15]. Ding et al. [16] examined the removal of ammonia from water using MD with a focus on flux and

chemical concentrations. However, no studies have examined MD in the context of a full desalination cycle, where energy recovery is highly important to the viability of a desalination process. Therefore, evaluation of MD in this thesis will be focused on energy efficiency.

1.1.1 Characteristics of MD

DCMD systems in desalination have been studied fairly extensively. While they have good salt rejection, they suffer high trans-membrane heat loss, and consequently low membrane flux. Typical DCMD systems, tested with NaCl solutions between 35,000 and 100,000 ppm, have achieved a membrane flux from 1-10 L/m^{2}hr [17, 18, 19]. The biggest disadvantage of these systems is that the cool water on the permeate side results in large conductive heat losses through the thin membrane.

AGMD typically has slightly higher flux for similar temperature conditions, as the air gap provides thermal insulation between the hot feed and cold condenser water. However, resistance to mass flux is limited by diffusion across the air gap and evaporation through the pores, which is also dependent on the pore size and the resultant trans-membrane diffusion mechanism. Condensate film thickness is typically 10 times thinner than the air gap width [14]. Fluxes for AGMD systems operating near 70 °C inlet feed temperature range have been reported from 10 L/m^{2}hr [14, 6] up to 65 L/m^{2}hr [13]. This type of system is most commonly used in pilot-scale desalination systems [20].

VMD has the best performance in terms of flux as a result of enhancement by the mechanical pressure difference. One system operating at a high temperature of 85 °C [21] achieved a flux of 71 L/m^{2}hr. A second system [13] was able to achieve a consistent flux of 146 L/m^{2}hr operating at 300 Pa on the permeate side and with a 40 °C feed inlet temperature. A third system [22] made use of turbulent feed flow and vacuum to enhance flux, achieving 40 L/m^{2}hr. The applied vacuum on the permeate side was roughly half an atmosphere, which can easily be achieved without expensive pumps and pressure vessels. This indicates that a mechanically applied pressure difference is more advantageous when using VMD systems. In cases where

fouling is a concern, mechanical pressure enhancement can keep feed temperatures low while still achieving high flux.

SGMD relies on a sweeping gas to entrain water vapor. It is typically not used in desalination as the latent heat is not given up into the air stream, and adding moisture to an air stream results in an increase in enthalpy without necessarily increasing the bulk temperature. This makes it hard to recover energy from the permeate stream, as the moist air sometimes exits close to, or below, the seawater inlet temperature, requiring additional cooling to create the appropriate temperature gradient to transfer heat into the feed stream. The requirement for external cooling has made this cycle too complex and expensive to be realized for desalination, where energy recovery is crucial.

1.1.2 Previous Work

Compared to real-world desalination processes, current MD desalination systems suffer from poor energy efficiency. Energy efficiency in this paper will be measured by the gained output ratio, or GOR, defined in Equation 1.1.

$$\text{GOR} = \frac{\dot{m}_p h_{fg}}{Q_{in}} \tag{1.1}$$

GOR is the ratio of the latent heat of evaporation of a unit mass of product water to the amount of energy used by a desalination system to produce that unit mass of product. The higher the GOR, the better the performance, as the energy used for evaporation is recovered and recycled multiple times. Amongst thermal systems, a solar still would have a a GOR on the order of 0.5 [23], whereas a good Multi-Effect Distillation system may have a GOR of 12 [24]. Table 1.1 shows the GOR values of existing experimentally tested MD systems with operating conditions when available.

GOR is directly proportional the recovery ratio (RR), or the amount fresh water produced per unit feed that enters the system, Equation 1.2 describes the recovery ratio:

$$\mathrm{RR} = \frac{\dot{m}_p}{\dot{m}_f} \tag{1.2}$$

Considering the heat input, Q_{in}, can be written as the temperature rise of the feed as it passes through the heater, or ΔT_{htr}, and the capacity rate of the feed, the GOR can then be written in terms of the recovery ratio and temperature rise required through the heater:

$$\mathrm{GOR} = \mathrm{RR}\frac{h_{fg}}{c_p}\frac{1}{\Delta T_{htr}} \tag{1.3}$$

In addition to increasing energy recovery in a system, improving GOR also involves improving system recovery ratio by increasing water production or decreasing the amount of feed flow rate required, thereby reducing load on the heater.

Table 1.1: GOR and operating conditions of existing single-stage MD desalination systems. "SP" denotes solar powered systems. Operating conditions listed if given.

System	Type	GOR	Operating Condition
Banat et al. (2007) [7]	AGMD (SP)	0.9	Clear sky, 40.11 kWh/day absorbed energy, 7 m^2 memb. area
Fath et al. (2008) [6]	AGMD (SP)	0.97	Clear sky, T_{top} = 60-70 °C, 7 m^2 area, T_{bot} = 40-50 °C, 0.14 kg/sec low rate, Seawater
Guillen-Burrieza et al. (2011) [5]	AGMD (SP)	0.8	T_{top}= 80 °C+ , 20.1 L/min (0.33 kg/s) feed flow rate, 5.6 m^2 memb. area, 2 modules in series, 35,000 PPM feed salinity
Criscuoli (2008) [25]	VMD	0.57	40 cm^2 memb. area, 1 kPa permeate pressure
Wang et al. (2009) [26]	VMD (SP)	0.85	
Criscuoli (2008) [25]	DCMD	0.17	40 cm^2 memb. area
Lee et al. (2011) [11]	DCMD	4.1	0.5 L/min (0.008 kg/sec) feed flow rate, T_{top} = 90 °C, 0.4 m^2 memb. area (per stage), 8 stages in series
Zuo et al. (2011) [10]	DCMD	1.4	0.04 m/s Feed, 0.48 m/s permeate (hollow fiber, permeate on shell side), T_{top}=90 °C, 10 m^2 area, T_{bot}= 25 °C, 30,000 PPM feed salinity

Most experimental systems have achieved a GOR of around 1. Larger membrane areas have achieved higher GOR values. With the limited amount of data on VMD systems reported GORs remain rather low, below 1, when compared to tested DCMD and AGMD designs. A wide range of GOR for each type of system shows the dependence on configuration and operating conditions. The systems are all at prototype scale, with an output of 0.1-1 m^3/day. These results show the need for additional insight on how the design of each type of MD configuration affects the thermal performance, which would in turn affect water cost.

Renewable Powered Systems

Solar powered desalination has the potential to provide a solution for arid, water-scarce regions that also benefit from sunny climates, but which are not connected to municipal water and power distribution networks that are necessary for the most common large-scale desalination systems. Solar energy is a natural way provide heating energy or electrical power to a small scale system that must run independent of any other infrastructure.

The most common form of solar desalination is a solar still. Solar stills are simple to build, but inherently do not recycle energy as water condenses on a surface that rejects heat to the ambient environment [23]. Another option of this type is solar powered reverse osmosis. While more energy efficient than any thermal based system, it requires expensive components which are expensive to maintain. RO membranes experience high pressures and can easily be damaged by substances commonly found in seawater, therefore pretreatment is required. As a result, high cost and complexity make these systems unattractive for off-grid or developing world applications.

However, renewable-powered MD systems which have been built currently have poor energy efficiency. When measured by the gained output ratio (GOR) these systems do not exceed the performance of a simple solar still, which typically has a GOR of 0.5-1, as most solar stills do not usually employ energy recovery [27]. Systems with poor energy performance are generally costlier to run, especially if there is a large capital cost associated with solar collection [28]. Table 1.1 lists the

energy performance of existing renewable energy powered MD systems, denoted by "SP".

1.2 AGMD: Advantages and Potential for Improvement

Of all the systems commonly used for desalination, air gap membrane distillation (AGMD) shows the strongest potential for improvement. GORs of current AGMD systems tend to be lower than for other systems, and the insulation properties of the air gap prevent direct thermal loss between hot and cold sides. The built in condenser surface allows fluid to be condensed at the local saturation temperature instead of being mixed and condensed at the mean saturation temperature as in a VMD system. Creative design improvements and optimization could potentially make AGMD competitive with more established thermal desalination systems.

Chapter 2

Analytical Models of MD

2.1 Introduction

Detailed modeling of the transport processes in an MD module is the first step toward complete cycle modeling, and allows for the identification of performance limiting processes at different operating conditions.

Existing analytical models for MD systems were adapted to be solved numerically (discretized) using a finite difference method. The membrane id divided along its length, L, in the flow direction, into discrete cells of length dz and width w, which multiplied make a differential area element, dA. Bulk flows serve as inputs and outputs for neighboring cells. An example cell of differential length for the feed side of any MD configuration with heat and mass flows illustrated is shown in Figure 2-1. In all cases a counter-flow configuration is used. A large system of equations, describing the heat and mass transfer interactions at each cell are combined with appropriate boundary conditions at the first and last cell and solved using Engineering Equation Solver (EES) [29]. EES is a simultaneous equation solver which uses a Newton iteration method to converge on the solution.

For AGMD, models by Liu et al. [30] and Rattner et al. [31] were used as a basis to solve to heat and mass transfer interactions across the cell. For DCMD a model by Bui et al. [32] was used. In the case of VMD, models that reflect steady-state operation were used, in which all air and other non-condensible gases have

been removed from the permeate side of the membrane module and the mole fraction of water vapor is close to 1. These formulations are similar to those of Mericq et al. [33] However instead of directly calculating membrane permeability, a constant membrane distillation coefficient is used representing the average values from several tested commercial membranes [34, 35, 36]. Properties for pure water [37] were used and evaluated at the temperature and pressure of the bulk flows in each cell. The models were validated with recent experimental data.

2.2 Common Model Elements

All MD configurations have a hydrophobic membrane which holds back the warm, saline feed stream. A control volume of the feed side and membrane is shown in Figure 2-1.

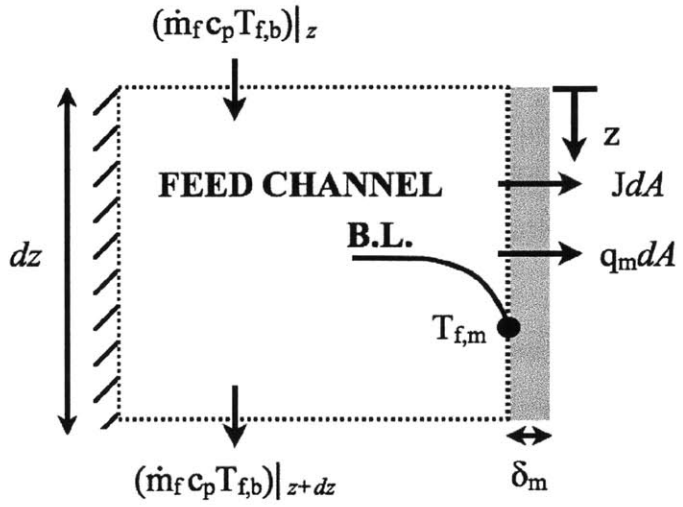

Figure 2-1: The feed (hot) side of any MD configuration with heat and mass fluxes labeled.

Mass transfer through the pores, J_m, is driven by a partial pressure difference between the water vapor on both sides. The total flux through any part of the membrane is defined by Equation 2.1:

$$J_m = B(p_{w,f,m} - p_{w,p,m}) \tag{2.1}$$

The vapor pressure of the water on the feed side at the membrane, $p_{w,f,m}$, is a known function of the temperature of the feed at the membrane, $T_{f,m}$, and the mole fraction of water in the feed at the membrane, $x_{w,f,m}$ (assuming an ideal solution).

$$p_{w,f,m} = p_{sat,w}(T_{f,m})x_{w,f,m} \tag{2.2}$$

The feed stream provides both the latent heat of evaporation, and any heat loss through the membrane; therefore, the temperature near the membrane surface is different from the bulk temperature due to the presence of a thermal boundary layer associated with the convection resistance through the fluid.

An energy balance on the feed stream results in Equation 2.3:

$$(\dot{m}_f h_{f,b})|_{z+dz} = (\dot{m}_f h_{f,b})|_z - (J_m h_{v,f,m} + q_m)dA \tag{2.3}$$

A mass balance on the feed side leads to the mass flow rate of the feed as function of length, which can vary appreciably over the total length of the module. However due to the low recovery ratio found in MD (on the order of 5%), this reduction in mass flow is small compared to the mass flow rate of the feed, but it is taken into account as a change in mass flow rate between successive cells in the numerical calculation.

$$\dot{m}_f|_{z+dz} = \dot{m}_f|_z - J_m dA \tag{2.4a}$$

$$d\dot{m}_f = -J_m dA \tag{2.4b}$$

Expanding the equation and using mass conservation from Equation 2.4:

$$d\dot{m}_f h_{f,b} + \dot{m}_f dh_{f,b} = -(J_m h_{v,f,m} + q_m) dA \tag{2.5a}$$

$$\dot{m}_f dh_{f,b} = -(J_m (h_{v,f,m} - h_{f,b}) + q_m) dA \tag{2.5b}$$

The vapor enthalpy, exiting the feed channel and passing into the membrane can be written in terms of the latent heat of fusion and the local liquid enthalpy which is equal to the saturated fluid enthalpy at that temperature:

$$h_{v,m} = h_{w,m} + h_{fg}(T_m) \tag{2.6}$$

The vapor enthalpy (Equation 2.6) can be used substituted into the energy balance to obtain the change in the enthalpy over a single cell.

$$\dot{m}_f dh_{f,b} = -\left[J_m (h_{fg} + h_{f,m} - h_{f,b}) + q_m\right] dA \tag{2.7}$$

where $dh_{f,b}$ is the bulk enthalpy difference in the positive z direction of the feed water, and q_m is the heat flux conducted through the membrane. The latent heat h_{fg} is evaluated at the local membrane temperature $T_{f,m}$. Convective heat transfer to the membrane surface is dependent on the speed of the flow and geometry of the flow channel. It can be evaluated with Equation 2.8:

$$J_m (h_{fg} + h_{f,m} - h_{f,b}) + q_m = h_{t,f}(T_{f,b} - T_{f,m}) \tag{2.8}$$

in which $T_{f,m}$, and $T_{f,b}$ are the temperatures of the membrane surface and bulk respectively at length-wise distance z. The convective heat transfer coefficient $h_{t,f}$ can be determined by established correlations for Nusselt number for either laminar or turbulent flow in any specific configuration and geometry [38].

Next, a control volume is taken around the membrane itself. Most of the energy that passes through the membrane is that carried by the mass flow and latent heat

of evaporation; however, heat is lost by conduction through the thin membrane. Heat can be conducted through the solid membrane surface in the solid (non-porous) portions, or through the water vapor in the pores as shown in Equation 2.9:

$$q_m = [k_m(1-\xi) + k_v\xi]\frac{1}{\delta_m}(T_{f,m} - T_{p,m}) \tag{2.9}$$

No mass is added or removed inside the membrane and all vapor flows out. Additionally it is assumed no condensation occurs in the pores.

2.3 Direct Contact MD

The membrane module as a whole is a counterflow device with the inflows and outflows as shown in Figure 2-2. Pure liquid water runs along the opposite side of the membrane, and provides a condensing surface for the vapor passing through the pores.

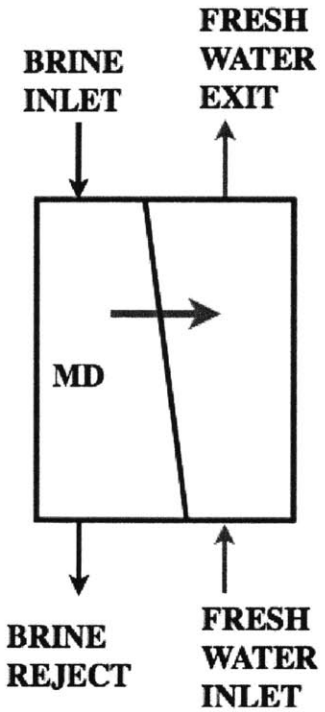

Figure 2-2: A simple counter flow DCMD module.

Taking a control volume on each side of the membrane, and the membrane itself, an energy and mass balance can be used to calculate all the necessary quantities. Figure 2-3 shows a control volume for one cell of length dz.

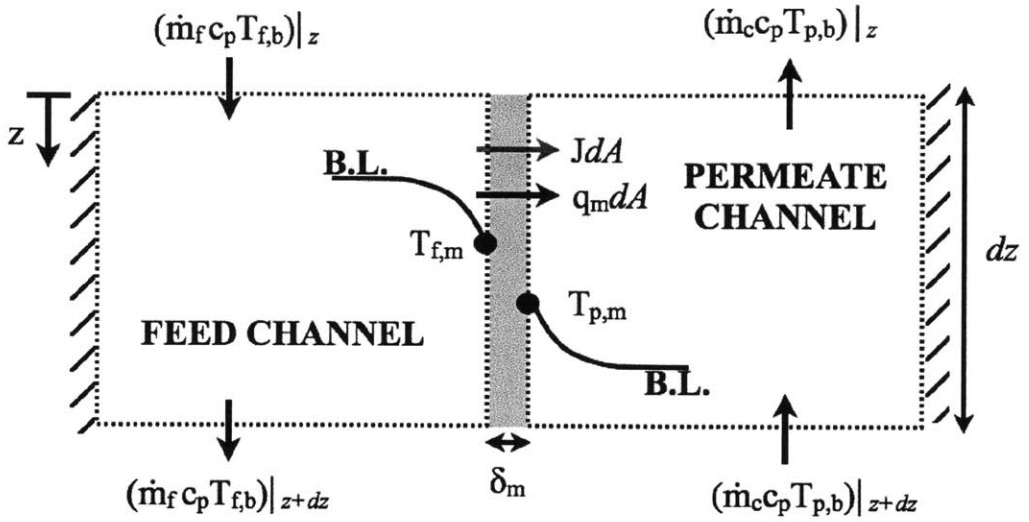

Figure 2-3: A control volume for a DCMD module cell.

The feed side, and membrane are modeled as described in the previous section, and the permeate side is very similar, as it is a liquid. The vapor pressure is the saturation pressure at the membrane temperature of the permeate stream. Since the stream is pure, the mole fraction is 1, and the expression reduces to Equation 2.10:

$$p_{w,p,m} = p_{sat,w}(T_{p,m}) \tag{2.10}$$

The permeate stream provides the condensing surface and accepts the condensed mass. An energy balance on the permeate stream results in Equation 2.11:

$$(\dot{m}_p h_{p,b})|_z = (\dot{m}_p h_{p,b})|_{z+dz} + (J_m h_{v,p,m} + q_m)dA \tag{2.11}$$

Since the condensate is absorbed into this stream, which flows counter to the feed, a mass balance leads to mass flow rate of the permeate as function of length.

$$\dot{m}_p|_z = \dot{m}_f|_{z+dz} + J_m dA \tag{2.12a}$$

$$d\dot{m}_p = -J_m dA \tag{2.12b}$$

Utilizing the same substitutions as those for the feed stream, and general definition of the vapor enthalpy:

$$\dot{m}_p dh_{p,b} = -\left[J_m(h_{fg} + h_{p,m} - h_{p,b}) + q_m\right] dA \tag{2.13}$$

where $dh_{p,b}$ is the enthalpy difference in the positive z direction of the permeate stream. Similar to the feed side, convection to the membrane surface is dependent on the speed of the flow and geometry of the flow channel. It can be determined with Equation 2.14:

$$J_m(h_{fg} + h_{p,m} - h_{p,b}) + q_m = h_{t,p}(T_{p,b} - T_{p,m}) \tag{2.14}$$

in which $T_{p,m}$, and $T_{p,b}$ are the temperatures of the membrane surface and bulk respectively at length-wise distance z.

2.4 Air Gap MD

In AGMD, the condensation process is also integrated in the module, but with an air gap of thickness d_{gap} on the order of 1 mm separating the coolant from the fresh water. In this case, seawater is also used as the coolant providing regeneration. An AGMD module with the inflows and outflows as shown in Figure 2-4.

Taking a control volume surrounding each side of the membrane, the membrane itself, and the air gap/condensate channel, an energy and mass balance can be used to calculate all the necessary quantities. Figure 2-5 shows a control volume for one cell of length dz.

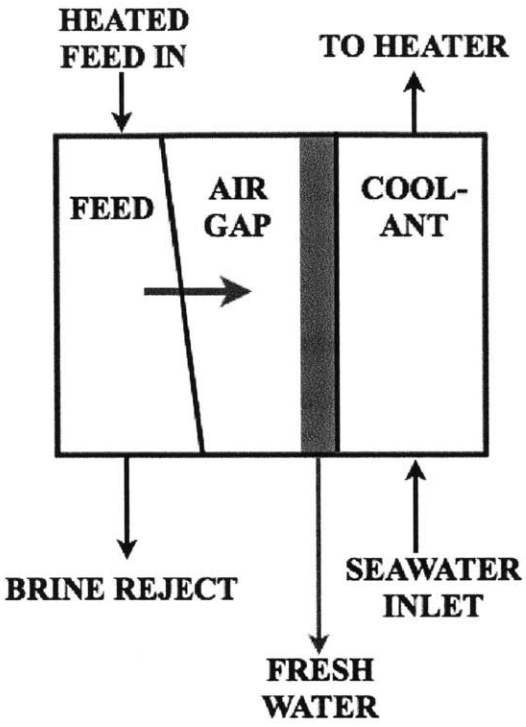

Figure 2-4: An AGMD membrane module with an integrated condenser.

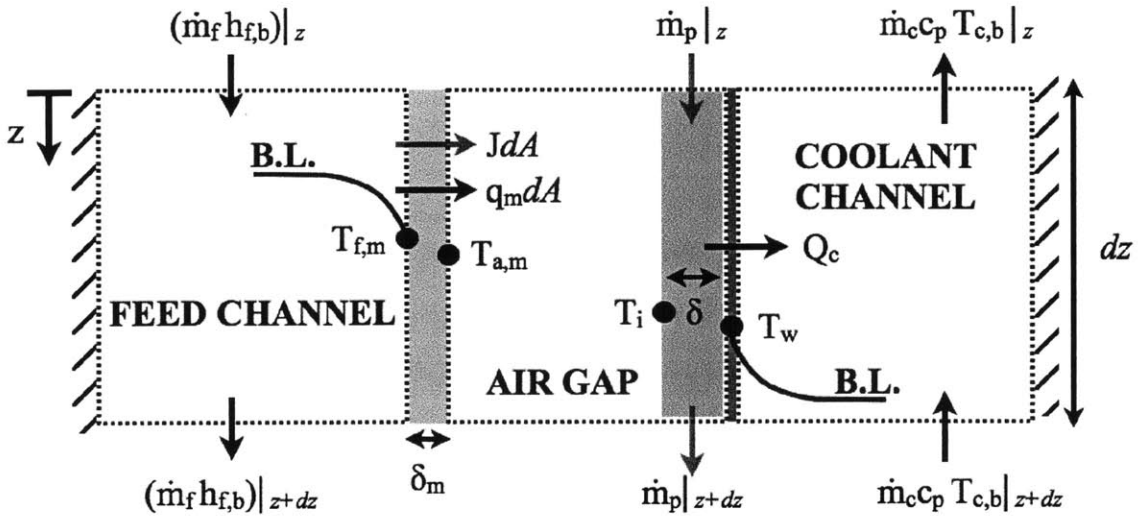

Figure 2-5: A control volume of an AGMD module cell.

The feed side and membrane are modeled as described the previous section. On the permeate side (air gap side), the partial pressure is a function of the mole fraction of water vapor present at the membrane surface and the total pressure on the permeate side, P_p.

$$p_{w,p,m} = P_p x_{w,p,m} \tag{2.15}$$

In the case of the systems modeled here, P_p is always atmospheric pressure. The mole fraction can be related to the common humidity ratio by Equation 2.16 [39].

$$x_{w,p,m} = \frac{\omega_{p,m}/0.622}{1 + \omega_{p,m}/0.622} \tag{2.16}$$

A control volume is taken around the air gap. Since the gap distance is very small ($d_{gap}/L_m \ll 1$ and $d_{gap}/w_m \ll 1$) convective flow, in the form of natural circulation, in the z direction is assumed to be negligible. The flow of permeate to the condenser surface is governed by binary diffusion across the gap as described by Equation 2.17 [40]:

$$\frac{J_m}{M_w} = \frac{c_a D_{w-a}}{d_{gap} - \delta} \ln\left(1 + \frac{x_i - x_{a,m}}{x_{a,m} - 1}\right) \tag{2.17}$$

In this formulation, it is assumed that no mass is transfered back through the membrane so that the flow of water vapor through the membrane is one way. With the temperatures of an MD process, it is unlikely that air will dissolve back into the water of the feed stream.

The flow of mass is dependent on the molar concentration, c_a, in the gap. This is approximated by treating the vapor-air mixture as an ideal gas at the mean cell temperature:

$$c_a = \frac{P_a}{\bar{R}(T_{a,m} + T_i)/2} \tag{2.18}$$

Energy flow into the air gap is limited by membrane conduction as described by Equation 2.9. While there is some energy released by sensible cooling of the vapor as it passes through the membrane and air gap, it is typically less than one percent of the membrane conduction q_m and a several orders of magnitude lower than the latent heat carried by the vapor. Therefore it is approximated to be zero. In the air gap, that energy is convected across the gap with the moving vapor, as described by Equation 2.20. Thermal radiation across the gap was considered, but found to have a negligible effect on flux and temperature, and was not included in this model. The convective heat transfer is easily derived by solving the energy equation where the convective velocity u is J_m/ρ_{mix}:

$$u\frac{dT}{dx} = \alpha\frac{d^2T}{dx^2} \tag{2.19}$$

where x in this case is the coordinate direction across the gap (not a mole fraction). Applying boundary conditions at the air side of the membrane (temperature and heat flux) and integrating twice the following equation is obtained:

$$T_{a,m} - T_i = \left(\frac{q_m}{k}\right)\frac{\alpha\rho}{J}\left[\exp\left(\frac{J}{\alpha\rho}(d_{gap} - \delta)\right) - 1\right] \tag{2.20}$$

All fluid properties are for the air/vapor mixture at the specific temperature in each cell.

The temperature of the condensate interface, T_i is determined by the partial pressure of water in air by solving Equation 2.2 at the interface where the mole fraction x_i is the ratio of the partial pressure of water vapor to the gap pressure P_a.

Upon entering the condensate layer the vapor gives up its latent heat, and the mass contributes to the thickening of the condensate layer. In gravity driven condensation, the layer thickness, δ, resists heat flow and is related to the mass of permeate

condensed by a simple laminar flow boundary layer equation [38]:

$$d\dot{m}_p = \frac{g(\rho_l - \rho_v)}{3\nu_l} w_m \left[(\delta + d\delta)^3 - \delta^3\right] \tag{2.21}$$

The heat conducted through the condensate layer is the sum of the heat conducted through the membrane, q_m, and the latent heat given up through condensation, evaluated at the interface temperature, T_i.

$$q_c = q_m + J_m h_{fg} \tag{2.22a}$$

$$q_c = \frac{k_w}{\delta}(T_i - T_{wall}) \tag{2.22b}$$

The condensate collects at the bottom of the module and the heat goes into the coolant stream. A boundary layer resistance in the coolant stream similar to that of the feed stream limits heat flow as described by Equation and 2.8. However, the heat that is absorbed into the condensate stream and passes through it's boundary layer is different, as no mass passes through the wall. The heat that enters the condensate stream is the sum of the membrane conduction, latent heat, and some sensible cooling of the liquid in the condensate layer.

$$\dot{m}_c dh_{p,b} = \left[q_c + J_m(h_{w,i} - h_{w,wall})\right] dA \tag{2.23}$$

Boundary layer resistance is described by:

$$q_c + J_m(h_{w,i} - h_{w,wall}) = -h_{t,c}(T_{c,b} - T_{wall}) \tag{2.24}$$

The heat transfer coefficient in the coolant stream, $h_{t,c}$, is calculated in the same way as that of the feed stream. The thermal resistances are comparable because of comparable mass flow rate and flow channel size.

2.5 Pumped Vacuum MD System

A pumped vacuum system is the most common type of VMD system. It consists of vapor extraction driven by a vacuum pump. Figure 2-6 show the flows in and out of a VMD module.

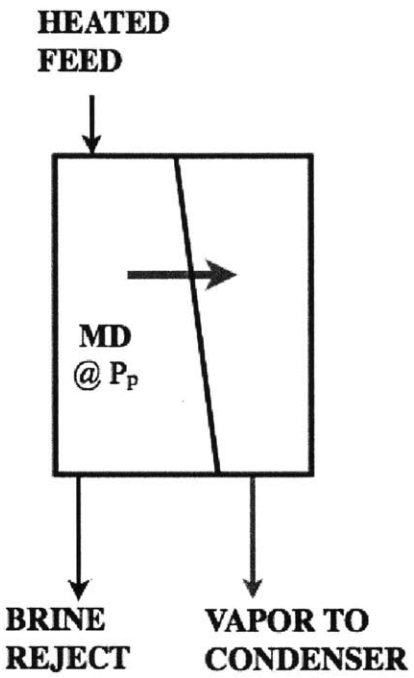

Figure 2-6: A VMD module where permeate is removed by a vacuum pump and condensed.

Unlike the AGMD system, where the air does not exit the system and can be maintained at a constant pressure, the vapor flow is driven by a vacuum pump. The pressure that the pump can achieve is inversely proportional to the flow rate of vapor from the module. This is obtainable from a pump curve. Since the vacuum pressure of the pump curve is a function of the total flow rate, integration of the permeate mass flow through the entire module is needed to find the vacuum pressure. Therefore, iteration is required to find the actual pressure.

During startup, the pump removes any air sitting in the module at a high rate, and the pump reaches steady state operation. During steady state, mass conservation dictates that only water vapor that enters through the membrane is removed (no air

leaks in an ideal case). Figure 2-7 shows a schematic drawing of a startup transient.

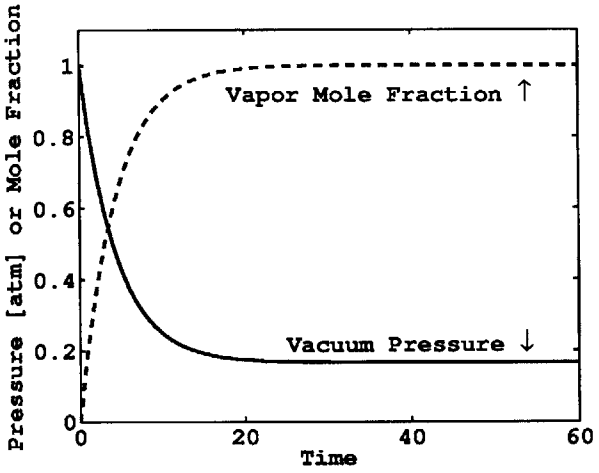

Figure 2-7: Schematic drawing of a startup curve showing the vacuum pressure and mole fraction of vapor on the permeate side of the module.

This model assumes that the process is running at a steady state such that:

$$J_m = B(p_{w,f,m} - P_p) \tag{2.25a}$$

$$\underbrace{P_p = f\left(\frac{J_m A_m}{\rho_v}\right)}_{\text{From Pump Curve}} \tag{2.25b}$$

The end result is that the flux is effectively dependent on the feed side temperature and the power of the pump. Since there is only vapor at reduced pressure on the permeate side, and the boundaries of the permeate chamber are adiabatic, no fogging is expected.

The feed side heat and mass transfer are calculated as described in the first section. However, on the permeate side there is no air at a lower temperature to conduct heat from the membrane, only vapor at $T_{f,m}$. As a result $T_{p,m} \approx T_{f,m}$ and $q_m \approx 0$. This is consistent with the very nearly isothermal expansion experienced by the water vapor as it passes through the pores, as the membrane thickness (minimum length of the pores) is about 1000 times the size of the nominal pore diameter. The heat flow that keeps the vapor isothermal, q_{exp}, is conducted though the solid parts of the membrane, and it may be calculated from the change in vapor enthalpy, h_v, using Equation 2.26:

$$q_{exp} = J_m \left[h_{f,m} + h_{fg} - h_v(P_p, T_{f,m}) \right] = RT_{f,m} \ln \left(\frac{v_{v,p,m}}{v_{v,f,m}} \right) \tag{2.26}$$

This heat of expansion is subtracted from the heat removed from the feed side control volume.

A boundary layer of moving vapor develops on the permeate side and the overall enthalpy of the vapor stream increases with additional membrane flux. A control volume representing this process is shown in Figure 2-8.

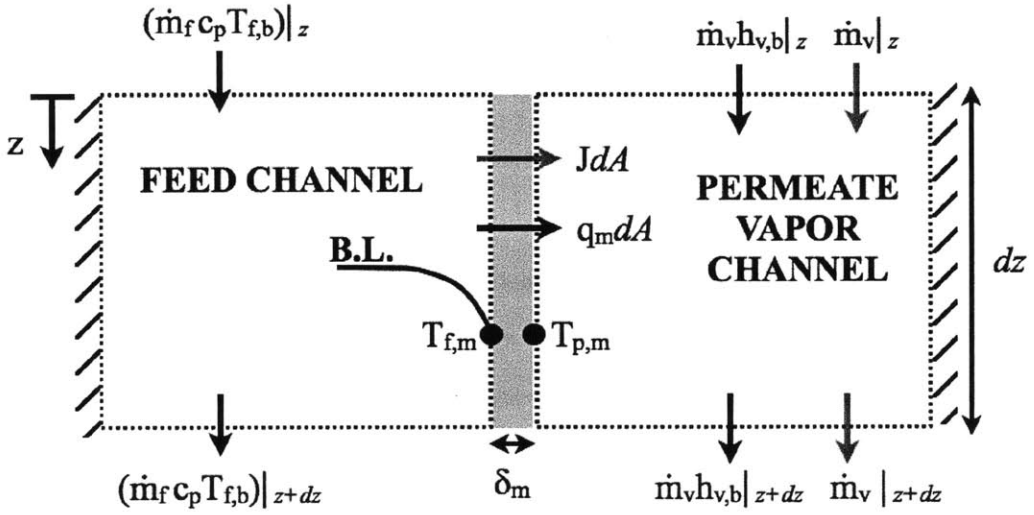

Figure 2-8: Control volume of a VMD membrane module cell.

Since no species other than water vapor is present in the permeate channel in steady state there, no concentration gradient is present to resist mass flow. Hence, the enthalpies of the streams combine according to Equation 2.27:

$$(\dot{m}_p h_{v,b})|_{z+dz} = (\dot{m}_p h_{v,b})|_z + J_m h_{v,m} dA \tag{2.27a}$$

$$\dot{m}_p|_{z+dz} = \dot{m}_p|_z + J_m dA \tag{2.27b}$$

2.6 Solution Method and Verification

The discretized numerical model was typically made up of several hundred cells with a set of equations describing the interactions from the hot-side to the cold-side bulk conditions at each cell. The resulting system can be upward of 10,000 equations solved simultaneously. Each of the cells encompass a finite length, and mass and heat flows are described by a single quantity for that length. A sufficient discretization to accurately describe the membrane could be obtained by increasing the number of cells (decreasing dz for given length) and observing a change in the output. For the longest membrane length, or largest values of the differential dz, the solution did not change in excess of 1/2% after the number of cells was increased to 260.

2.7 Model Validation

Models were evaluated numerically using parameters published in experimental studies of MD systems. The standard package Engineering Equation Solver [29] was used for calculations. Properties for pure water [37] were used and evaluated at the temperature and pressure of the bulk flows in each cell.

2.7.1 Direct Contact MD

Validation of the DCMD model was based on experiment done by Martinez-Diez and Florido-Diaz [35]. Table 2.1 shows given parameters provided as inputs for the model. The membrane distillation coefficient was not reported and was only implied by the experimental results, however for the purposes of validation, a value of B for the same type of membrane measured by Vazquez-Gonzalez and Martinez [36] was used.

Table 2.1: Operating parameters from Martinez-Deiz [35]. Starred parameters are compared with model for validation.

Given Parameter	Value
Feed/Permeate Flow Rate	*Various*
Feed Temp. (Inlet/Outlet Average)	45 °C
Permeate Temp. (Inlet/Outlet Average)	35 °C
Length	55 mm
Channel Width	7 mm
Channel Depth	0.4 mm
Membrane Type	Gelman Inst. TF200 PTFE
Membrane Distillation Coeff. (Measured, [36])	22×10^{-7} kg/m^2 Pa sec
Permeate Flux*	*Various*

Experiments were conducted [35] at three mass flow rates through the channel: 1.65×10^{-3} kg/s, 1.21×10^{-3} kg/s, and 0.772×10^{-3} kg/s. Table 2.2 shows the experimental results compared to the model.

Table 2.2: Comparison between model presented here and an experiment by Martinez-Deiz [35].

Run #	Mass Flow Rate	Permeate Flux - Expt.	Permeate Flux - Model	% Difference From Experiment
1	1.65×10^{-3} kg/s	10.08 kg/m^{2}hr	16.28 kg/m^{2}hr	61.5%
2	1.21×10^{-3} kg/s	9.36 kg/m^{2}hr	16.05 kg/m^{2}hr	71.5%
3	0.772×10^{-3} kg/s	8.64 kg/m^{2}hr	15.79 kg/m^{2}hr	82.7%

Given the simplicity of the DCMD system, presuming the accuracy of the module geometry and mass flow rate, the results suggest that the value of B is different from the one measured by Vazquez-Gonzalez and Martinez [36] (given in Table 2.1). If only an error in the membrane distillation coefficient is presumed, better agreement is obtained by reducing B to 13×10^{-7}. Additionally the spread in results between each mass flow rate is greater than predicted by the model, with closer agreement at the higher mass flow rate. This suggests inconsistencies in the feed and permeate channel flowrate or channel geometry, and as a result inconsistencies in the temperature polarization, which can be a dominant resistance in DCMD, especially for low Reynolds number feed flows such as the ones in this study. With a small membrane

area, inconsistencies between runs could more dramatically affect the results and the local membrane distillation coefficient could be significantly different in a small membrane coupon vs. a large one due to manufacturing variability or fouling.

2.7.2 Air Gap MD

The Fath et al. [6] air gap system was a larger scale solar-heated installation. Its parameters are shown in Table 2.3. Data was given for the operating conditions and inlet/outlet temperatures over time. For the present comparison, a point in the middle of the day was selected to avoid the effect of startup transients.

Table 2.3: Operating parameters from Fath et al. [6]. Outlet temperatures and mass flow rates, denoted with an asterisk, are compared with the model for validation.

Known Parameters	**Value**	**Approximated Parameter**	**Value**
Feed Flow Rate	0.14 kg/s	Membrane Distillation Coeff.	16×10^{-7} kg/m^2 Pa s
Feed Inlet Temp.	72 °C	Air Gap Width	1 mm
Condenser Inlet Temp.	45 °C	Flow Channel Width	4 mm
Membrane Area	8 m^2		
Permeate Flowrate*	10 kg/hr		
Feed Outlet Temp.*	50 °C		
Condenser Outlet Temp.*	65 °C		

Mean membrane distillation coefficient values for PTFE membranes were obtained from external testing [17, 34, 35]. The value used here represents an average value for commercially manufactured membranes. Measurements for the channel depth and air gap were made from a photo of the cross-section of the module and outer module dimensions [41]. With a mean condensate layer thickness 60 μm, the condensate layer thickness did not exceed 1/10th of the air gap, which is consistent with prior observation [14].

Table 2.4 shows the results of the simulation compared with the experiment. Errors are deviations from the experimental value. For calculating error all temperatures are temperature differences between the inlet and outlet.

Table 2.4: Comparison between simulation and Fath et al. experiment [6].

Quantity	Experimental	Simulated	% Difference from Experiment
Permeate Flow Rate	10 kg/hr	9.38 kg/hr	6.2%
Feed Outlet Temp.	50 °C	49.3 °C	3.3%
Condenser Outlet Temp.	65 °C	67.4 °C	12.0%

The simulation approximates the flux and temperatures well, slightly over-predicting flux and temperature drop. The over-prediction of flux, which would lead to more energy being taken from the feed stream, may be explained by the lack of non-idealities such as heat loss which would affect the channels on the outer-most surface of a spiral-wound module such as this. Also the presence of non-condensible gases and dissolved solids in the seawater would lower the partial pressure on both the feed and air gap sides, resulting in lower flux.

2.7.3 Pumped Vacuum System

While there have been no pilot-scale VMD systems similar to the Fath et al. air gap system, recent experiments have been conducted on smaller bench-top setups. One such setup is a flat sheet system developed by Mericq et al. [42]. Several experiments were conducted with varying salinity brines, including RO retentate. Table 2.5 shows parameters from the lowest salinity experiment with a salt concentration of 38,000 ppm. Fluxes were measured initially and over time to account for fouling of the membrane. The initial flux value is used for comparison as the model does not account for fouling.

The heat transfer coefficient has been calculated from the channel geometry and known flow rate and Reynolds number.

The resultant flux was 10.43 kg/m^{2}hr, 3.2% greater than the initial value measured in the experiment. Since the simulation used pure water properties, there will be a difference of flux due to the reduction in partial pressure of the water vapor and reduction in specific heat capacity [43]. However, an analysis of a VMD module based on the pilot-scale dimensions in Table 2.3 using seawater properties and varying the

Table 2.5: Operating parameters from Mericq et al. [42]. Parameters denoted with an asterisk are compared with the model for validation.

Known Parameters	**Value**
Feed Flow Rate	0.0366 kg/s
Feed Inlet Temp	53 °C
Permeate Side Pressure	7 kPa
Membrane Area	57.75 cm^2
Channel Depth	1 mm
Membrane Distillation Coeff.	4.37×10^{-7} kg/m^2 Pa s
Feed Side Heat Transfer Coeff.	7809 W/m^2K
Permeate Flux*	10.1 kg/m^2 hr

salinity shows that the flux decreases 3% as the salinity increases by 45,000 ppm from 0, which is within the uncertainty in the experimental results.

2.7.4 Membrane Distillation Coefficient Data

The membrane distillation coefficient has a large impact on the flux and, due to the non-uniform nature of MD membranes, it is difficult to determine exactly.

The membrane distillation coefficient, B, is primarily a function of the membrane material properties, the pore size, the vapor being passed through the membrane, and a weak function of temperature. Flow is controlled by two diffusion processes, Knudsen, and molecular diffusion, which depend on the pore size relative to the mean free path of water molecules as given by Equation 2.28:

$$\lambda = \frac{k_B \bar{T}}{\sqrt{2}\pi P_p \sigma_w^2} \tag{2.28}$$

The mean free path is dependent on pressure and temperature. P_p, the sum of the partial pressures, is the total pressure in the membrane pore, and is equal to the pressure on the permeate side at all times and positions. Formulations for each process [44] can be described using Equation 2.29:

$$B_K = \frac{2}{3}\frac{\xi r}{\tau \delta}\left(\frac{8M_w}{\pi \bar{R}\bar{T}}\right)^{1/2} \tag{2.29a}$$

$$B_M = \frac{\xi}{\tau\delta}\frac{P_p D_{w-a}}{p_{p,a}}\frac{M_w}{\bar{R}\bar{T}} \tag{2.29b}$$

$$B = \left[\frac{3}{2}\frac{\tau\delta}{\xi r}\left(\frac{\pi\bar{R}\bar{T}}{8M_w}\right)^{1/2} + \frac{\tau\delta}{\xi}\frac{p_{p,a}}{P_p D_{w-a}}\frac{\bar{R}\bar{T}}{M_w}\right]^{-1} \tag{2.29c}$$

Many studies have attempted to form simpler models for B. A formula incorporating both diffusion processes with a log-mean average [19] was formulated based on average material properties. A simpler formulation [14] neglects Knudsen diffusion. This is applicable for membranes with pores that are large relative to the mean free path of water vapor molecules. It is also has the benefit of being independent of pore size, which can vary widely in a membrane.

Given the connection between local conditions, such as mean temperature, and local pore size and tortuosity, which is usually unknown, a lumped value for B is used to represent the membrane permeability. Additionally, given the variability of membranes and the focus on cycle performance and energy recovery in this thesis, a constant value of B is used as determined from values previously obtained by experiment. This reduces the dependence of the cycle performance on the properties of a specific membrane.

Table 2.6 summarizes B values given in literature for PTFE (Teflon) membranes.

Table 2.6: Experimentally tested membrane distillation coefficients for PTFE membranes. Membranes were tested in DCMD configuration unless otherwise noted.

Source	Manufacturer	Nominal Pore Size	B [kg/m^{2}Pa s]	Notes
[34]	Millipore	220 nm	16.2×10^{-7}	"Durapore" GVHP type
	Experimental	45-373 nm	5.4×10^{-7} - 54×10^{-7}	Manufactured with increasing water content in casting solution 0-6% by wt.
[35]	Gelman Instruments	200 nm	21×10^{-7} - 27×10^{-7}	176 μm thick
[42]	Millipore	220 nm	4.37×10^{-7} with range of 3.6×10^{-7}- 5.2×10^{-7}	175 μm thick, tested on VMD process
[36]	Gelman Instruments	450 - 200 nm	12×10^{-7} - 24×10^{-7}	60 μm thick on PP support layer

In a pumped vacuum system, the greatest resistance is diffusion through the membrane, represented by the membrane distillation coefficient. Therefore this parameter would have the greatest effect on the flux in a VMD module. As shown in Table 2.6, the parameter B can vary widely depending on the process used, with VMD resulting in lower B values. Additionally, in smaller modules damage to the membrane has a more pronounced effect on performance. The model cannot take into account local membrane variations, which must be observed experimentally. Variation in B contributes to difficulty in validating this model with published results, particularly for the small DCMD system [35] compared above.

Chapter 3

Novel MD Configurations

3.1 Solar Direct Heated Membrane AGMD

Membrane distillation has several advantages as a means for renewable-energy powered, off grid desalination and water purification. As a thermally driven membrane technology which runs at relatively low pressure, which can withstand high salinity feed streams, and which is potentially more resistant to fouling, MD could be used for desalination where photovoltaic powered reverse osmosis is not a good option. The use of thermal energy, rather than electrical energy make this technology attractive for applications where input energy and water production would be inherently intermittent and large quantities of electricity (from photovoltaic cells) would be very expensive. Easy scalability and a smaller footprint give it advantages over other large thermal systems such as multi-stage flash and multi-effect distillation for small scale production.

In the novel configuration proposed here, integration of the heat collection and desalination steps is accomplished by using the MD membrane to absorb solar energy. Instead of the fluid stream being heated and sent to the beginning of the MD module at an elevated temperature, the saline fluid stream is heated directly at the point of evaporation by solar energy absorbed by the MD membrane. Figure 3-1 shows the heat and mass flows along a length of membrane.

This configuration has several distinct advantages over traditional MD systems.

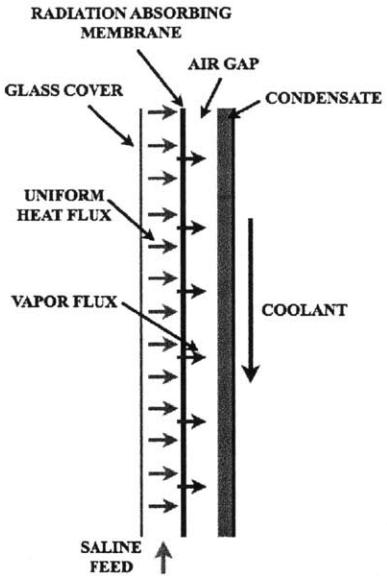

Figure 3-1: Schematic diagram of a radiatively heated MD module with energy and mass flows.

First, since the fluid is being continuously heated while it distills instead of being heated before being distilled, the temperature across the module remains higher, increasing the vapor pressure and the resultant flux due to higher evaporation potential. Secondly, since the heat of vaporization is being provided directly at the liquid-vapor interface, but directly from the heat source, the resistance to heat flow through the boundary layer or temperature polarization is substantially reduced. Lastly the entire MD process is now integrated in one device and can take advantage of simple methods of solar collection and concentration, such as the device shown in Figure 3-2.

Some aspects of this design have been investigated previously. Use of direct heating on the membrane to eliminate temperature polarization was experimentally tested by Hengl et al. [45]. Heating was delivered using an electrically resistive metallic membrane which would be impractical to use in a larger scale system. Energy efficiency performance was not measured. Chen et al. [46] used uniform solar flux to heat the feed stream by placing a solar absorbing surface above the feed stream. This method still retained the temperature polarization effect, but captured the idea of integrating solar collection and desalination into one unit.

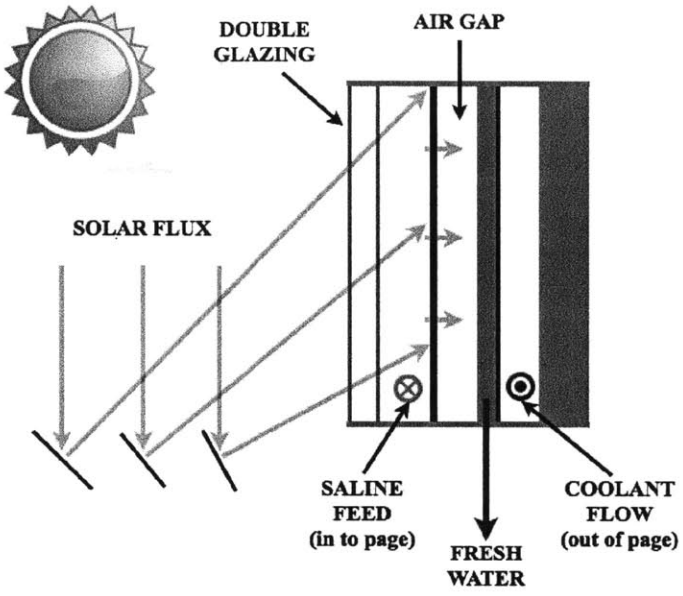

Figure 3-2: Side view of a possible solar direct-heated system configuration.

The feature that strongly distinguishes this system from others developed in the past, is a solar absorbing membrane that sits below the water layer. The membrane can be a dyed single sheet that absorbs solar energy near the MD pores, or a composite membrane with a hydrophilic polymer such as polycarbonate or cellulose acetate, layered on top of a standard MD membrane material, like Teflon (PTFE).

3.1.1 Modeling

The membrane distillation portion of the system was modeled using equations from Chapter 2. However in a directly heated system, there is no external heat input and the energy enters at the membrane surface. Since that surface is exposed to the environment, there are also losses. A control volume of a differential portion of the saline feed channel for this case in shown in Figure 3-3.

Without a solar radiation input, the energy and mass balance of the fluid flowing through differential element remains the same as for any other MD system discussed in Chapter 2. Previous work [47] assumes that the water acts as part of the cover system, and therefore no energy is absorbed in the water layer. However, while solar

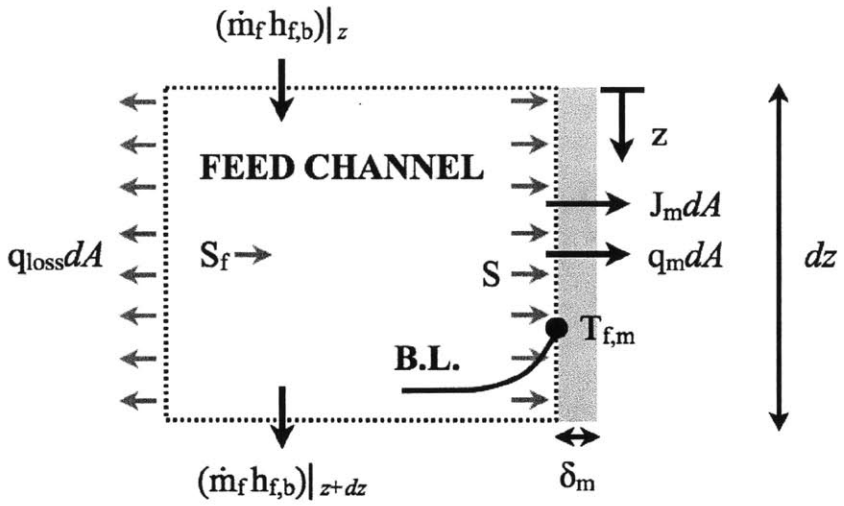

Figure 3-3: The hot side of the MD membrane receiving heat flux, with heat and mass fluxes labeled.

radiation is primarily absorbed at the membrane, the bulk feed stream does absorb a non-negligible amount of solar radiation (approximately 18 % of total absorbed radiation), denoted by the variable S_f. Equation 3.1 details the energy balance in the feed stream and membrane:

$$SdA = -q_f dA + [J_m(h_{fg} + h_{f,m} - h_{f,b}) + q_m]\, dA \tag{3.1a}$$

$$\dot{m}_f dh_{f,b} = [-q_f + S_f]\, dA \tag{3.1b}$$

Consolidating and collecting terms, Equation 3.1a shows that the solar input S is distributed among sensible heating of the feed stream, q_f; energy to evaporate the liquid; and conductive losses through the membrane, respectively. Equation 3.1b accounts for the absorption of solar radiation into the feed stream.

The temperature difference between the feed in the bulk stream and at the membrane surface can be found using the heat transfer coefficient $h_{t,f}$ between the bulk and wall where heat flowing from the membrane to the bulk increases the temperature of the bulk stream over the length of the module as described in Equation 3.2 where

the bulk enthalpy is increased by heat from a hotter membrane:

$$-q_f dA = h_{t,f} dA(T_{f,m} - T_{f,b}) \tag{3.2}$$

Solar Transmission

The quantities S and S_f are determined by the transmission characteristics of the cover system. Since fluid flows over the absorber plate this fluid becomes an additional material in the cover system, attenuating the energy that reaches the absorber.

A system of two covers was described by Duffie and Beckman [23] which would account for incidental reflections between covers, however a good approximation for most solar collectors is that transmission through to the next cover is a fraction of what is transmitted through the previous cover [23]. This is described by Equation 3.3 with the entry angle of the light into the next cover is the exit angle of the previous cover.

$$\tau_2 = (1 - \rho_2)(1 - \alpha_2)\tau_1 \tag{3.3}$$

α and ρ are the fraction of energy lost by absorption and reflection respectively. τ is what is transmitted.

The water layer below the second cover acts as an additional cover. Reflection through the water is a function of the entry angle of a beam of light that exits the glass above it.

$$n_{gl} \sin(\theta_{in}) = n_w \sin(\theta_{out}) \tag{3.4}$$

The perpendicular and parallel components of reflection are defined by Equation 3.5 and can be used to find the total reflectivity of the water layer in Equation 3.6

$$r_{\parallel} = \frac{\tan^2(\theta_{out} - \theta_{in})}{\tan^2(\theta_{out} + \theta_{in})} \tag{3.5a}$$

$$r_{\perp} = \frac{\sin^2(\theta_{out} - \theta_{in})}{\sin^2(\theta_{out} + \theta_{in})} \tag{3.5b}$$

$$(1 - \rho_w) = \frac{1}{2}\left(\frac{1 - r_{\perp}}{1 + r_{\perp}} + \frac{1 - r_{\parallel}}{1 + r_{\parallel}}\right) \tag{3.6}$$

where ρ_w is fraction of beam light reflected from the surface of the water, and $r_{\parallel}$ and $r_{\perp}$ are the parallel and perpendicular components of reflectance respectively.

The loss due to absorptivity of the water layer is slightly more complicated. The glass glazings have a relatively constant extinction coefficient in the visible and near infrared where most solar radiation occurs. The extinction coefficient is related to the amount of radiant energy that gets absorbed per unit thickness and is a function of wavelength as described by Equation 3.7:

$$\alpha(\lambda) = 1 - \exp\left[-\frac{K_{ext}(\lambda)d}{\cos(\theta_{out})}\right] \tag{3.7}$$

For water, the extinction coefficient varies in the range of solar radiation wavelengths [48]. Figure 3-4 shows the transmissivity of water vs. wavelength [48] compared to borosilicate glass, which is a common glazing material in solar collectors [49].

While the extinction coefficient is not related to power linearly, the absorptivity due to the extinction coefficient (Equation 3.7) is, as the total power attenuated at a specific wavelength is the absorptivity multiplied by the input power. The power-averaged absorptivity (Equation 3.8) is used directly in the model instead of calculating it from a single extinction coefficient (as can be done for a glass glazing panel using Equation 3.7).

$$\alpha_w = \frac{\int_0^{\infty} \alpha(\lambda) I_r(\lambda) d\lambda}{\int_0^{\infty} I_r(\lambda) d\lambda} \tag{3.8}$$

where I_r is the irradiance in W/m^2 nm. The irradiance can be approximated by using Planck's Law of emission from a black body in a vacuum [48], where the sun is

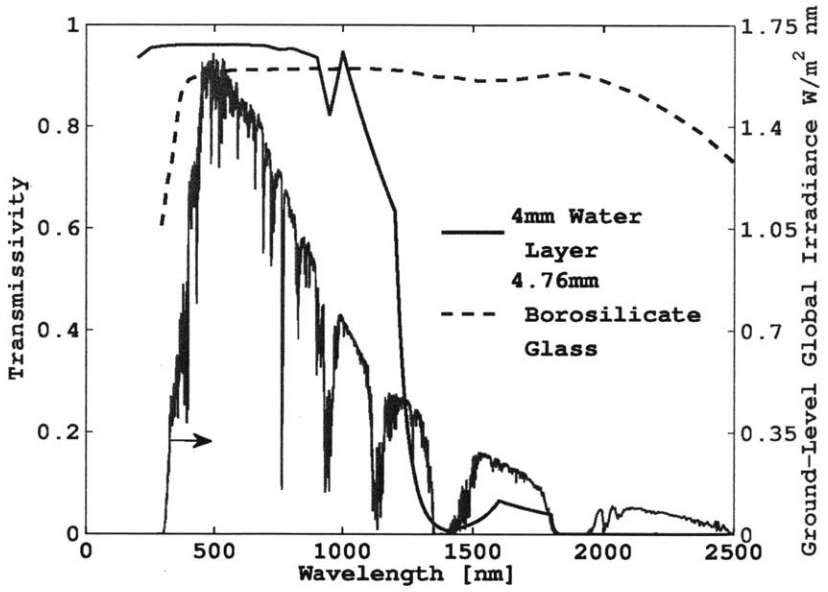

Figure 3-4: Transmissivity of solar collector glass compared to water in the visible and near infrared spectra

approximated as a black body radiating at 5762 K [23].

$$I_{r,bl}(\lambda) = \frac{2h_{pl}c_0^2}{n_{air}^2\lambda^5}\left[\exp\left(\frac{h_{pl}c_0}{n_{air}k_b\lambda T}\right) - 1\right]^{-1} \tag{3.9}$$

This then allows for the calculation of the total transmissivity of the water layer. Using Equation 3.3 the transmissivity of the full stack can be obtained and combined with the solar absorptivity of the membrane to obtain the transmission-absorption product. While the transmission-absorption product is a function of the reflectivity of absorber, the vast majority of opaque absorber materials are minimally reflective and obey the rule described in Equation 3.10 [23].

$$(\tau\alpha) = 1.01\tau_{stack}\alpha_{abs} \tag{3.10}$$

Using Equation 3.10 and breaking down τ_{stack} into its components for a collector

with two glazings, $c1$ and $c2$, the solar absorption of the system can be calculated.

$$S = 1.01\tau_{c1}\tau_{c2}\tau_w\alpha_m \tag{3.11a}$$

$$S_f = 1.01\tau_{c1}\tau_{c2}\alpha_w \tag{3.11b}$$

For simplicity, all solar radiation is assumed to be beam radiation in this model.

Heat Loss From Top of The Module

As with any solar collector the heated surface is exposed to the environment in order to collect solar energy. This results in a certain heat loss along the length. The heat loss through a cover system has been described in detail [23] as well as in previous work by the authors [50].

The loss through the top is a combination of heat transfer from the feed water through the cover system and to the environment. Heat transfer modes are shown in Figure 3-5.

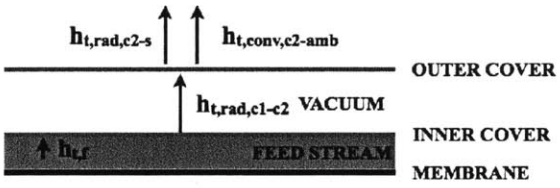

Figure 3-5: Loss modes through the solar collecting surface of the module.

The loss model further approximates the glass covers as opaque to thermal radiation from low temperature sources, and all energy received from radiation is absorbed and re-radiated at the temperature of the cover. Since the thermal radiation from the top cover sees the sky, it is lost to a sky temperature of 4 °C, and the convective loss is to an ambient air temperature of 25 °C. These conditions are typical of a desert environment on a clear day [51]. Typically sky temperature is relatively unimportant for calculating collector performance [23]. However this may become important as

the module can run near 90 °C and radiative loss becomes a higher percentage the total loss to the environment. Convective loss is determined by known correlations for forced convection over a flat plate [40] and an ambient wind speed of 4 m/s. To minimize loss to ambient air the characteristic length of flow over the collector can be kept small by spacers that break up the wind along the length.

3.1.2 Cycle Configurations

A uniformly solar heated MD system can be used in different cycle configurations. The simplest configuration is simply the module itself, which accepts cool saline water at the coolant inlet, and produces fresh water and brine reject at an elevated temperature. Figure 3-6 shows this configuration.

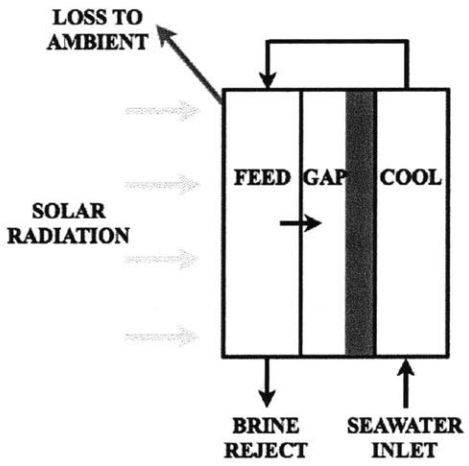

Figure 3-6: A basic desalination cycle using only the AGMD module.

If the temperature of the membrane was higher and more even over the length, the potential for evaporation would be higher and performance should improve for the same solar heat input. This is accomplished by using a recovery heat exchanger, as shown in Figure 3-7.

With solar direct heating, the temperature over the module length is not necessarily more flat, but higher overall. A schematic lengthwise temperature profile is

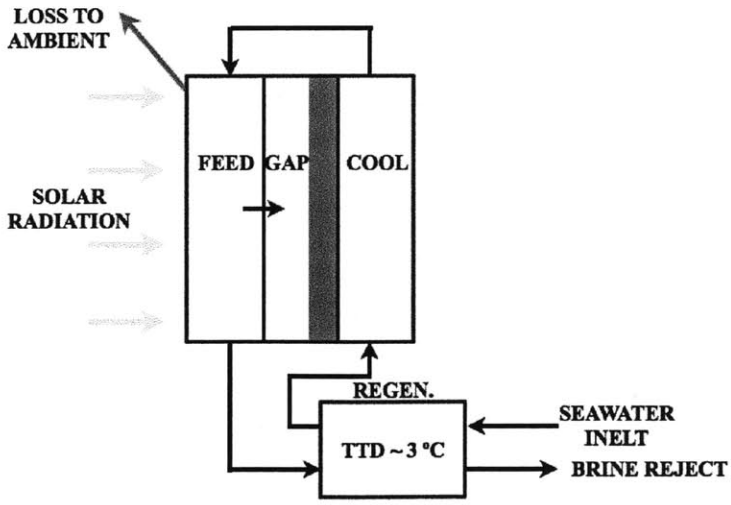

Figure 3-7: An AGMD desalination unit with recovery heat exchanger at the bottom of the cycle.

shown in Figure 3-8. The effect of overcoming heat transfer resistance through the bulk feed stream is evident at the inlet as well.

This configuration shows promise for developing compact, single-unit, distillation systems, which represent an improvement over current solar distillation technologies, including solar stills and other solar-powered MD systems.

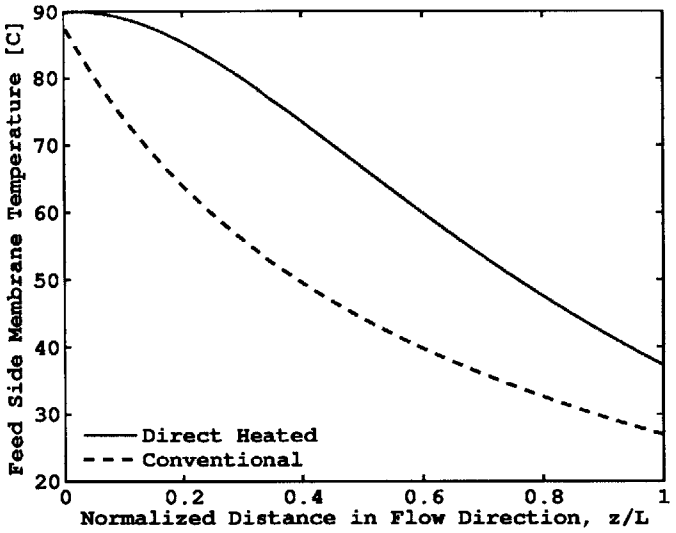

Figure 3-8: Temperature profile of the feed side of the membrane along the collector length for a solar direct heated system at an insolation of 850 W/m^2 compared with a system conventionally heated to the same maximum membrane temperature.

3.2 Multi-Stage Vacuum MD

As demonstrated in prior work [52], the performance of single stage VMD systems is inherently limited. A parametric study of the size and operating parameters of a single stage VMD cycle, demonstrated that the fundamental performance limit of a single-stage VMD systems is a GOR of 1.

This limit arises from the fact that energy recovery is limited by the saturation temperature of the pressure in the condenser. Maximizing flux by increasing the pressure difference between the saline feed and the condenser lowers the condensation temperature in the condenser, which requires high mass flow rates of colder water to condense the additional vapor when compared to a system with a smaller pressure difference (higher saturation temperature) and lower water output. This trade-off results in poor energy recovery.

One way to maximize energy recovery is to stage the MD modules in a similar manner as that found in multi-stage flash (MSF) desalination. In MSF vapor is produced by flashing heated liquid at subsequently lower pressures. The vapor is

condensed at the reduced pressure in each stage pre-heating saline water, which acts as a coolant. MSF systems can have upwards of 45 stages with a small pressure difference between them. The simplest case is the once-through MSF system. This system achieves a GOR of 3-7 depending on the season. In winter, lower feed water temperatures reduce performance, as greater feed preheating is required [53]. Figure 3-9 shows a typical MSF desalination system.

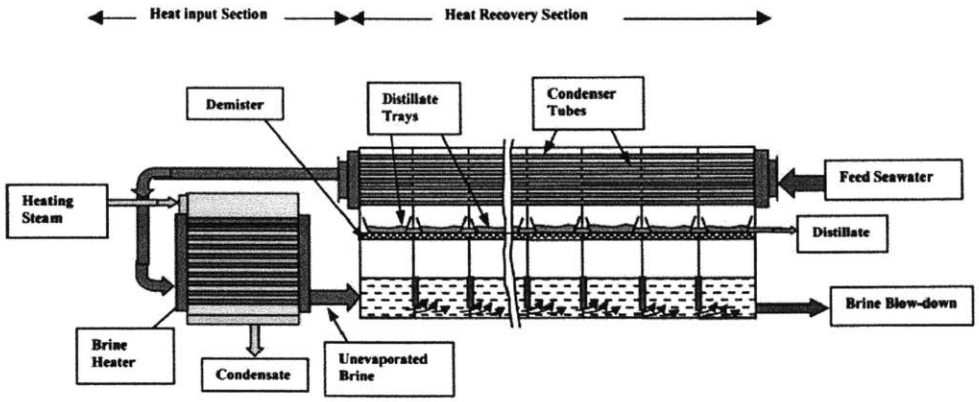

Figure 3-9: Process diagram for a once-through MSF system [53].

In the proposed configuration of VMD, the flash chambers of MSF are replaced with membrane distillation modules. Optimal sizing of module features would maximize the amount of membrane area producing vapor, while to minimizing temperature polarization and pressure drop. Figure 3-10 shows a multi-stage VMD system.

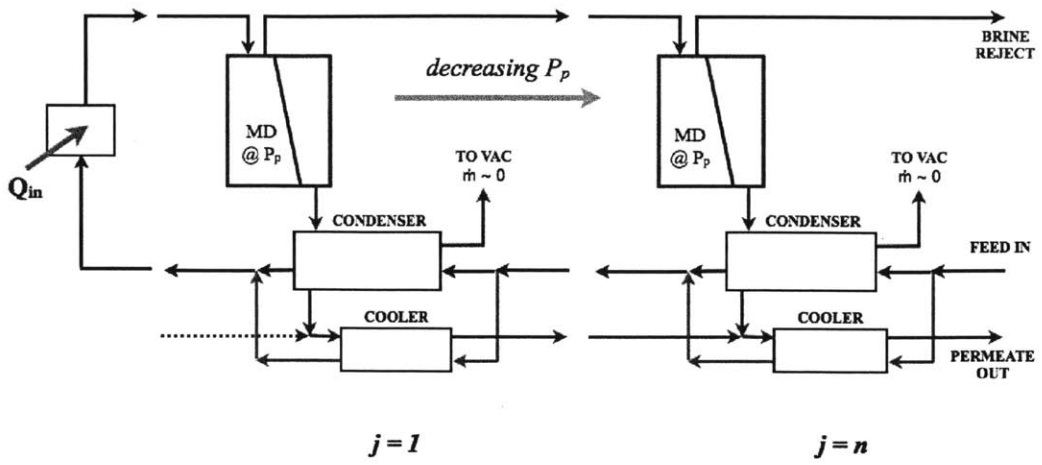

Figure 3-10: Multi-Stage Vacuum MD (MS-VMD) process diagram.

This configuration has several distinct advantages over MSF. MD systems are more easily scaled down. MSF systems are typically built into municipal water systems and desalinate hundreds of thousands of cubic meters of water per day. Flash chambers have to be large to accommodate the vapor and reduced pressure. Flash chambers also require extra hardware to keep seawater mist from contaminating the condensed vapor. MD modules can be built smaller to accommodate lower volume applications, such as off-grid water purification. In MD, spaces where the pressure is reduced are very small requiring a smaller amount of lower strength, and often cheaper, materials to support the pressure difference. Lower temperatures in MD also mean that the membrane and heat exchanger surfaces are less prone to fouling.

In cases where such a system may be used off-grid, reduced pressure can be generated from a mechanical vacuum pump powered by photovoltaics. For a larger scale system a steam ejector can be used to maintain vacuum in each MD stage, as is done in a multi-effect distillation (MED) system.

3.2.1 Modeling

A model for a multi-staged VMD system can be formed by repeatedly solving the equations outlined in Chapter 2 for each membrane module, and then connecting the

module to the other components in Figure 3-10. Each stage shown is then connected with the neighboring stage by equating enthalpy and mass flow rates

The other components in the system (heat exchangers, condensers, and the feed heater) are modeled based on "black box" control volume models. The condenser and permeate cooler are both modeled with an effectiveness model and energy balance. Equations 3.12 - 3.13 detail the energy balance and effectiveness model for the condenser.

$$\dot{m}_{cond} c_p \left(T_{cond,out} - T_{cond,in}\right) = \dot{m}_p \left(h_{p,v} - h_{p,l}\right) \tag{3.12}$$

$$\epsilon = \frac{\left(h_{p,v} - h_{p,c}\right)}{\left(h_{p,v} - h_{p,l,max}\right)} \tag{3.13a}$$

$$\frac{h_{p,l,max}}{c_p} = T_{cond,in} \tag{3.13b}$$

where the subscript *cond* denotes the coolant passing through the condenser, which is saline water being pre-heated, and p denotes permeate water passing from the vapor state, v to a condensed liquid state, c. A perfectly effective condenser ($\epsilon = 1$) would cool the liquid permeate to the coolant inlet temperature. A model for the permeate chiller follows similarly, however instead of entering as a vapor the permeate would enter the chiller carrying an enthalpy $h_{p,c}$.

As a means of comparison with an MSF system, the component performance can be measured by the log-mean temperature difference (ΔT_{lm}). These are approximately 13 °C for the condenser and 10 °C for the permeate chiller. Similar or better component effectiveness can be found in actual large-scale MSF systems [54]. These log-mean temperature differences correspond to effectiveness, ϵ, values of 0.98 and 0.96 for the condenser and permeate chiller respectively. Equation 3.14 defines the log-mean temperature difference for the heat transfer components where the subscripts *in* and *out* represent the coolant stream and *hot* represents the inlet stream of the fluid to be cooled or condensed.

$$\Delta T_{lm} = \frac{T_{out} - T_{in}}{\ln\left(\frac{T_{hot}-T_{in}}{T_{hot}-T_{out}}\right)} \tag{3.14}$$

3.3 Novel Energy Recovery Enhancements

Several means of enhancing energy recovery in MD systems can be employed that represent an improvement over traditional methods. They include recovering heat from the hot brine without brine recirculation, and reducing the pressure in air gap systems to improve diffusion of vapor across the gap.

3.3.1 Hot Brine Discharge Regeneration

A common method of recovering energy from hot brine reject is to mix the reject with fresh brine, sending warmer, but more concentrated brine back into the desalination system. While this method is simple, and avoids an extra heat exchange step, it is limited in its effectiveness, and concentrated brine can severely scale a desalination system. While MD systems are less prone to scaling and fouling, high brine concentrations can still block membrane pores and reduce hydrophobicity [55]. Recovering the energy from brine reject while limiting feed concentration can easily be accomplished by adding another heat exchanger at the bottom of an MD cycle. Figure 3-11 shows a brine regeneration heat exchanger on an AGMD Cycle.

Modeling

The heat exchanger is a counterflow device modeled as a "black box" model with a fixed terminal temperature difference (TTD). Equation 3.15 shows a simple energy balance around the heat exchanger, assuming it is fully insulated.

$$\dot{m}_{f,out} c_p \left(T_{f,out} - T_{f,rej}\right) = \dot{m}_{f,in} c_p \left(T_{c,in} - T_{SW,in}\right) \tag{3.15}$$

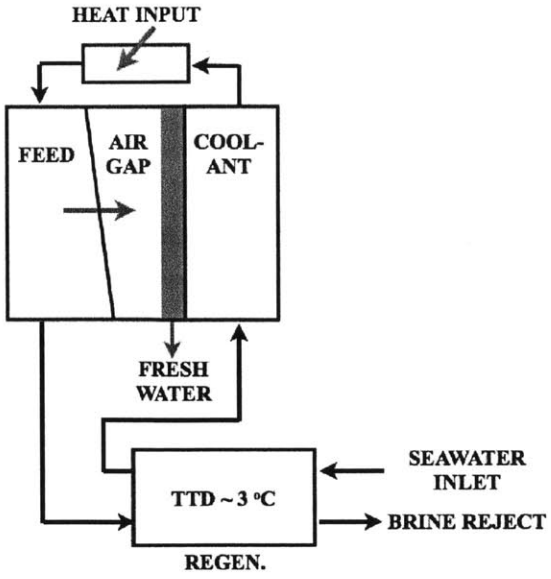

Figure 3-11: Brine regeneration in AGMD

where $T_{f,out}$ is the temperature of the brine exiting the MD module, $T_{f,rej}$ is the brine reject exiting the heat exchanger, and $T_{c,in}$ is the temperature of the preheated feed exiting the heat exchanger and entering the coolant side of the MD module. The above equation has two unknowns, and to fix the one of the unknowns Equation 3.15 is used. The TTD is typically a fixed performance parameter; 3 K is a typical value for most counterflow exchangers.

$$\mathrm{TTD} = \min\left[\left(\mathrm{T_{f,rej}} - \mathrm{T_{SW,in}}\right), \left(\mathrm{T_{f,out}} - \mathrm{T_{c,in}}\right)\right] \tag{3.16}$$

Energy Efficiency Comparison

When applied to an AGMD process, recovering energy from the hot brine significantly increases efficiency, allowing the cycle to reach its top temperature with a lower heat input. For an AGMD system operating over the same temperature range, Figure 3-12 shows the difference in GOR between both systems as a function of heat input normalized to the heat input required to heat a system without energy recovery to

a feed inlet temperature, $T_{f,in}$, of 90 °C. The feed inlet temperature of both systems sweeps from 38 °C to 90 °C as heat input increases.

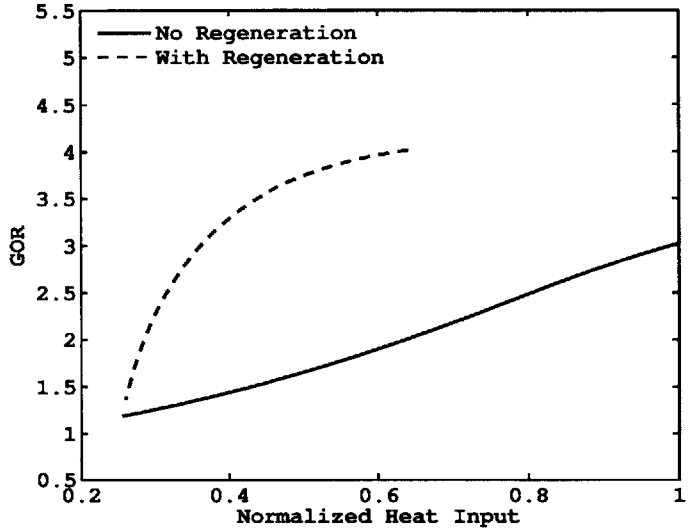

Figure 3-12: Comparison of GOR for an AGMD system with and without regeneration.

The effect of regeneration is immediately apparent as the same top temperature (and thus comparable product flow rate) is achieved with a fraction of the heat input for a system without regeneration.

3.3.2 Reduced Pressure Gap AGMD

Reducing the pressure in an Air Gap MD system has the effect of reducing the diffusion resistance of water vapor through the gap.

Modeling

The effect of reduction of the diffusion resistance is clearly evident when considering Equation 2.17, repeated here:

$$\frac{J_m}{M_w} = \frac{c_a D_{w-a}}{d_{gap} - \delta} \ln\left(1 + \frac{x_i - x_{a,m}}{x_{a,m} - 1}\right) \tag{3.17}$$

The diffusion coefficient of water in air D_{w-a} is defined as [38]:

$$D_{w-a} = 1.97 \times 10^{-5} \left(\frac{P_a}{P_{atm}} \right)^{-1} (T/256)^{1.685} \tag{3.18}$$

where T is the mean gap temperature in kelvin. As gap pressure P_a decreases, the diffusion coefficient goes up. Not only does the diffusion coefficient increase, the vapor concentration increases, allowing more vapor in the gap for a given difference in mole fraction. These effects allow an increase in flux without increasing the temperature across the gap, and without increasing the heat input required. As a result, GOR increases.

Comparison with Gap Reduction

When assessing the effect of pressure reduction on an AGMD system, it can be thought of as effectively reducing the gap size. Conversely, reduced pressure can allow for the construction of a gap with larger dimensions and reduced dimensional tolerances for a more easily built system. Figure 3-13 shows that reducing the pressure in an AGMD system with a 4 mm gap width from 1 atmosphere is to 0.2 atm results in a comparable improvement to reducing the gap size from 4 mm to 1 mm at atmospheric pressure.

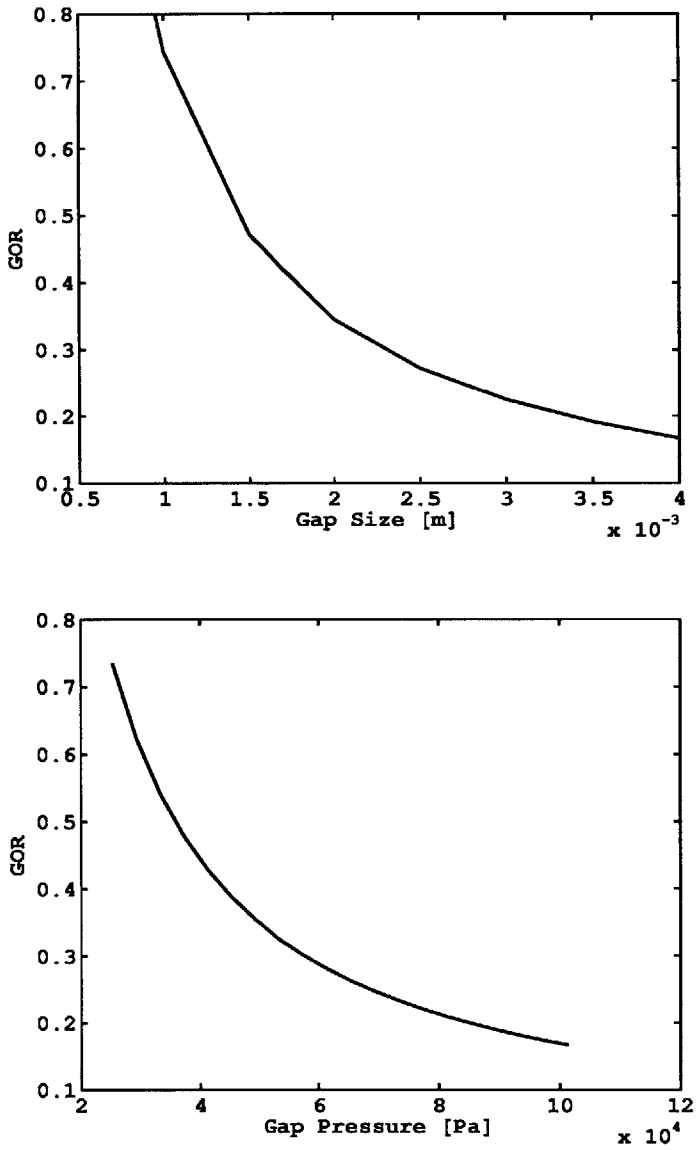

Figure 3-13: Comparison of energy efficiency improvement resulting from reducing the gap size and gap pressure in an AGMD system with 100 m^2 of membrane area.

Chapter 4

Experimental Validation

To validate the model and test the novel principles described in the previous chapters, a bench-top experiment was designed, subject to the limits of manufacturability, and constraints on operational parameters such as mass flow rate and pressure drop. The experiment was designed to be modular, and reconfigurable to test both conventional and solar heated systems, as well as implement any improvements to the cycle such as brine regeneration, or gap pressure reduction.

4.1 Experimental Scaling

To understand how the energy efficiency performance of a bench-top experimental system relates to that of a large-scale production system of the same configuration (i.e., AGMD), it is necessary to know how the system scales with input parameters such as system size, feed mass flow rate, and operating temperature. The model for an AGMD system consists of many equations and is highly nonlinear, depending in large part on exponential functions of temperature and of the permeate flux itself multiplied by the effects of system size. However, it can be simplified using some order of magnitude estimates derived from the numerical solution to the detailed system of equations outlined in Chapter 2.

In analyzing the results of the detailed model the following approximations can be made:

- Heat conduction through the membrane, q_m, is negligible. $q_m/J_m h_{fg} < 0.1$. Since the air in the gap has good insulating properties heat flux as a result of conductive losses through the membrane are small compared to the energy carried by the latent heat of the vapor.

- The thickness of the liquid condensate layer in the gap, δ, is negligible. $\delta/d_{gap} < 0.15$. This ratio is even lower at the top of the module where there is a small amount of condensed vapor.

- The change in temperature across the gap along the length of the module is small relative to the absolute temperature (in kelvin) of the vapor in the gap. $(T_{f,b} - T_{c,b})/\bar{T}_{gap} < 0.05$. For the purpose of calculating the vapor concentration in the gap by means of the ideal gas law (Equation 2.18), the average absolute temperature can be held constant. For this simplified model, it is fixed to $(T_{top} + T_{bot})/2$.

- The diffusion coefficient of water vapor in air, D_{w-a}, is assumed to be constant at a given gap pressure, as it is only a weak function of temperature.

To further simplify the model, the vapor pressure/dewpoint temperature equation, also known as the Antoine Equation, can be simplified as an exponential function with only two constants by fitting data obtained from the full Antoine Equation. For the operational range of MD (25-95 °C) the following equation is obtained:

$$p_w = C_1 \exp(C_2 T) \tag{4.1}$$

where $C_1 = 1134.8$ Pa and $C_2 = 0.0473$ 1/°C with a R^2 value of 0.998. This makes this a good approximation of the vapor pressure as a function of temperature for most MD systems, and makes the model easier to simplify.

The flux across the module will be evaluated at the top of the module where the bulk feed temperature is the top temperature of the cycle T_{top}. Evaluating the flux starts with the equation for flux permeating through a membrane:

$$J_m = B(p_{w,f,m} - x_{a,m}P_a) \tag{4.2}$$

The vapor pressure on the feed side can be found in terms of feed membrane temperature, $T_{f,m}$, and the simplified Antoine Equation, Equation 4.1, evaluated at that temperature. This membrane temperature is lower than the bulk temperature as a result of temperature polarization. This is estimated by the heat flow out of the feed and heat transfer coefficient, h_t. If location of the evaluation is the top, the membrane temperature is:

$$T_{f,m} = T_{top} - \frac{J_m h_{fg}}{h_t} \tag{4.3}$$

The sensible cooling of the liquid that becomes the permeate as it travels from the bulk feed to the membrane is neglected, as this is typically less than $0.01 J_m h_{fg}$ in solutions of the detailed model.

The vapor mass fraction on the gap side (denoted by the subscript a) of the membrane is a function of the vapor fraction gradient, as described by Equation 2.17. Since the thickness of the condensate layer is neglected and the concentration c_a is fixed at the constant average temperature $\bar{T}_{gap}$ this becomes:

$$J_m = \frac{P_a}{(\bar{R}/M_w)\bar{T}_{gap}} \frac{D_{w-a}}{d_{gap}} \ln\left(1 + \frac{x_i - x_{a,m}}{x_{a,m} - 1}\right) \tag{4.4}$$

which may be rearranged to solve for $x_{a,m}$:

$$x_{a,m} = 1 + \exp\left[\frac{-J_m(\bar{R}/M_w)\bar{T}_{gap}d_{gap}}{D_{w-a}P_a}\right](x_i - 1) \tag{4.5}$$

The vapor fraction at the condensate layer interface, x_i, can be determined using Equation 4.1 by evaluating it at the interface temperature where $x_i = p_w(T_i)/P_a$. This interface temperature is also the wall temperature of the condenser, since the condensate layer has no thickness. Since the condenser wall is typically made of a highly thermally conductive material, such as copper, it too has negligible resistance. Therefore the interface temperature can be related to the coolant temperature by the

heat transfer coefficient, which for a coolant channel of the same geometry as the feed channel is also h_t:

$$T_i = T_{c,b} + \frac{J_m h_{fg}}{h_t} \tag{4.6}$$

To evaluate the flux across the top of the module, the temperature of the coolant at the top of the module must be approximated. Since AGMD systems operate in counterflow, as shown in Figure 2-4, the temperature at the exit of the coolant channel is increased by the energy of condensation that is absorbed along the full length of the membrane. A simple energy balance, shown in Equation 4.7, can be used to approximate the coolant exit temperature. Since membrane flux varies along the length, with flux at the bottom of the module approximately 1/3 of that at the top, an average value of flux expressed as a fraction of flux at the top is used. This fraction is approximately 2/5 and is determined by solving the detailed numerical model for a variety of top temperatures, mass flow rates, and system sizes, and taking an average of this ratio. Generally the ratio is a strong function of top temperature, owing to the exponential dependence of the driving pressure on temperature, and a very weak function of system size.

$$\dot{m}_f c_p (T_{c,b} - T_{bot}) = (2/5) J_m h_{fg} A_m \tag{4.7a}$$

$$T_{c,b} = \frac{(2/5) J_m h_{fg} A_m}{\dot{m}_f c_p} + T_{bot} \tag{4.7b}$$

It is now possible to back substitute Equations 4.3 - 4.7 into each other and then into Equation 4.2 to obtain an implicit expression for flux, as shown in Equation 4.8.

$$\begin{aligned} J_m = {} & BP_a \left[\exp\left(-J_m \frac{(\bar{R}/M_w)\bar{T}_{gap} d_{gap}}{D_{w-a} P_a} \right) - 1 \right] + \\ & BC_1 \exp\left(C_2 T_{top} - J_m \frac{C_2 h_{fg}}{h_t} \right) - \\ & BC_1 \left[\exp\left(C_2 T_{bot} + J_m \left(\frac{C_2 h_{fg}}{h_t} - \frac{(\bar{R}/M_w)\bar{T}_{gap} d_{gap}}{D_{w-a} P_a} + \frac{C_2 (2/5) A_m h_{fg}}{\dot{m}_f c_p} \right) \right) \right] \end{aligned} \tag{4.8}$$

Equations for heat input, GOR, and recovery ratio (RR) in terms of flux at the top of the system can also be obtained:

$$\dot{Q}_{in} = \dot{m}_f c_p (T_{top} - T_{c,b}) = \dot{m}_f c_p (T_{top} - T_{bot}) - (2/5) J_m h_{fg} A_m \tag{4.9a}$$

$$\text{GOR} = \frac{(2/5) J_m h_{fg} A_m}{\dot{Q}_{in}} = \left[\frac{\dot{m}_f c_p (T_{top} - T_{bot})}{(2/5) J_m h_{fg} A_m} - 1 \right]^{-1} \tag{4.9b}$$

$$RR = \frac{J_m (2/5) A_m}{\dot{m}_f} = \frac{c_p (T_{top} - T_{bot})}{h_{fg}} \left(\frac{1}{\text{GOR}} + 1 \right)^{-1} \tag{4.9c}$$

First, a non-dimensional water production rate based on the driving evaporation potential governed by difference between the top and bottom temperatures is found in the formulation of Equation 4.8:

$$R_P = \frac{B C_1 \exp\left[C_2 \Delta T\right] A_m}{\dot{m}_f} \tag{4.10}$$

where ΔT is the temperature difference $T_{top} - T_{bot}$. This captures the operating temperature difference and membrane properties, in the form of B. It is non-dimensionalized by the feed mass flow rate.

From Equation 4.8 several parameter combinations can be observed, which govern the energy recovery and energy effectively consumed to drive the evaporation potential:

$$R_D = \frac{(\bar{R}/M_w) \bar{T}_{gap} d_{gap}}{D_{w-a} P_a} \tag{4.11a}$$

$$R_T = \frac{C_2 h_{fg}}{h_t} \tag{4.11b}$$

$$R_R = \frac{C_2 (2/5) A_m h_{fg}}{\dot{m}_f c_p} \tag{4.11c}$$

To obtain the effect on the driving force, these ratios are multiplied by the total flux, and thus the ratios have units of inverse flux, or s m^2/kg.

The energy consumed to drive the evaporation goes with the mass transfer across the gap (R_D), and temperature polarization in the feed and coolant channels (R_T).

R_R goes with the system energy recovery. In a membrane distillation system, GOR generally goes up with an increase in flux, driving potential, and energy recovery, with energy recovery being the dominant contribution to GOR for systems of low flux and large membrane size. The first two ratios relate to the resistance to vapor mass transfer (in the form of reduced pressure driving force due to temperature polarization, and mass transfer resistance through the gap). GOR would vary with the inverse of these ratios. The heat transfer coefficient that appears in the temperature polarization ratio is also a function of system size, most strongly the mass flow rate and cross sectional area of the flow channel. Since the relation between system size and heat transfer coefficient varies with the flow regime, a simplified relation between heat transfer coefficient and system size cannot be obtained for all systems. Therefore, the inlet parameters will remain expressed as h_t and explicitly calculated based on the fixed system size and constant fluid properties.

Given a non-dimensional driving force and several additional parameters relating to the energy consumption and recovery, a non-dimensional parameter relating to the system performance can be postulated by arranging each additional parameter (R_D, R_T, and R_R) based on their relative impact on GOR in to a non-dimensional ratio and multiplying that ratio by the non-dimensional driving force (R_P):

$$\Psi = R_P \frac{R_R}{R_T + R_D} = \frac{BC_1 \exp\left[C_2 \Delta T\right] A_m}{\dot{m}_f} \frac{(2/5) A_m h_{fg}}{\dot{m}_f c_p \left(\frac{h_{fg}}{h_t} + \frac{(\bar{R}/M_w)\bar{T}_{gap} d_{gap}}{C_2 D_{w-a} P_a} \right)} \tag{4.12}$$

The effect of each parameter can be seen on system performance. The system is more energy efficient when the area is large relative to the feed mass flow rate, the gap is small (reducing the length for vapor diffusion), the heat transfer coefficient is higher, diffusion coefficient is maximized, and the driving potential for evaporation is high. Some parameter changes, such as providing a large membrane area (i.e., large channel width and long length) can be at odds with increasing heat transfer coefficient (i.e., reducing channel width and increasing Reynolds number for a given feed mass flow rate) and require optimizing the system parameters given cost and constructibility

constraints. The trend of Ψ holds for systems of any size. For some small systems, such as the experimental system described in this chapter, the effect of temperature polarization and diffusion resistance ($R_T + R_D$) can be much larger than the energy recovery, and as a result these systems perform substantially more poorly and Ψ is small, or less than one.

To validate Ψ as a scaling parameter, it can be evaluated across a range of MD systems for which GOR is determined using the validated detailed model from Chapter 2. A set of test cases can be created by varying several design parameters one at a time while keeping the remaining ones constant. The baseline parameters are listed in Table 4.1. These systems represent all sizes and performance levels, and are not necessarily optimized for GOR. The baseline systems is representative of a typical production-scale system.

Table 4.1: Parameters of a baseline AGMD system from which test cases are generated.

Parameter	**Value**
Mass Flow Rate [kg/s]	1
Inlet Temperature, T_{bot} [°C]	20
Top Temperature, T_{top} [°C]	85
ΔT [°C]	57
Length [m]	145
Width [m]	0.7
Flow Channel Depth [mm]	4
Gap Size [mm]	1.55
Membrane Material	PVDF
Membrane Dist. Coefficient, B [kg/m^{2}Pa s]	16×10^{-7}
Membrane Pore Size [μm]	0.2
Membrane Thickness [mm]	0.2
Air Gap Spacer Open Area [-]	50%
Air Gap Spacer Material	Polyproplyene

Each of the design parameters in Ψ are varied, and the resultant GOR and Ψ values are plotted on the same graph. If Ψ is an appropriate non-dimensional parameter describing the AGMD process, then all the points should fall essentially on the same curve. There will be some inconsistencies arising from the approximations made to obtain the simplified model and Ψ. Figure 4-1 shows this relationship for 66 different

AGMD systems as modeled with the detailed model described in Chapter 2.

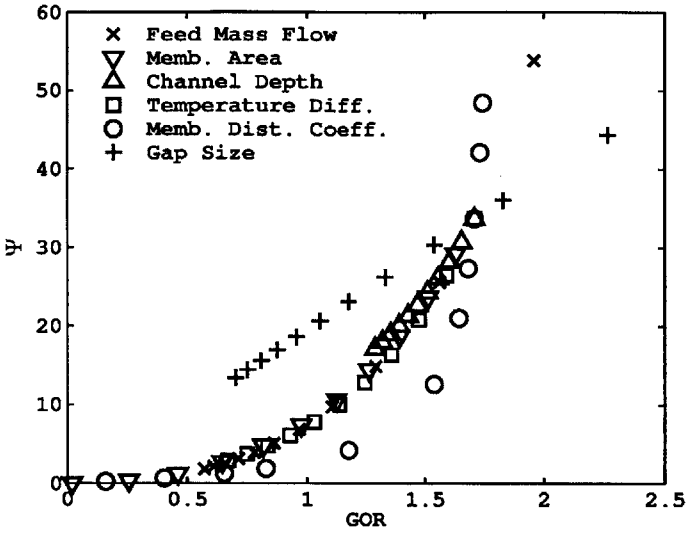

Figure 4-1: Non-Dimensional System Parameter Ψ vs. modeled GOR for 66 different systems.

It can be seen that, for most of the design parameters varied, the relationship between GOR and Ψ for each collapse onto the same curve. There is some variation from the model simplification, but most parameters behave with a similar polynomial dependence. The relationship predicted by varying the air gap size, however does not fit, and results in a linear relationship between GOR and Ψ. Varying B results in a relationship that is of a higher order polynomial than the rest of the data. Ψ is completely insensitive to the effects of gap pressure, because approximations made in the simplified model result in the gap pressure dropping out in the term $D_{w-a}P_a$. Therefore Ψ cannot be used for comparisons across pressure, gap size, and membrane properties.

For the purposes of comparing the experimental system designed in this Chapter (Table 4.2) with production scale systems such as one described in Table 4.1, the poor prediction of GOR using Ψ for systems of varying gap size and membrane properties can be eliminated when assessing the overall relationship between GOR and Ψ. This is because production and bench scale systems can be built with similar

(small) gap sizes and the same membrane, but a system with hundreds of square meters of membrane area and multiple kilograms per second of feed mass flow rate that cannot fit on a lab bench. As a result the test cases generated from Table 4.1 use the same gap size as the experimental system, 1.55 mm, as well as the same membrane, $B = 16 \times 10^{-7}$ kg/m^2 Pa s. When systems of varying gap size and membrane properties are eliminated from calculating the relationship between Ψ and GOR, Figure 4-2 shows the resulting relationship. The relationship is polynomial in nature in the form of $\Psi = A\text{GOR}^n$. A very good fit ($R^2 = 0.995$) is obtained for $A = 7.3$ and $n = 2.9$. The bench-scale experiment is shown for comparison, which is very well predicted by the curve.

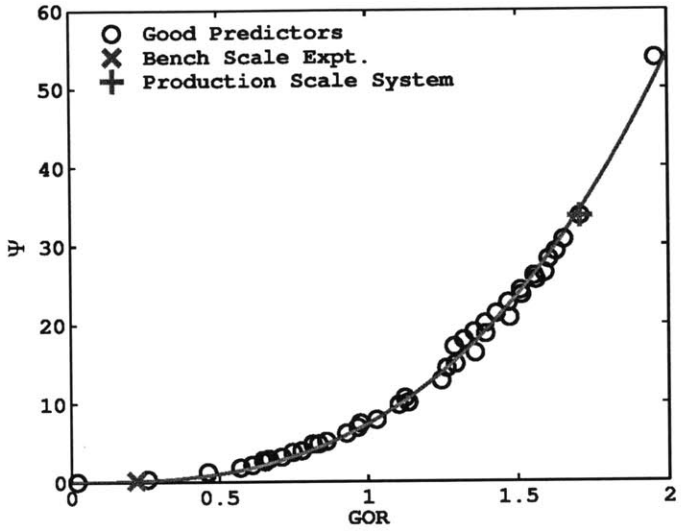

Figure 4-2: Non-Dimensional System Parameter Ψ vs. GOR with best fit curve

Therefore, in comparing the performance of a bench scale experiment to a production scale system with the same membrane and gap size, one would multiply the results from the small system by the ratio $(\Psi_{prod}/\Psi_{expt})^{1/2.9}$.

Since Ψ is a non-dimensional parameter it can be used to relate other system outputs, if those outputs are expressed as a function of other non-dimensional parameters, such as the gained output ratio where $\text{GOR} = (\Psi/7.3)^{(1/2.9)}$. A non-dimensional parameter for the permeate flow rate, expressed as the recovery ratio, can be derived

by using the relationship in Equation 4.13.

$$\Psi_{RR} = \frac{c_p(T_{top} - T_{bot})}{h_{fg}} \left(\frac{1}{(\Psi/7.3)^{1/2.9}} + 1 \right)^{-1} \tag{4.13}$$

The same method for determining the relationship between Ψ to GOR ca be used to determine the relationship between Ψ_{RR} to recovery ratio. Figure 4-3 shows plots for the same set of systems as in Figure 4-1.

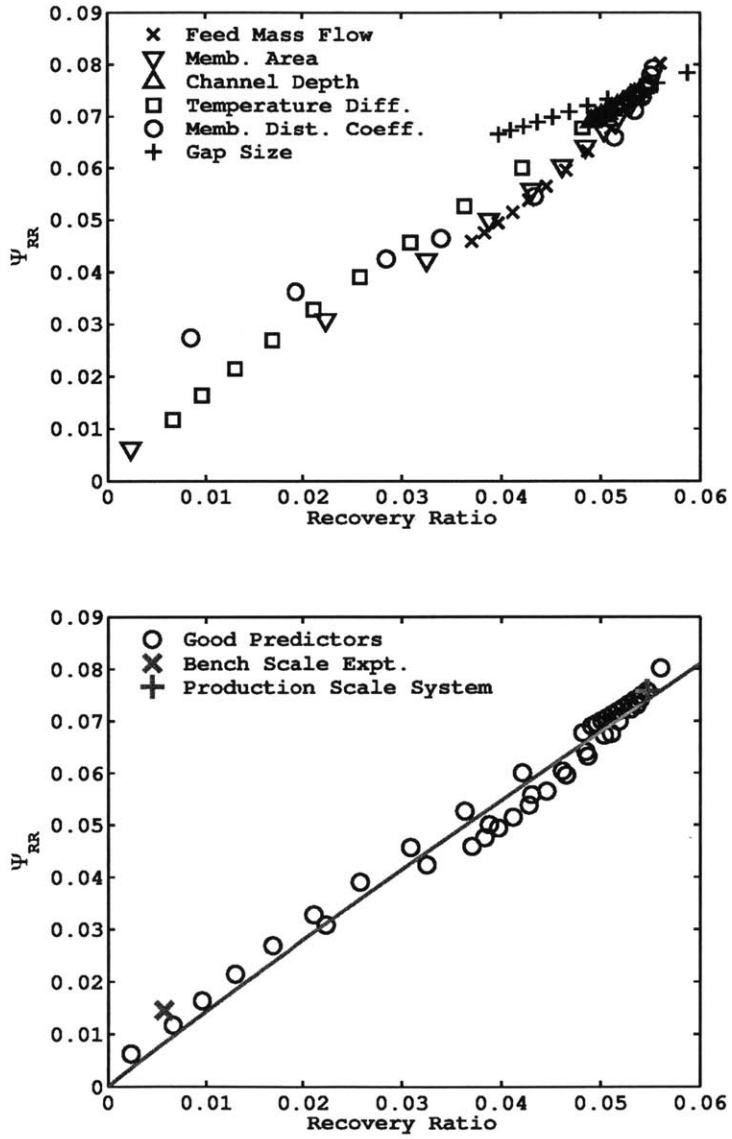

Figure 4-3: Relationship of Ψ_{RR} vs. recovery ratio with best fit curve.

The resulting polynomial relationship in the form of $\Psi_{RR} = A\ RR^n$ is nearly linear, where $A = 1.24$ and $n = 0.97$. It too is a good fit, with an R^2 value of 0.977.

Using Equation 4.13 the recovery ratio result of a small system to that of a larger system can be done multiplying the recovery ratio of the experimental system by $(\Psi_{RR,prod}/\Psi_{RR,expt})^{1/0.977}$.

Due to the highly non-linear equations governing the AGMD process, the relationship between Ψ_{large} and Ψ_{small} can only be an approximate means of scaling a system of two different sizes provided they have the same gap size, membrane properties, and gap pressure, as the coefficients of $\Psi = A\text{GOR}^n$ change significantly with the change in those parameters. For all other design parameters, Ψ can provide a robust description of the process across the parameter range, allowing prediction of the performance of a system of larger size from an experiment with the same membrane, gap size, and gap pressure.

4.2 Design and Construction

In order to further validate the modeling shown in Chapter 2, and to prove the novel concepts shown in Chapter 3, a modular experiment was constructed which could easily be reconfigured depending on the mode being tested. Figure 4-4 shows the layout with all the components necessary to test the various different configurations.

4.2.1 Objectives

There were three primary goals of the experimental work:

- Validate models for conventional AGMD, hot brine stream energy recovery, reduced pressure gap, and solar direct heated concepts.
- Establish the importance of solar absorbing membrane in the solar direct heated concept.
- Demonstrate the energy efficiency (GOR) of various concepts.

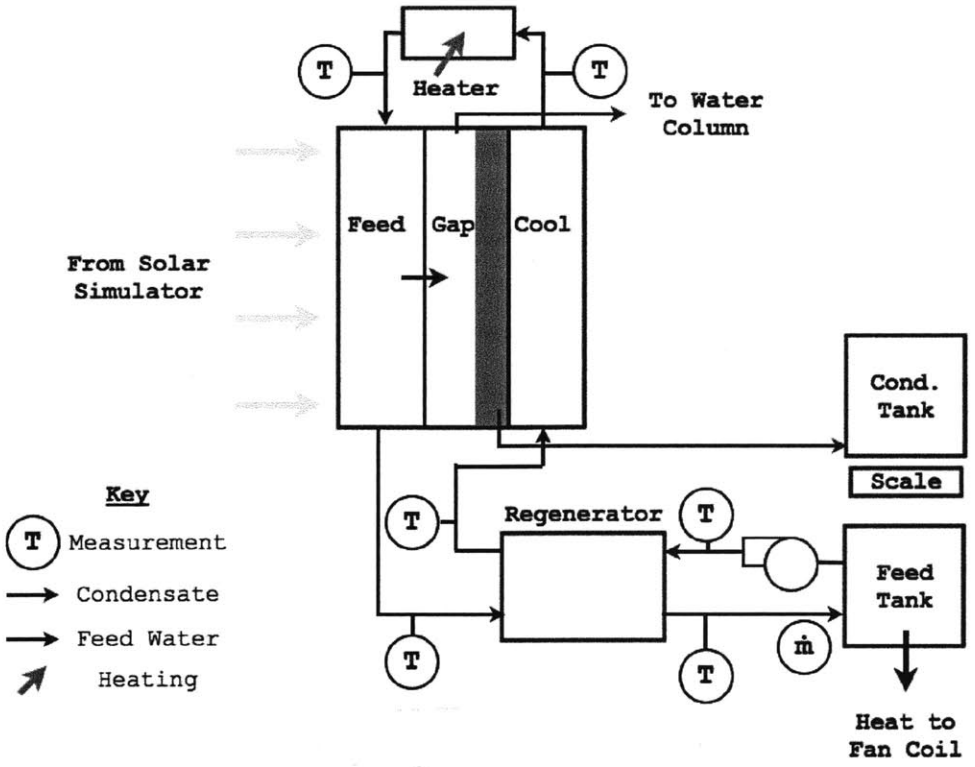

Figure 4-4: Flow sheet for the experimental setup with all possible configurations shown.

4.2.2 Experimental Design

Due to lack of adequate sunlight in the northeastern United States, the system was sized to be illuminated by a bench-top solar simulator for testing of the solar direct heating concept. This constrained the illuminated channel to a 9 x 9 in (23 x 23 cm) square. In order to achieve a long aspect ratio a serpentine channel was designed to fit into the illuminated square as shown in Figure 4-5.

The resulting channel is nearly 1 m long, and 4.5 cm wide, and is completely contained in the square window. This allows the entire channel to be uniformly illuminated by the solar simulator.

The channels were milled into a 1 inch (2.54 cm) thick Delrin (Acetal) block. The plastic provides thermal insulation of the hot feed and thermal mass to even out temperature variations that result from short time scale changes in mass flow rate in the system. The disadvantage of this design is that the system takes a long time to

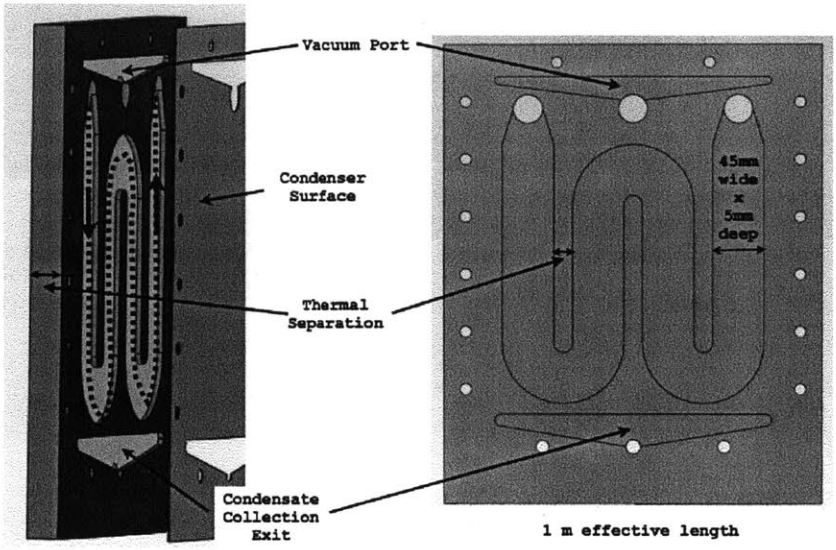

Figure 4-5: Serpentine flow channel in a square area.

warm up when adjusting the heat input.

The block containing the coolant channel contains features to access the air gap. A copper plate, which serves as the condenser surface closes the serpentine channel, but allows the permeate to pass into the coolant channel block and out of the back of the system. The module is oriented vertically with a slight tilt backward allowing gravity to assist the movement of condensate. The membrane spacer, which contains only two-dimensional features, allowing for easy manufacturing, spans the area between the vacuum port and condensate collection channel.

Both channel blocks, the condenser surface, and the gap spacers are sandwiched between two aluminum plates. The plates contain fittings for connecting the feed stream, extracting permeate, and reducing gap pressure. The front plate also contains a opening to allow a window for solar collection. Figure 4-6 shows each component in the experiment stack for the solar collecting system. For experiments without solar collection, the glazing frame and thin feed channel are replaced by a 1 inch (2.54 cm) thick Delrin block similar to the coolant channel, but without the condensate collection and vacuum port.

The primary membrane used was the a PVDF unsupported membrane made by Millipore (Immobillon PSQ). It was approximately 170 μm thick and had a nominal

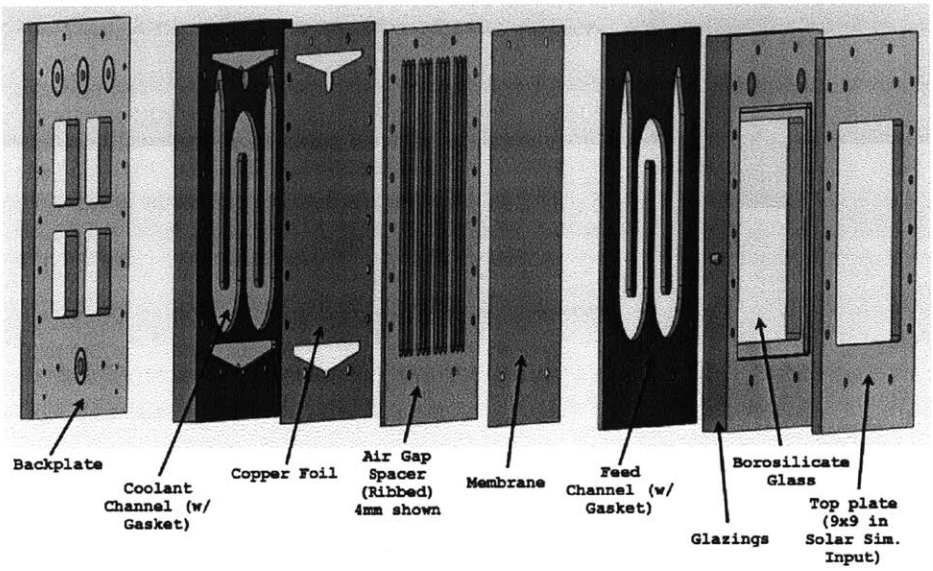

Figure 4-6: Components of MD module "sandwich".

pore size of 0.2 μm. The membrane distillation coefficient of 16×10^{-7} kg/m^2 Pa s was taken from prior work by Khayet et al. [34]. For the a reduced pressure test at 0.4 atm, a polyester supported PTFE membrane made by Pall Life Sciences was used. It too had a nominal pore size of 0.2 μm, but a thickness of 300 μm including its support layer. The membrane distillation coefficient of this membrane was scaled from comparison testing between it and the Millipore PVDF membrane in another setup, and was found to be 23×10^{-7} kg/m^2-Pa-s.

Once the stack is bolted together, an electric heater is added in-line in the feed flow stream between the coolant outlet and feed side inlet. Due to the area of the heater and the resulting surface heat flux, the top temperature of the system was limited to 70 °C to avoid boiling that occurrs on the surface of the heater at higher temperatures. Temperature measurement were accomplished by several threaded T-Type thermocouples from Omega (TC-T-NPT-G-72) using the standard calibration. The probes had an error of +/- 1 K for the temperature range considered.

A tank containing 10-13 ppt sodium chloride solution provided the feedwater for the experiments, and allowed conductivity to be used as a tracer measurement to detect leaks. The feed was circulated by magnetic drive pump (Little Giant PE-1.5-

MDI-SC). A second pump (Little Giant 3-MDX) circulated fluid through a fan coil radiator to maintain a consistent temperature in the feed tank.

Flow rate was controlled by means of a needle valve placed on the outlet before the brine reject returns to the tank. This valve captures most of the pressure drop in the system, keeping hydraulic pressure consistent inside the feed and coolant channels. The resulting positive hydraulic pressure kept the membrane flat in the channel, preventing non-uniformity in the flow and membrane area. This high pressure also made it easer to remove air that may be trapped in the serpentine channel. Feed flow rate was measured by taking a ballistic measurement, which involved collecting the output of the feed for 10 or 20 seconds and weighting the result on a balance of 0.1 g accuracy. Condensate was also collected and weighted periodically on the same balance to measure permeate flowrate. The completely assembled experiment (conventional heating) is shown in Figure 4-7

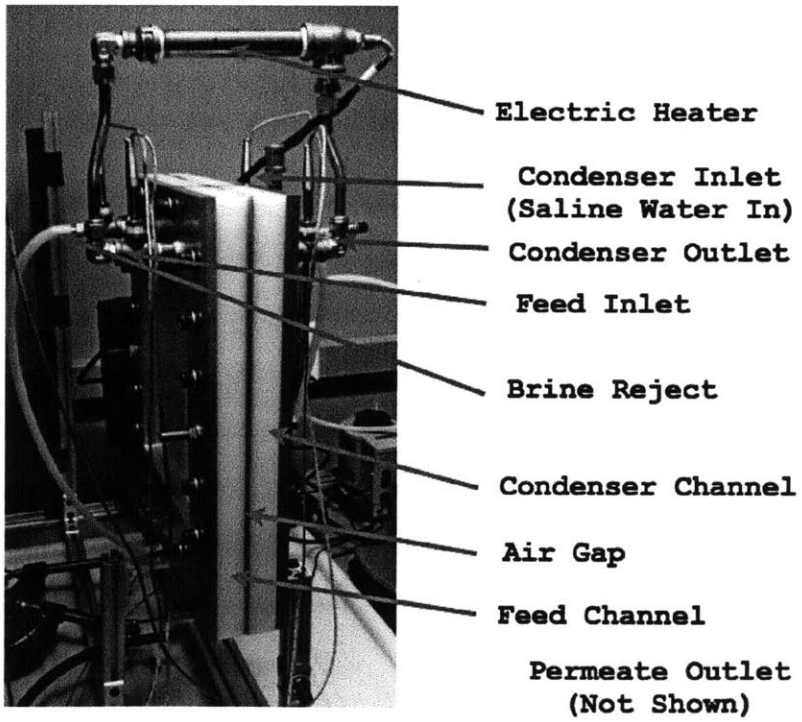

Figure 4-7: Assembled module configured to be heated at the top of the cycle.

During an experiment the whole setup was surrounded by 1 in (2.5 cm) thick foam insulation, limiting loss heat transfer coefficient to less than 1 W/m^2-K. The

operating parameters of the experiment are shown in Table 4.2.

Table 4.2: Experiment attributes and operating parameters.

Parameter	Value
Mass Flow Rate [kg/s]	0.0004-0.0024
Inlet Temperature, $T_{SW,in}$ [°C]	26-30
Top Temperature, $T_{f,in}$ [°C]	42-72
Heat Input, Q_{in} [W]	100-270
Length [m]	0.973
Width [m]	0.045
Flow Channel Depth [mm]	5
Gap Size [mm]	1.55
Membrane Material	PVDF or PTFE (0.4 atm gap pressure)
Membrane Dist. Coefficient, B [kg/m^{2}Pa s]	16×10^{-7}
Membrane Pore Size [μm]	0.2
Membrane Thickness [mm]	0.2
Spacer Open Area [-]	50%
Spacer Material	Polyproplyene

4.2.3 Solar Direct Heated Experiment

For experiments conducted with a solar absorbing membrane, the large feed channel block was replaced by a spacer comprising the flow channel and a frame holding two polycarbonate glazing panels which was placed over the flow channel spacer. Feed water passes between the inner glazing panel and membrane, bounded by the feed channel spacer. Figure 4-8 shows the device being heated by solar energy from a solar simulator.

Composite Membrane Design

To enable a conventional MD membrane to absorb solar energy, the highly reflective hydrophobic membranes needed to be treated in such a way to absorb solar energy or layered with another material that would provide the absorption while the MD membrane provides hydrophobicity. Because of the hydrophobic nature of MD membranes, using a liquid dye would be very difficult, so a composite membrane strategy was employed instead.

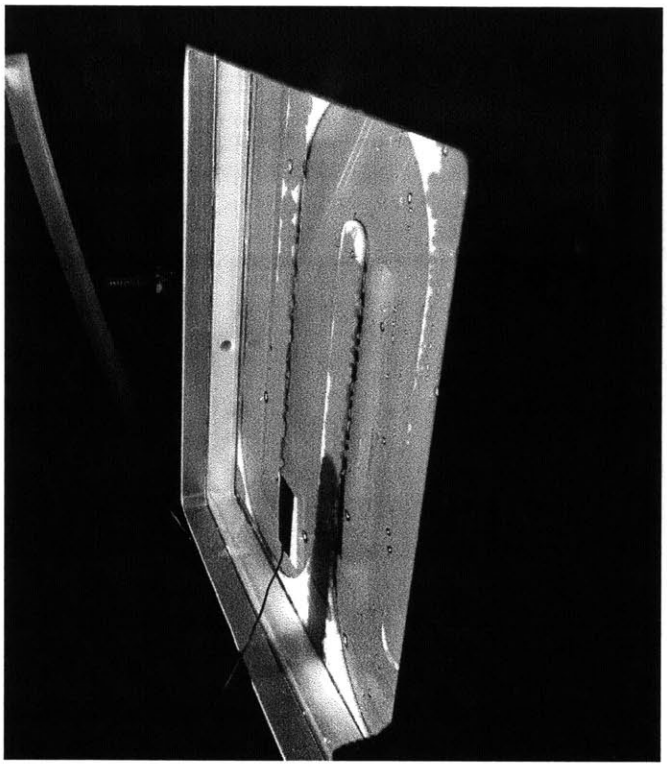

Figure 4-8: Assembled module with a composite membrane being heated by solar energy.

A variety of layering material were first selected for their black-colored appearance and ability to pass liquid. A selection of these materials were then tested in a Perkin Elmer Lambda 950 spectrophotometer for their absorptivity in the UV, visible, an infrared. Figure 4-9 shows absorptivity as it varies with wavelength. A standard solar spectrum is plotted for comparison.

As a result of this analysis, the Millipore HABP, a hydrophilic nitrocellulose based membrane, was selected. It had consistently high absorptivity across the range, and was highly hydrophilic, promoting the passage of water. Materials with higher absorptivity, such as the coated fiberglass or woven carbon fiber cloth, were far less permeable to water, and would add to the mass transfer resistance. Other hydrophobic membranes such as the mixed cellulose esters (MCE) and polycarbonate track etched (PCTE) membrane saw absorptivity drop sharply outside of the visible range and would fail to capture a large portion of the solar spectrum.

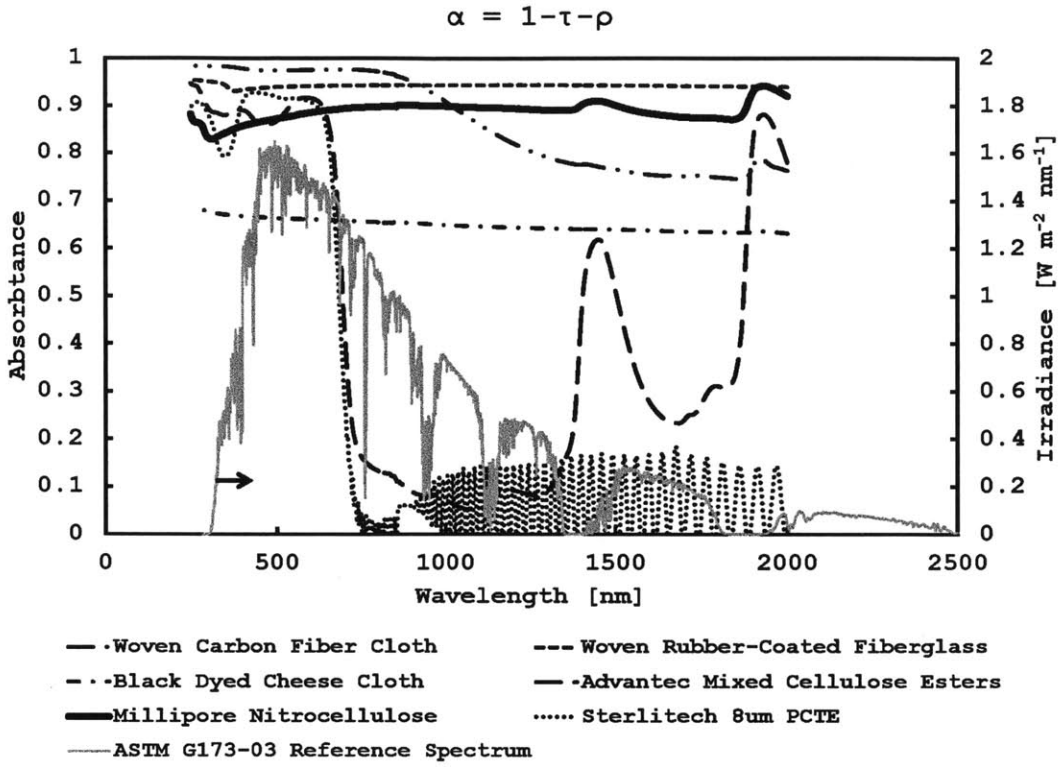

Figure 4-9: Absorptivity of several solar absorbing materials for a composite MD membrane.

4.2.4 Spacer Experimentation

In the course of developing the experiment, it was necessary to develop membrane spacers that could support the mechanical loads of large pressure differences (up to 0.6 atm). Several different spacer types were tested, with a mesh style proving to be the superior choice. The first iteration of spacer utilized open areas to maximize the area for vapor to pass through. Figure 4-10 shows the spacer in context of the module. The wider solid portions directly correspond to the division between the vertical parts of the serpentine flow channel.

However, these openings were too wide to maintain even a hydraulic pressure difference over the membrane of 14 kPa without the membrane sagging and contacting the condenser surface. This would limit the area available for vapor flow and lead to a non-uniform gap. The thin ribs in the spacer also suffered from buckling as the

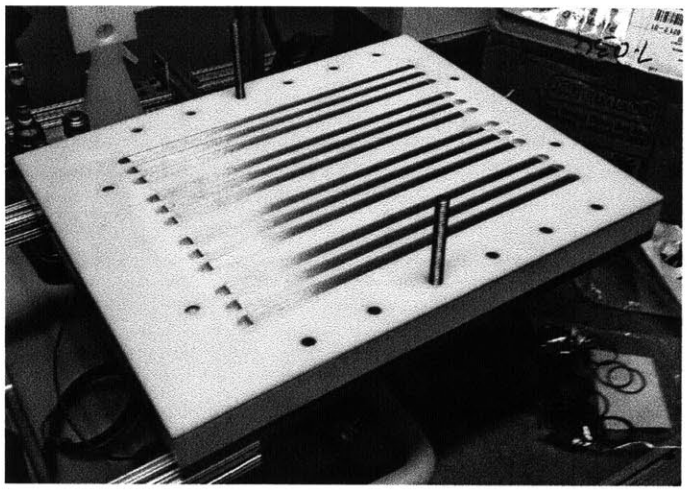

Figure 4-10: Open spacer placed over the condenser plate.

module heated up creating even wider gaps between ribs.

The next iteration retained the ribs, but narrowed the ribs and narrowed the gap between them to 3 mm. The bottom of the ribs were disconnected from the spacer frame, eliminating buckling due to thermal expansion. The increased frequency of ribs resulted in a spacer that was approximately 60% open. The spacer is shown in Figure 4-11.

While the ribs decreased the amount of vapor that could be passed through by masking off 40% of the membrane, it was able to stand up to the hydraulic pressure on the membrane; however, when the gap pressure was reduced, the membrane failed from being excessively stretched around the corners of the ribs.

Since mechanical support was highly important for the module to function at all, the final design was similar to what is used in high pressure RO systems, and utilized a woven mesh. A mesh was selected to be the same material and thickness as a standard polypropylene sheet. A frame was cut using a water jet cutter and a mesh was pressed into the frame. The resulting spacer was slightly less than 50% open, but supported the membrane more uniformly and eliminated sharp corners that could damage the membrane when strong differential pressure was applied. Figure 4-12 shows the spacer installed.

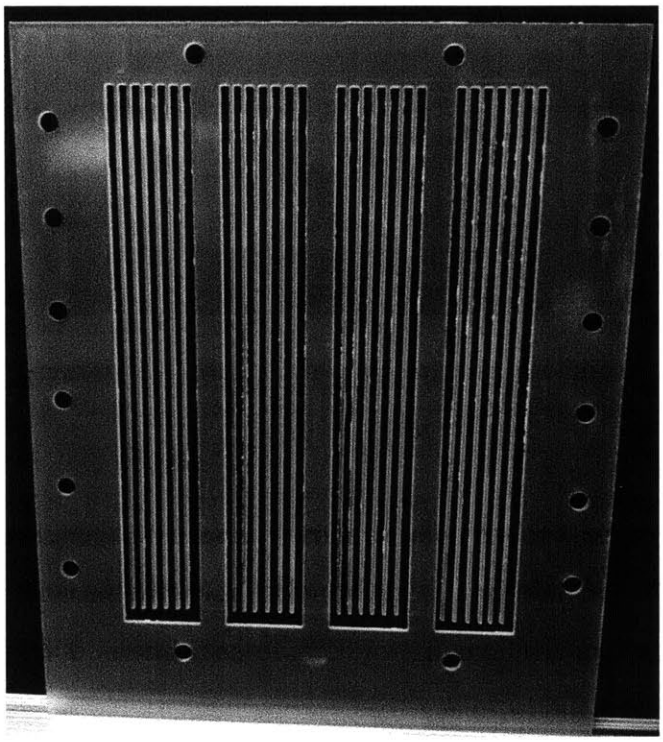

Figure 4-11: Narrow rib spacer, with higher rib frequency.

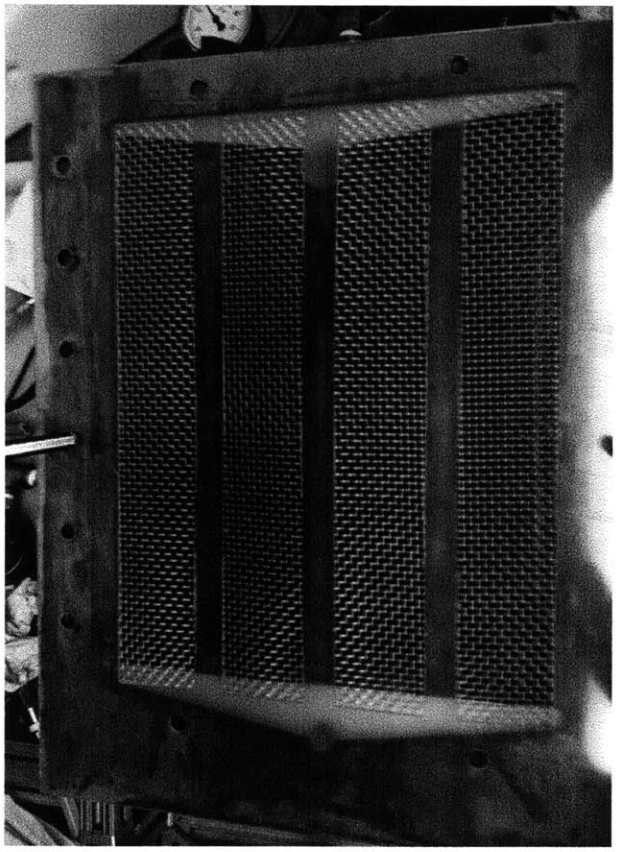

Figure 4-12: Screen spacer with support in both the horizontal and vertical directions.

4.3 Results

4.3.1 Validation and Reduced Pressure Gap AGMD

The first set of experiments was conducted to validate the detailed MD model in Chapter 2 and to test the improvement of GOR as the pressure in the gap was reduced. Measurements were made at successive heat inputs ranging from 100 to 270 W, at a mass flow rate around 0.0024 kg/sec.

To reduce the pressure in the air gap, the gap was connected to a vacuum pump and a two stage water column for pressure stabilization and measurement. A schematic diagram of the water column is shown in Figure 4-13. The first stage of the water column is capable of reducing the gap pressure to 0.7 atm, adding a second stage doubles that and enables pressure reduction to 0.4 atm. Due to the relationship between gap pressure and GOR, reductions below 0.7 atm have a greater impact, as shown by Figure 3-13.

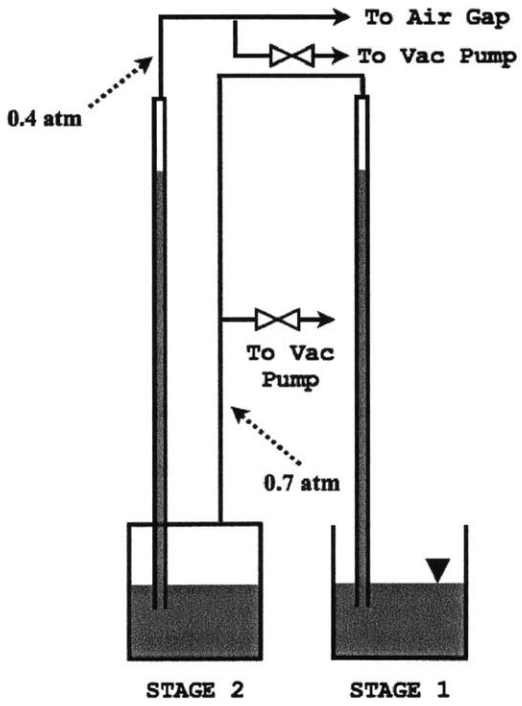

Figure 4-13: Two stage water column to reduce gap pressure to as low as 0.4 atm.

As the heat input was increased, top temperature and mass flow rate increased. The top temperature of the system was limited by the heat flux of the electric immersion heater, shown installed in a tube at the top of the experiment in Figure 4-7, such that the feed fluid would not boil at the surface of the heater. This limited the top temperature to 72 °C.

Figure 4-14 shows the variation of GOR with top temperature in the experimental system. A comparable GOR for an optimized large scale system is shown on the right hand axis.

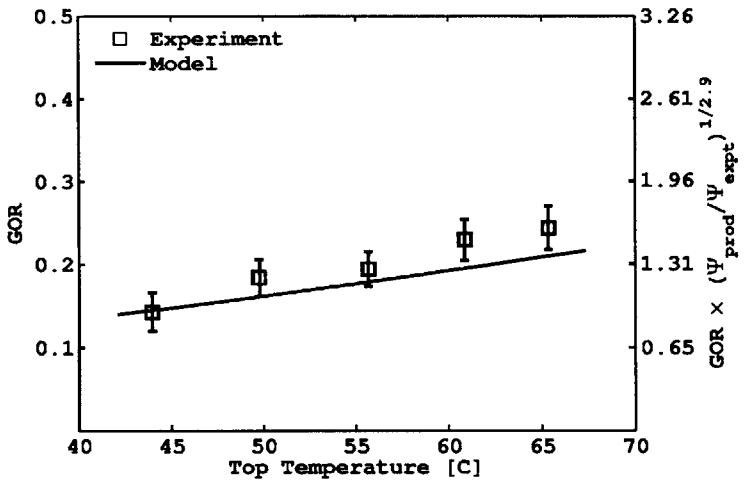

Figure 4-14: Comparison between experimental data and model for a conventionally heated AGMD system at atmospheric pressure.

Gap Narrowing Through Membrane Deformation

The results shown in Figure 4-14 demonstrate a consistent under-prediction of GOR by the model. For a system of a given membrane area and heat transfer coefficient, the analysis in the first part of this chapter suggests a strong effect of the gap size on overall performance. Because the membrane is subjected to a hydraulic pressure of up to 14 kPa gage, it will tend plastically deform and sag into the open spaces in the mesh. This has the effect of reducing the gap size, which in turn decreases diffusion resistance across the gap. The maximum amount of membrane depression was measured, and approximating the stretching as uniform over an opening in the

spacer, an average membrane depression value was calculated. The model was run again with the gap size reduced by this value. Figure 4-15 compares the model with membrane stretching to the one without.

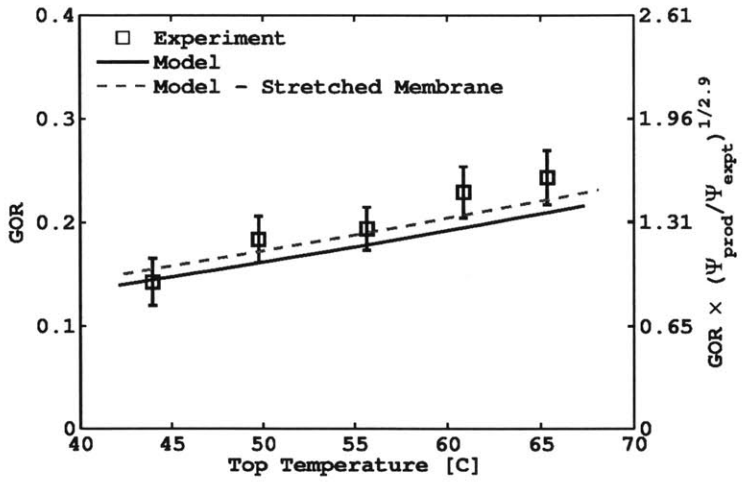

Figure 4-15: Comparison between experiment and models with and without stretching of the membrane.

The model agrees significantly better with experimental data once membrane stretching is taken into account. However since this is may not be uniform for all runs or membrane types, further model comparisons are made assuming the gap is at the full designed size.

Air Gap Pressure Reduction

Since GOR changes only slightly with a change in pressure up to 0.7 atm, reducing pressure in the gap only slightly will not have a large impact. This effect can be seen in Figure 4-16, which shows how GOR varies with temperature at various gap pressures.

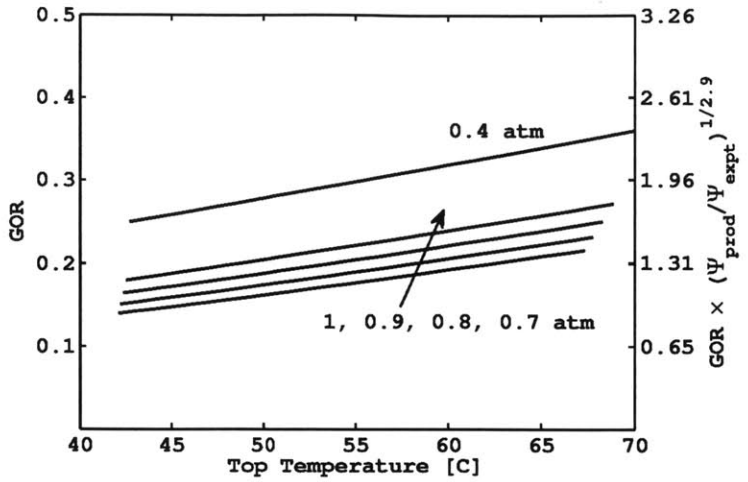

Figure 4-16: GOR vs. top temperature for various gap pressures.

Superimposing the experimental results at atmospheric pressure over Figure 4-16, pressure reductions for 0.9 and 0.7 atm fall within the experimental error. Experiments at slightly reduced pressure (0.9 atm) were attempted previously [56] and only a small enhancement of mass transfer was reported.

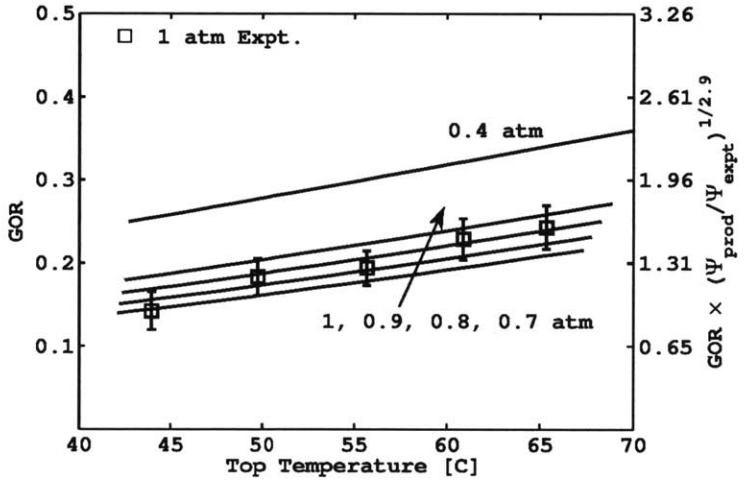

Figure 4-17: GOR vs. top temperature for various gap pressures compared to experimental results at atmospheric pressure.

As a result, reduced pressure experiments were conducted at pressures below 0.7 atm. Tests were done at an absolute pressure of 0.4 atm with the supported Pall PTFE membrane. The experiments are plotted in Figure 4-18.

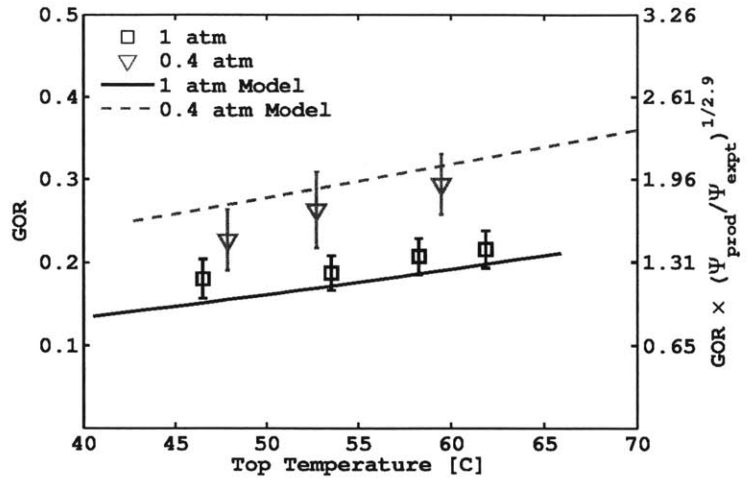

Figure 4-18: GOR vs. top temperature for atmospheric and 0.4 atm gap pressures compared to experiments.

Evident in these results are the differences between the membranes tested. The supported membrane did not stretch into the open spaces in the mesh, but did exhibit a constant leak rate under mechanical pressure. This leak rate was measured by taking the exact flow conditions as a typical test, but with the heater turned off. Verification by salinity measurements confirmed the collected fluid in these tests was entirely undiluted feed. The leakage rate was subtracted to obtain the results shown.

The benefits of pressure reduction can be more easily seen by comparing the recover ratio, or non-dimensional product flow rate, and reduced pressure. These data are plotted in Figure 4-19. This plot shows a clear benefit for reducing pressure in the gap as a means of enchaining energy recovery and increasing water output.

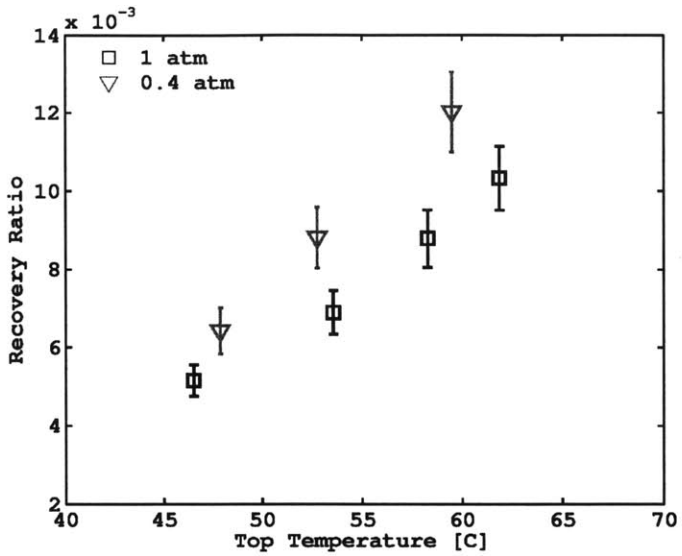

Figure 4-19: Recovery ratio vs. top temperature for atmospheric and 0.4 atm gap pressures compared to experiments.

4.3.2 Solar Direct Heated System

Tests of the novel directed heated concepts were performed on the bench-scale experiment.

In this system, the top temperature has less of an effect on system performance than the solar irradiation flux. As the heating is distributed, the top temperature does not necessarily occur at the inlet or outlet of the feed channel, and does not occur in the bulk fluid stream. As conventionally heated systems of any size operate at similar top temperature, small and large solar heated systems, are operated at comparable solar irradiation flux. The solar flux has a greater impact on temperature, and thus permeate flux, at lower feed flow rates.

Given the coupling of membrane area and solar collector area, membrane flux, J_m, is directly related to GOR:

$$GOR = \frac{J_m h_{fg} A_m}{I A_m} = \frac{J_m h_{fg}}{I} \tag{4.14}$$

Systems with comparable membrane flux have comparable energy efficiency, as they are only related by the constant factor h_{fg}, which is the same for a system of any area.

Representing the result in terms of permeate flux is clearer, because it is a directly measurable quantity and the experimental error is confined to the measurement error in flux alone, instead of being combined in the uncertainty in I. This serves the purpose of validating the models for direct heating of the membrane as well.

The solar simulator used (Newport 92190) provided a uniform (within 10%) solar flux, I, up to 750 W/m^2 for a 9 x 9 in square. Tests were also done at 580 W/m^2 using a lower lamp power supply setting.

Figure 4-20 shows tests conducted at both irradiation fluxes across a range of mass flow rates. In all the subsequent plots, the mass flow rates are normalized to the mass flow rate needed for the highest temperature in the system to be within 1 °C of the seawater inlet temperature, effectively providing no driving potential for evaporation, at the highest solar flux (750 W/m^2).

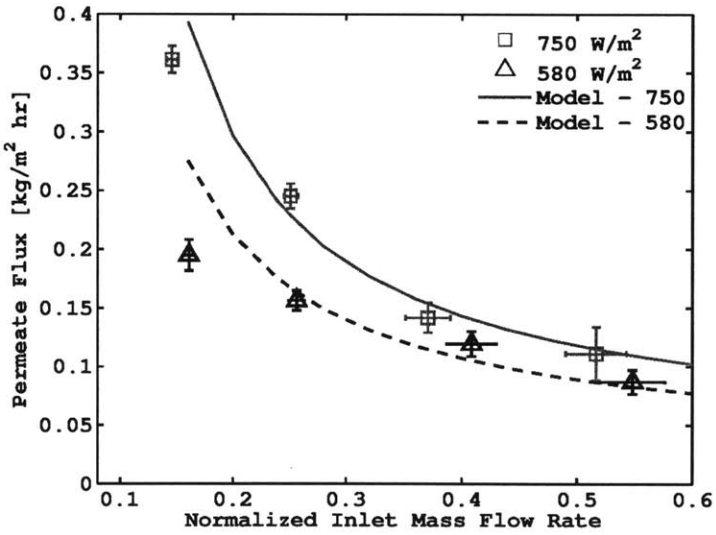

Figure 4-20: Flux performance of a solar direct heated system.

The experiments show broad agreement with the model. The narrow range of tests is primarily owing to the small scale of the experiments. Higher temperatures require lower mass flow rates, which are harder to control consistently with manually adjusted valves. Higher mass flow rates cause the feed temperature to drop, approaching the feed water inlet temperature, and eliminating the distinction between different solar

fluxes and decreasing permeate flowrate. Using a higher irradiation by bringing the simulator closer to the membrane would result in greater non-uniformity in flux, heating the inner channels significantly more than the outer ones. Calibration of the simulator for an average heat input of 1.8 kW/m^2 resulted in a the outer channels being heated an average of 25% less than the inner ones. Further reducing solar flux by reducing power to the simulator lamp would also the system lower temperatures too close to the feed water inlet temperature, resulting in low permeate flowrate.

The range of operating parameters shown in Figure 4-20 can provide a basis of comparison to demonstrate the importance of heating the feed at the point of evaporation. This model will be compared to several other solar heating configurations, schematically shown in Figure 4-21.

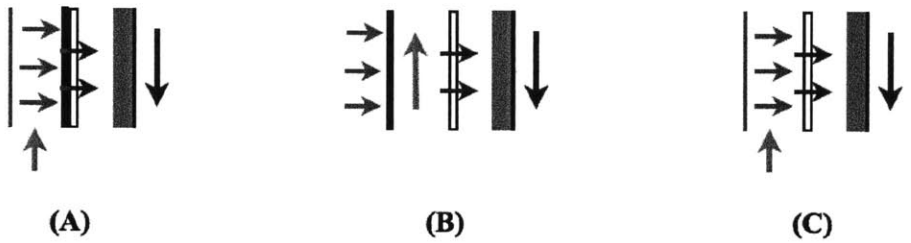

Figure 4-21: Various heating configurations tested for comparison: (A) a direct-heated composite membrane, (B) a heated plate above the fluid stream, and (C) a direct-heated plain MD membrane.

Figure 4-22 compares the performance of different heating schemes. From these experiments it is clear that heating at the membrane surface is superior. When compared to heating above the fluid stream (with a coated absorber plate), the effect of eliminating the heat transfer resistance from the bulk fluid stream to the membrane is clearly evident. There are also additional losses as the coated opaque absorber is closer to the environment. The effect of a solar radiation absorbing surface on the membrane is also apparent in this comparison. Since three times as much energy is absorbed at a the surface of the composite membrane than in the bulk fluid stream, a membrane without a solar radiation absorbing layer would reflect most incident radiation resulting in low heating and poor performance.

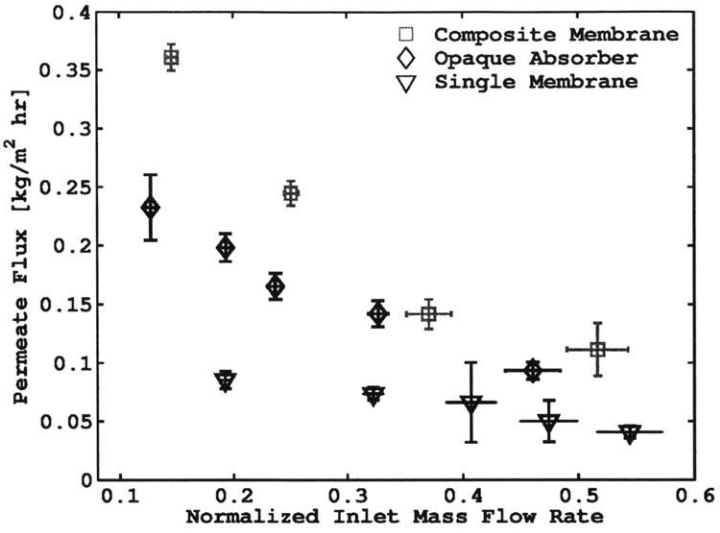

Figure 4-22: Comparison of different solar heating configurations.

4.3.3 Hot Brine Discharge Regeneration

The experimental apparatus can also be used to test the effect of recovering energy from the heated brine without recirculation. To accomplish this, a simple plate-frame counter flow heat exchanger is attached to the bottom of the module as shown in Figure 4-4. The heat input at the electric heater is then varied at a constant mass flow rate (approximately 0.0024 kg/sec) so that the system functions over a similar range of top temperatures with and without regeneration. The results are shown in Figure 4-23.

The data show the same trend, as exhibited in Figure 3-12, for a large optimized system. A model for the experiment here is not compared because the GOR is highly dependent on the terminal temperature difference of the heat exchanger. While this is measured and is used as in input in the model, the experimental error in the terminal temperature difference is large enough of significantly affect the model output, so a comparison with the model for validation purposes here would have little meaning. However, the increase in GOR is significant, which fits what would be expected for larger systems.

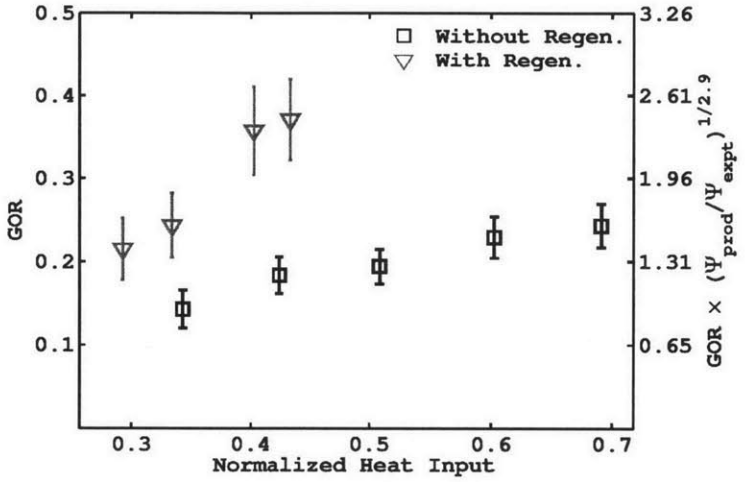

Figure 4-23: GOR vs. Heat Input for an conventionally heated system with and without regeneration.

Chapter 5

Applications

Using the detailed model in Chapter 2, a varicty of system sizes, configurations, and operating parameters can be explored. This allows for the optimization of MD systems for maximum energy recovery.

5.1 Parametric Study of MD Systems - Optimal Configurations

For comparisons of energy efficiency, the models in Chapter 2 were coupled with basic single stage cycle designs. The basis for the geometry of the module used for every configuration was one the designed by the Fraunhofer Institute [41] and tested in several real-world settings [6, 7]. This module is found in the majority of current solar-powered membrane distillation systems [20]. The dimensions were used in a simple flat plate module with the baseline attributes listed in Table 5.1.

In the system models, feed water is assumed to be extracted directly from the sea at 27 °C. Operation is steady and no storage or recirculation of the feed is used. Heat exchangers have no fixed size or heat transfer coefficient, but instead are taken to operate at a fixed terminal temperature difference (TTD). TTD is the minimum temperature difference between two streams in a heat exchanger, and a value of 3 degrees kelvin was assumed, which is common in practice. This ensures that the

Table 5.1: Module attributes of a baseline MD module.

Feed Mass Flow Rate, $\dot{m}_{f,in}$	1 kg/s
Membrane Material	Teflon (PTFE)
Length, L	10 m
Width, w	0.7 m
Flow Channel Depth, d_{ch}	4 mm
Porosity, ξ	0.8
Thickness, δ_m	200 μm
Membrane Distillation Coeff., B	16×10^{-7} kg/m^{2}Pa s
Thermal Conductivity, k_m	1.2 W/mK

GOR is not limited by the fixed size of a heat exchanger and the comparison is only between the MD configurations. Figures 5-1-5-3 show the flowsheets for these cycles.

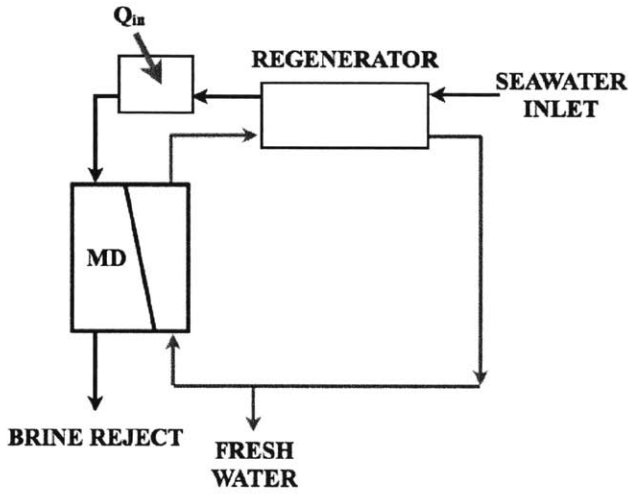

Figure 5-1: DCMD system flowsheet.

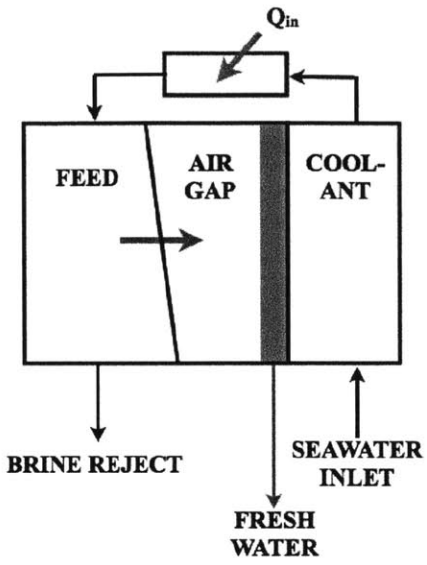

Figure 5-2: AGMD system flowsheet.

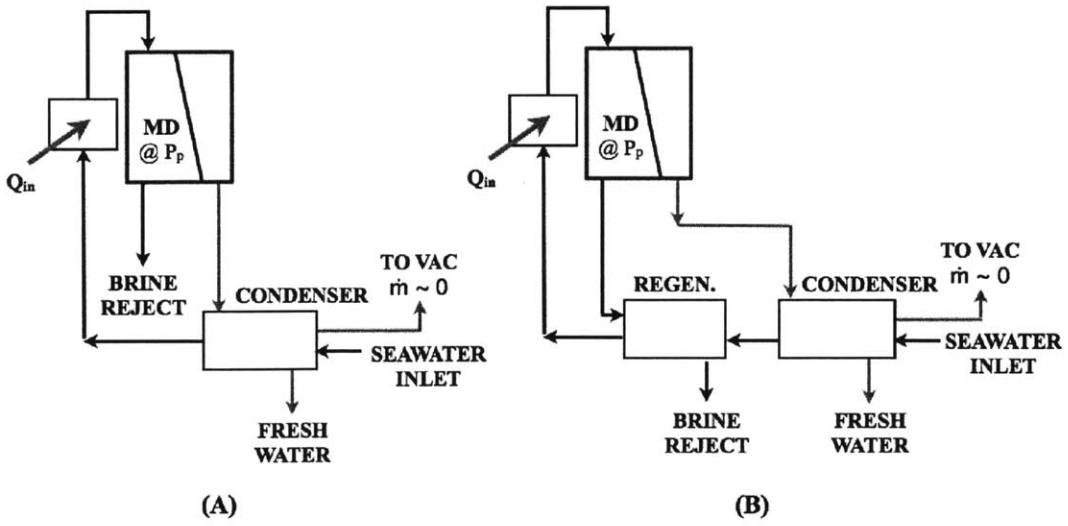

Figure 5-3: VMD system flowsheets, (A) without and (B) with brine regeneration.

Comparisons, shown in Figures 5-4 - 5-9, were made between the configurations (DCMD, AGMD, and VMD without brine regeneration) across the range of operating conditions (feed inlet temperature, seawater temperature, and mass flow rate), as well as module geometry (effective membrane length, flow channel depth, and air gap width). In VMD, the vacuum pressure is a dependent variable, changed to keep the terminal temperature difference in the condenser constant at 3 degrees kelvin. This pressure varied between 7 and 23 kPa. Convergence of the model could not be obtained for effective lengths beyond 40 m. The following figures show how GOR varies with respect to changes in these parameters.

5.1.1 Module Geometry

Figures 5-4, 5-5 and 5-6 show that module geometry and design can have a dramatic effect on GOR, particularly when considering the effective length. Increasing the length increases the area for heat and mass transfer. In DCMD and AGMD this increases the amount of energy that can be recovered, as fixed channel geometry fixes the heat transfer coefficient in the channel. With a shorter length, and thus a higher mean membrane flux carrying the latent heat of evaporation and permeate mass, the amount of energy passed through the membrane is very high requiring a larger temperature difference between the streams for a fixed heat coefficient. A larger temperature difference is also required to condense the larger amount of vapor. This increases the temperature difference at the feed inlet and permeate outlet, requiring more energy to be provided by the heater, and decreasing GOR. In DCMD and AGMD increasing the length increases GOR over a wide range. In VMD, however, this advantage is diminishing after a certain length, as the pressure difference, and flux, approach zero due to the feed temperature approaching the saturation temperature at the reduced permeate pressure. With no additional flux through the extra membrane, GOR remains constant. In AGMD another important resistance is the mass transfer across the air gap. This resistance drives up the temperature difference across the gap exponentially, as the mass carries the latent heat of fusion to the condensate layer. Narrowing the flow channel thickness increases the Reynolds number and convective

heat transfer coefficient, decreasing the heat transfer resistance in the channel.

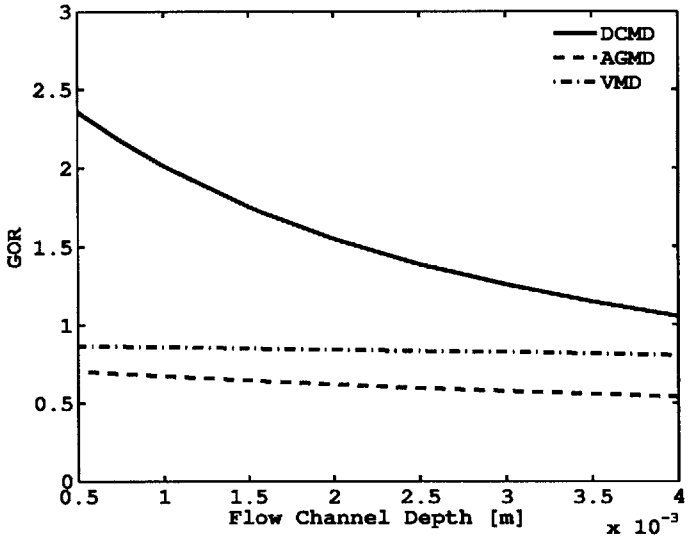

Figure 5-4: GOR as a function of flow channel height.

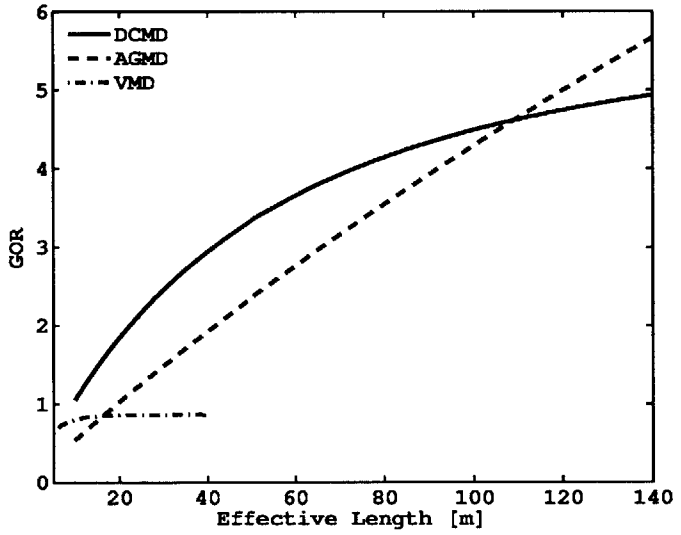

Figure 5-5: GOR as a function of length in the flow direction.

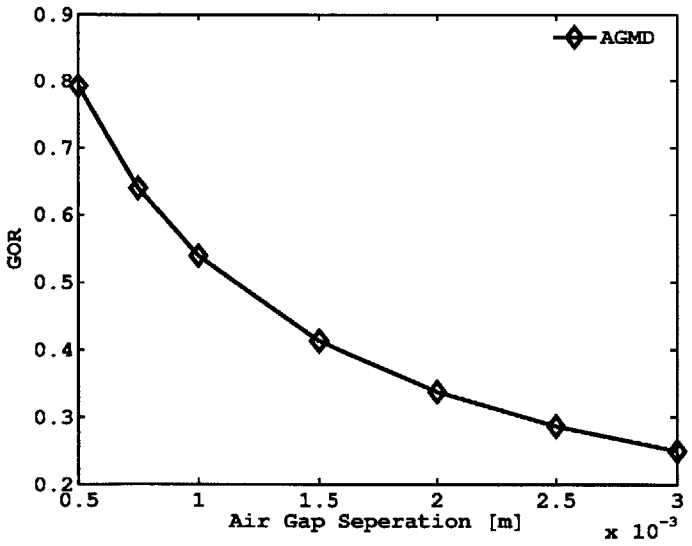

Figure 5-6: GOR as a function of air gap size in an AGMD system.

5.1.2 Operating Conditions: Temperature and Mass Flow Rate

GOR at varying operating temperatures is shown in Figures 5-7 and 5-8. Increasing the top temperature increases GOR despite the increased demand on the heater, as the greater flux is used to preheat the feed in DCMD and AGMD. The greater flux also increases water production for a net increase on GOR. Lowering the seawater inlet temperature creates more demand for heating without changing water production significantly for a fixed top temperature, and therefore the GOR decreases.

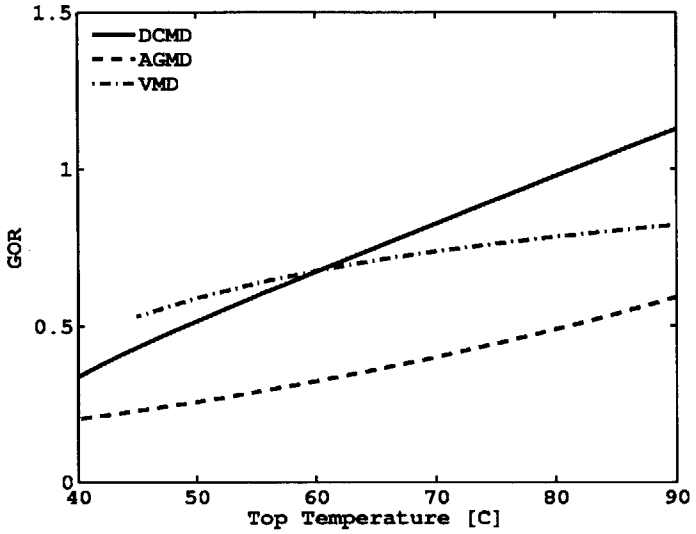

Figure 5-7: GOR as a function of top temperature, $T_{f,in}$.

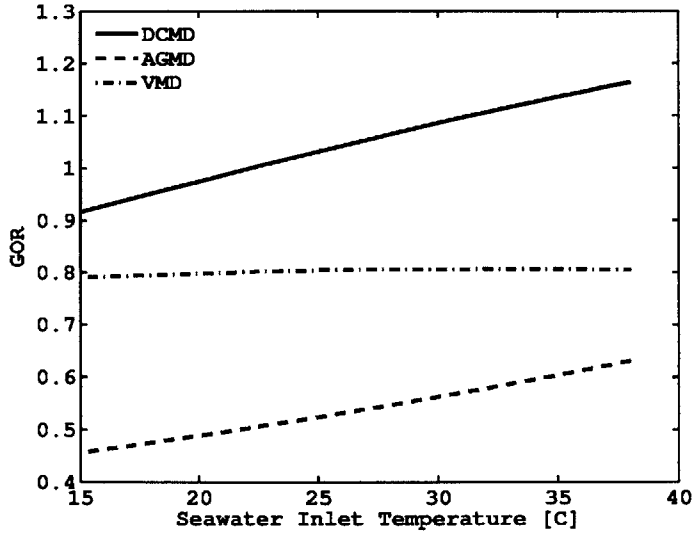

Figure 5-8: GOR as a function of bottom temperature, $T_{SW,in}$.

Figure 5-9 shows the effect of varying the mass flow rate. It shows that GOR can be maximized when the flow rate is low and energy required to heat the feed is minimized. For membranes 10 m long, mass flows under 0.2 kg/s yield relatively high GOR. After a certain mass flow, rate GOR goes below 1 and decreases slowly. This indicates that, for short membrane lengths, flow should be maintained in the laminar regime despite the increased heat transfer resistance. In AGMD, however, GOR is very high for a very low mass flow rate, as there is very little heat required to raise the feed to its top temperature. Unfortunately, the water production is extremely small, making this configuration impractical in the real world. Better results are obtained by increasing the effective length for a higher mass flow rate.

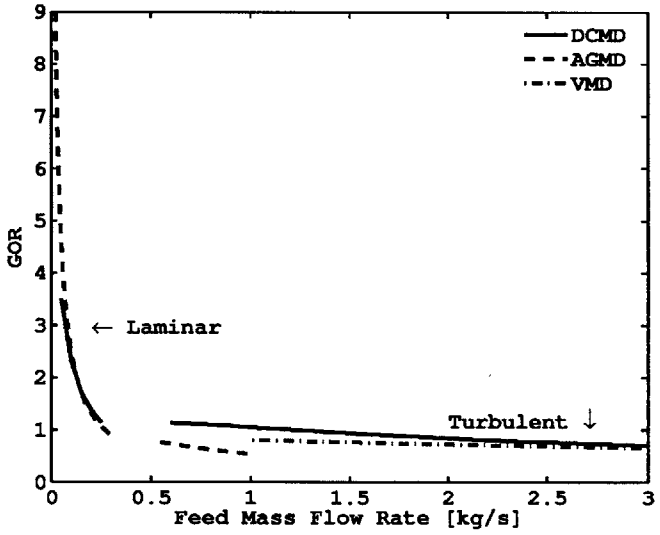

Figure 5-9: GOR as a function of mass flow rate. Gaps in lines indicates transition flow region, where heat transfer coefficient is not defined.

VMD, however, does not follow this trend, as all the vapor is condensed externally, not locally on a cool permeate stream or cooled condenser wall. Condensation in VMD is limited by the bulk saturation temperature at the reduced pressure, instead of the dew point temperature at the local water vapor partial pressure. Because DCMD and AGMD operate at atmospheric pressure, the dewpoint temperature can vary and can be locally higher than the mean saturation temperature, which corresponds to the permeate-side pressures typically found in a VMD system. Therefore, as pressure is reduced to increase flux in VMD, the amount of cooling water needed to condense the

permeate vapor without exceeding the saturation temperature minus the condenser terminal temperature difference becomes very large. Some of this incoming seawater can be rejected as excess cooling water, which decreases the load on the heater, but discards useful energy which otherwise could be returned to the feed. Thus, using excess cooling water results in no net effect on GOR. It can alternatively be passed through the heater, increasing the flux and water production; but in that configuration the heating requirement outweighs the energy recovery resulting in a net decrease in GOR.

5.1.3 Relationship Between Recovery Ratio and GOR

The proportional relationship between recovery ratio and GOR is demonstrated in Figure 5-10. For DCMD and AGMD systems which show a large increase in GOR with an increase in length, the recovery ratio increases as GOR increases. For very long lengths of the membrane, total water production goes down as the feed temperature, and evaporation potential decrease. However, the low membrane flux results in a very low saturation temperature difference between the feed side membrane surface and condensate-vapor interface in the gap to adequately condense, and the temperature difference across the heater decreases as result. This effect results in a net increase in GOR even as the recovery ratio levels off.

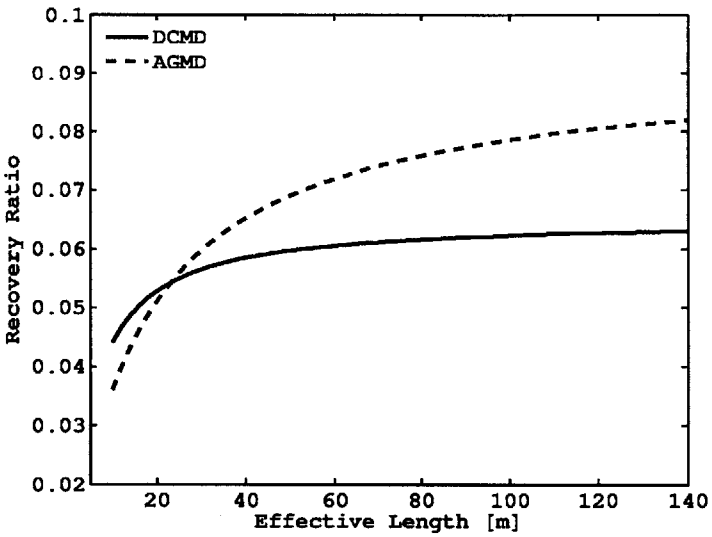

Figure 5-10: Recovery ratio as a function of length for DCMD and AGMD systems.

5.1.4 Comparison of VMD: Use of Brine Energy Recovery

Since the brine reject in a single-stage system exits at an elevated temperature, it would make sense to recover some of this energy and put it back in the feed. Ideally, all the energy would be recycled by brine recirculation with the injection of make up water to compensate for the fresh water generated. This is approximated in steady state by an ideal regenerator (no terminal temperature difference) as shown in Figure 5-3B. Comparison between a normal single stage VMD system and one with brine regeneration is shown in Figures 5-11 - 5-15.

These results demonstrate that, even with ideal brine energy recovery, the GOR of a reduced pressure VMD system reaches a limit of 0.93, which is far below what is expected to be needed for these systems to be economically viable [28]. This is because the low saturation temperature prohibits high temperature rise in the seawater inlet from energy recovery of the permeate vapor, which is essential for increasing GOR.

However, multi-staging may be able to overcome this limitation. Multi-staged systems create a smaller amount of vapor in each stage at descending permeate pressure. The cold seawater used to condense the vapor is passed in the opposite direction, gaining temperature as it heads to the first stage with the highest permeate pressure. This arrangement allows similar flux as a large single stage VMD, but the

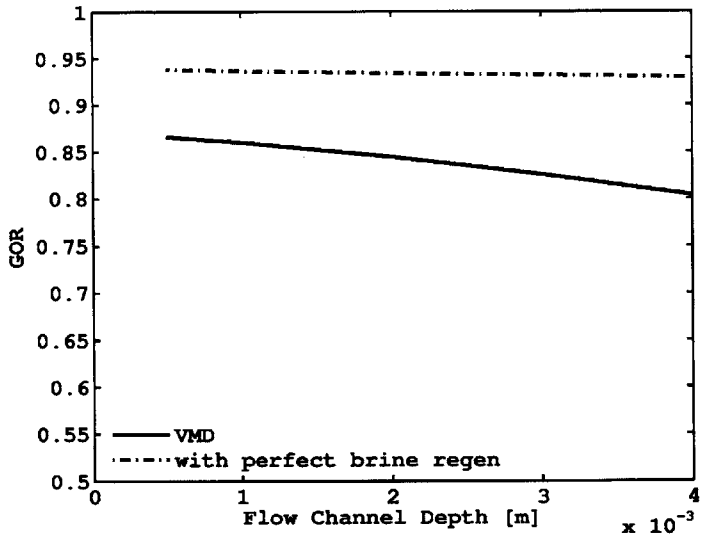

Figure 5-11: GOR as a function of flow channel depth in VMD systems with and without brine regeneration.

higher permeate pressures and corresponding higher saturation temperatures allow heat transfer into the cold seawater at higher temperature, reducing the amount of heating required. Recently, a system set up as a multi-effect distillation system which uses membranes to produce vapor instead of direct boiling, achieved a GOR of around 3 in 5 stages [12]. However, similar performance might be achieved in single stage AGMD and DCMD system, which may be less expensive to build, and would not require additional energy for vacuum pumps.

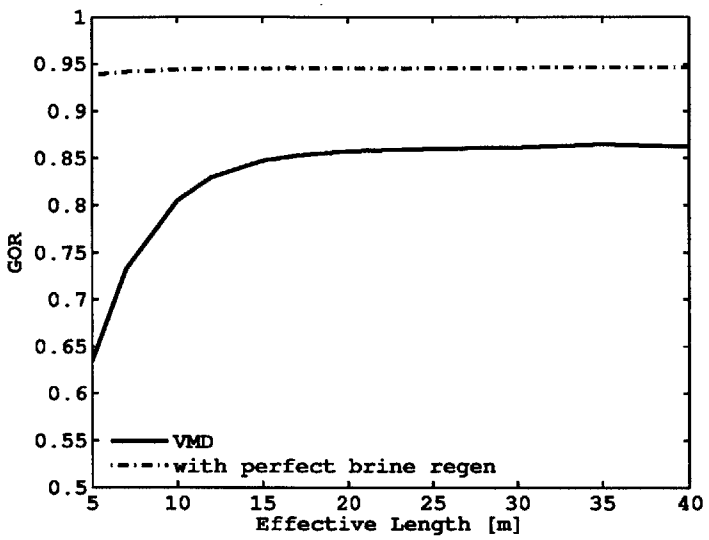

Figure 5-12: GOR as a function of effective length in the flow direction for VMD systems with and without brine regeneration.

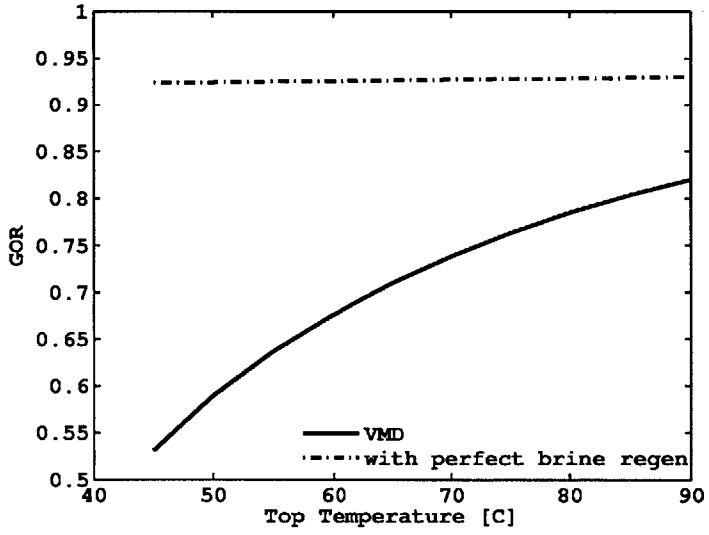

Figure 5-13: GOR as a function of top temperature ($T_{f,in}$) for VMD systems with and without brine regeneration.

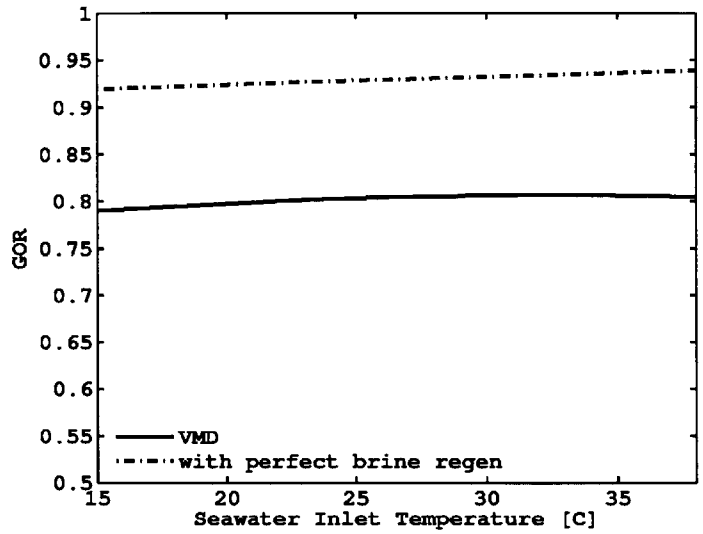

Figure 5-14: GOR as a function of bottom temperature ($T_{SW,in}$) for VMD systems with and without brine regeneration.

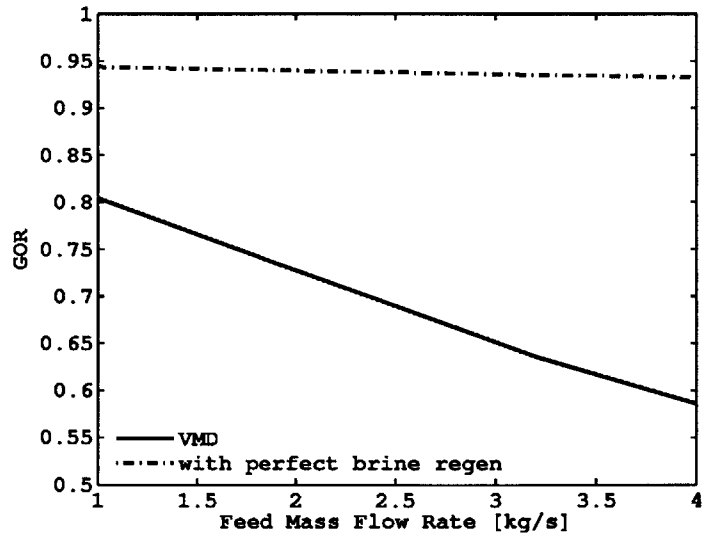

Figure 5-15: GOR as a function of mass flow rate in VMD systems with and without brine regeneration

5.2 Large-Scale Solar Direct Heated AGMD

The model presented in Chapter 3 can be used to design large scale solar MD distillation systems, which can rival the performance of other means of solar-thermal desalination.

Energy efficiency was tested by modeling the complete cycle for systems with and without heat recovery from the brine (Shown in Figures 3-6 and 3-7 respectively.). Lessons on optimal module designs from previous work [52] were applied to the baseline design for modeling the current system. Table 5.2 shows baseline operating conditions.

Table 5.2: Baseline Properties of a Solar Heated AGMD Module

Module Geometry		**Membrane**	
Effective Length, L	145 m	Membrane Dist. Coeff., B	16×10^{-7} kg/s m^{2}Pa
Width, w	0.7 m	Porosity	0.8
Channel Depth, d_{ch}	4 mm	Thickness	200 μm
Air Gap, δ_{gap}	1 mm	Conductivity	1.2 W/m K
Operational Parameters		**Solar Collection**	
Mass Flow, $\dot{m}_f$,$\dot{m}_c$	1 kg/s	Irradiation	850 W/m^2
Seawater Temperature, $T_{SW,in}$	20 °C	Concentration Ratio	1
		Glazing Separation	20 mm
		Glazing Thickness	2 mm
		Glazing Emissivity	0.8
		Combined ($\tau\alpha$) Product	0.8

Under these conditions, pressure drop in the flow direction is between 3.5-4 atm. For comparison, the liquid entry pressure of a moderately hydrophobic membrane with a contact angle of 120° and a pore diameter of 200 nm is around 6.6 atm, allowing the membrane to withstand such hydraulic pressures even if it contains pores that are larger than the mean pore diameter.

As this device relies on solar energy, the energy efficiency as measured by GOR can be calculated in two ways: The heat input can be taken to be he incident solar radiation, thereby accounting for all the losses in the solar collection step, which for systems that use external solar collectors is captured by the collector efficiency. The heat input can be taken to be the energy provided to the fluid, which excludes the

collection inefficiency and heat loss from the device. Both versions of GOR are defined in Equation 5.1:

$$GOR_1 = \frac{\dot{m}_p h_{fg}}{IA} \tag{5.1a}$$

$$GOR_2 = \frac{\dot{m}_p h_{fg}}{((S + S_f) - \bar{q}_{loss})A} \tag{5.1b}$$

One sun represents 850 W/m^2, the daily mean radiation for summertime in a desert climate. The system was modeled at a variety of percentages of that amount. When the heat input was taken to be the incident solar irradiation, GOR for this system was on the order of 1, which is in line with existing solar desalination technologies. When the heat input is the heat that is absorbed by the fluid the GOR can approach 3, which is competitive with commercial MD systems [12]. In this cycle, the feed side membrane temperature varies a great deal and goes quite low, as the coolant inlet is fixed at the cold seawater temperature. As a result, the potential for evaporation is reduced and high concentration ratios are required to achieve good performance as shown in Figure 5-16. However GOR improves significantly for a given concentration by using a recovery heat exchanger.

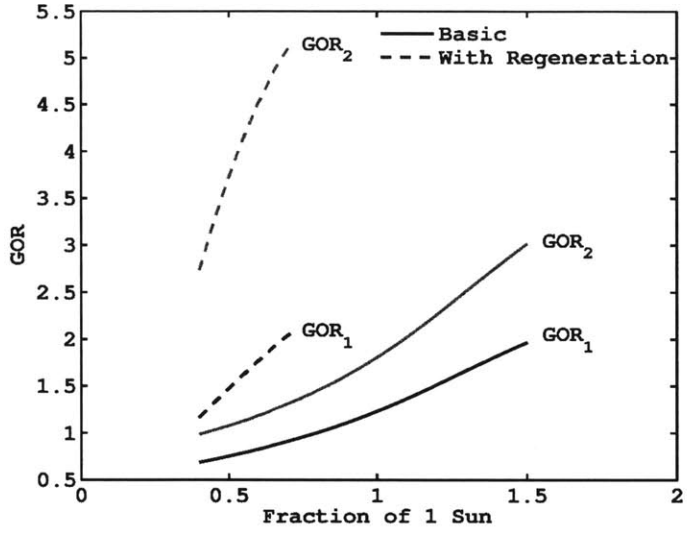

Figure 5-16: GOR as a function of degree of solar concentration with and without brine regeneration.

Figure 5-16 shows how the energy efficiency of this system varies with heat input. Overall the system with regeneration performs better for a given amount of energy input, especially when the heat input to the fluid is used as a basis for GOR (GOR_2). This has the distinct advantage of eliminating the need for concentrating collectors, and performing better during low solar insolation periods, such as dawn and dusk.

5.2.1 Comparison of GOR Between Different Solar Heating Configurations: A Simple Direct Heated System

To better understand the energy efficiency behavior of a system where the solar collection area is coupled to the distillation membrane area, two different methods of solar collection are compared with conventional cycle heating. The conventional cycle was heated with a separate 42% efficient solar collector array. The array was composed of Xianke XKPH58-30 evacuated tube liquid heating collectors, one of the best solar collectors for heating at high temperatures as rated by the Solar Rating and Certification Corporation [57]. The efficiency figure of 42% assumes operation at peak efficiency. Figure 5-17 shows results over a range of feed inlet temperatures. The

MD module in this example has an extremely basic design, and does not make use of very small air gaps, or vacuum between the glazings. The attributes and operating conditions are shown in Table 5.3.

Table 5.3: Attributes and operating conditions of a simple one-piece solar MD desalination system.

Parameter	**Value**
Solar Flux	750 W/m^2
Feed Inlet Mass Flow Rate	1 kg/s
Length	145 m
Width	0.7 m
Flow Channel Depth	5 mm
Gap Size	1.5 mm
Spacer Open Area	50%
Glazings	Double Glazed, Non-evacuated

Performance of direct heating is superior to external heating for all temperatures, despite the fact that the membrane could be more throughly insulated if it was decoupled from the solar collection. However, this is offset by the inefficiency of the collector array itself, not including losses from the additional piping required to deliver the hot fluid to the membrane module. For the opaque absorber over the fluid, which is similar to a configuration studied by Chen and Ho [46], losses are greater as a result of the absorbing surface being closer to the environment, and the driving force for evaporation is reduced due to additional temperature polarization.

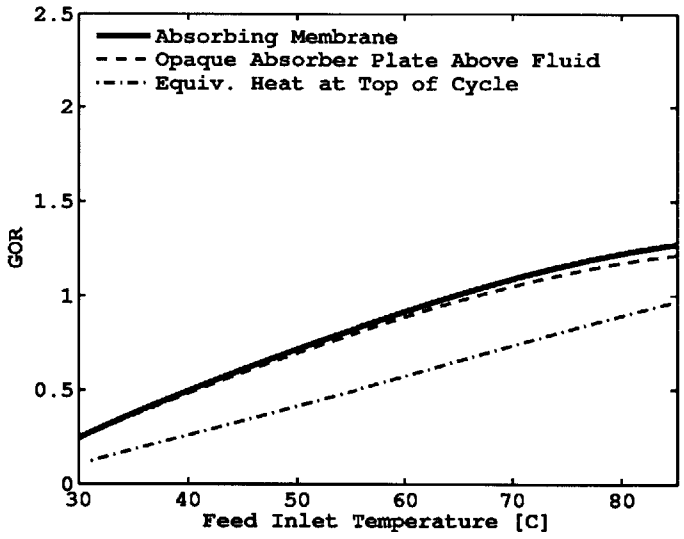

Figure 5-17: GOR as a function of feed inlet temperature for two different solar direct heating configurations and conventional heating.

These results suggest that direct heated membrane could be a viable alternative to, and an improvement on, traditionally solar heated systems that are discussed at the beginning of this thesis.

5.2.2 Conclusions

This device shows promise in improving solar powered desalination in a simple, effective single or two-piece device. It has the advantages of integrating solar collection into a single device, and delivering heat directly to the source of evaporation, reducing temperature polarization, and increasing vapor flux. A simple liquid-liquid heat exchanger can be added to improve performance, allowing the device to function well during low insolation periods. This device has the potential to achieve performance that exceeds both that of existing solar stills and that of more complex solar powered MD systems by over 25%.

5.3 MSF-Competitive Multi-Stage VMD System

A large scale multi-stage VMD system has the potential to be competitive with MSF, but with all the advantages of MD as outlined in Chapter 3.

For the comparison, and in a compromise between summer and winter performance, the seawater inlet temperature is set at 20 °C. The feed top temperature is set at 95 °C, which is near the upper limit for MD systems. A once-through MSF system with the same process flow shown in Figure 3-10 is used where the membrane modules are replaced by an isenthalpic flashing process at the same pressure. The decrease in vapor saturation temperature from stage to stage (called ΔT_{flash} in MSF systems) is 3 °C. Saturation temperature determines the pressure in each module, P_p.

Optimal membrane sizing and flow rates were taken from results of the parametric study of VMD systems in the first section of this chapter. The membrane module was designed to produce the maximum amount of vapor at a given permeate pressure. The maximum amount of vapor is produced when the feed temperature exiting the module is reduced to the saturation temperature at the given module pressure, P_p, and the driving potential for evaporation is zero. As a result, membranes were short in the flow direction with 400 sheets in parallel such that the feed reaches the saturation temperature at the end of the module and no non-productive membrane is used. If the difference in saturation pressure between each stage is equal then the optimal module design for one stage should be close to optimal for all other stages. Feed flow channel size was chosen to balance heat transfer coefficient (to minimize temperature polarization) and pressure drop. A full list of system parameters for the two modeled systems can be found in Table 5.4.

Table 5.4: Parameters for MS-VMD system and MSF equivalent

Operational Parameters		Membrane Module	
Inlet Mass Flow Rate	3 kg/s	Length	2 m
Top Temperature	95°C	Width	0.15 m
Seawater Inlet Temperature	20°C	Flow channel depth	2 mm
Number of Stages	20	Membrane thickness	200 μm
ΔT_{flash}	3°C	Pore size	0.2 μm
Condenser Effectiveness	0.98	Number of parallel sheets	400
Cooler Effectiveness	0.96	Membrane distillation coeff., B	16×10^{-7} kg/m^{2}s Pa

5.3.1 Energy Efficiency Comparison

Using GOR as a measure of overall system energy efficiency, MD and MSF system performance show comparable performance for a membrane module that is optimally designed to produce the largest amount of vapor possible. This makes the end states of the evaporation process in MS-VMD similar to the end states of the evaporation (flashing) process in MSF, with the resulting vapor produced in MS-VMD exiting the module slightly superheated, as vapor near the feed inlet is produced at a temperature slightly above the saturation temperature for that stage (Vapor at the feed inlet is produced near the saturation temperature of the previous stage). For the operating conditions given above and the same number of stages, multi-stage VMD has very similar performance as measured by GOR as shown in Figure 5-18. Performance for a non-optimal membrane module, which contains a quarter of the membrane area of an optimized module, is also shown. Performance is significantly lower, demonstrating the importance of module geometry in achieving superior system performance.

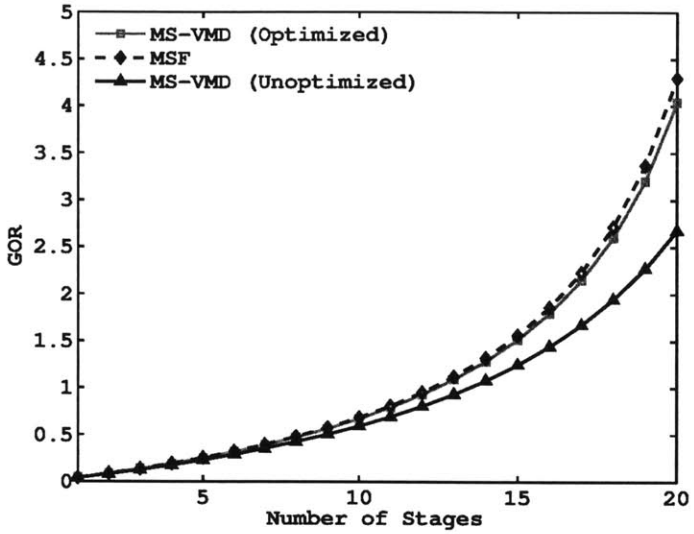

Figure 5-18: GOR as a function of the number of stages in an MS-VMD process compared with MSF and a MS-VMD system with a quarter of the optimal membrane area.

As with MSF, performance is greatest for a large number of stages. The number of stages is restricted by the top and bottom temperatures of the system, effectiveness of the heat exchangers, and ΔT_{flash}. Decreasing ΔT_{flash} allows a greater number of stages and slightly higher thermal performance; however, equipment cost would increase.

A similar trend in the recovery ratio is observed, as shown in Figure 5-19. The results show a significant increase in recovery ratio, in line with those found in larger thermal systems.

5.3.2 Irreversibility Comparison - Entropy Generation

Another way to evaluate the performance of the MS-VMD is to look at the rate of entropy generation compared to similar components in MSF. Here a 20-stage system for both MS-VMD and MSF with the parameters described in Table 5.4 will be used. Specific entropy generation in a stage is defined as the total entropy generation divided by the flowrate of fresh water permeate produced in that stage. Entropy generation is defined as the difference between the flows, i, of specific entropy going in and out

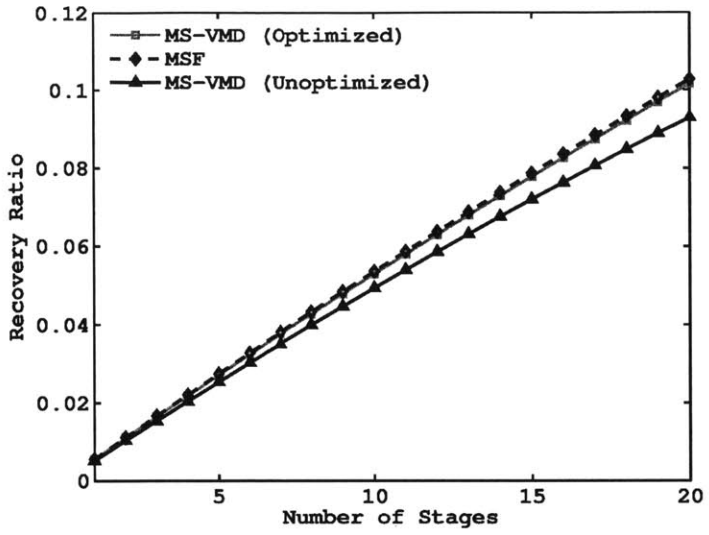

Figure 5-19: Recovery Ratio as a function of the number of stages in an MS-VMD process compared with MSF and an MS-VMD system with 1/4 of the optimal membrane area.

of the control volumes shown in Figure 5-20.

$$\dot{s}_{gen} = \frac{\sum_i \dot{m}_{out,i} s_{out,i} - \sum_i \dot{m}_{in,i} s_{in,i}}{\dot{m}_p} \tag{5.2}$$

Figure 5-21 shows a breakdown of specific entropy generation for each system. For MS-VMD, the evaporation of water through an MD membrane replaces the vapor flashing process in MSF. Despite the small pore sizes in an MD membrane, which would lead to a great deal of mass transfer resistance, and thus high irreversibility, the vapor flashing process is comparably irreversible. In fact, the production of vapor in and MD process is less irreversible than a flashing process, but produces superheated vapor. The difference between a MS-VMD system with an optimized module and MSF arises from the fact that this superheated vapor, leads to additional entropy generation in the condensation step, slightly lowering GOR. The greater source of irreversibility overall comes from the condensation and cooling process, which could be targeted for improvement; for example, by using a more effective condenser, or using more stages and decreasing ΔT_{flash} to minimize the temperature gradient between

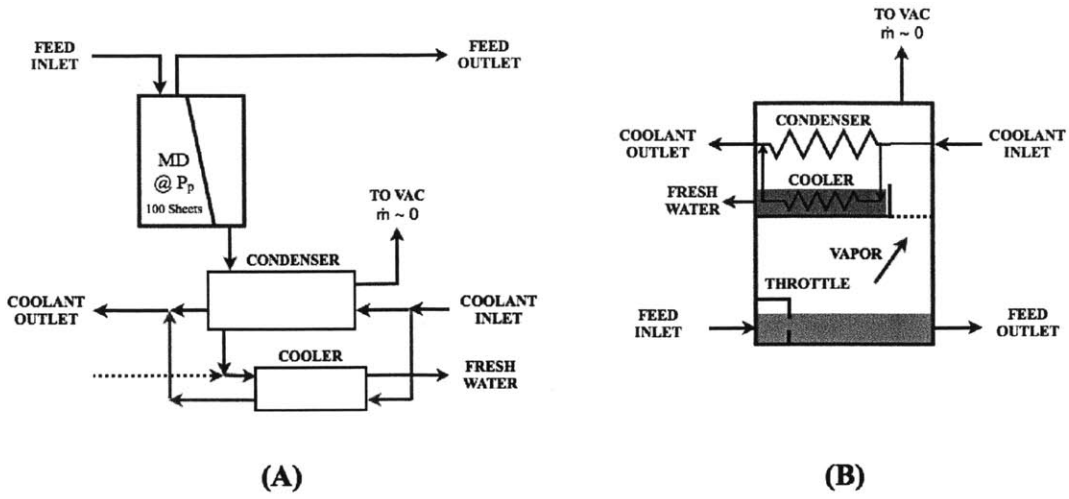

Figure 5-20: Control volumes for comparison of entropy generation. (A) A MS-VMD single stage, and (B) a MSF stage with the same components. Specific entropy is evaluated at the inlets and outlets shown.

the vapor and condenser.

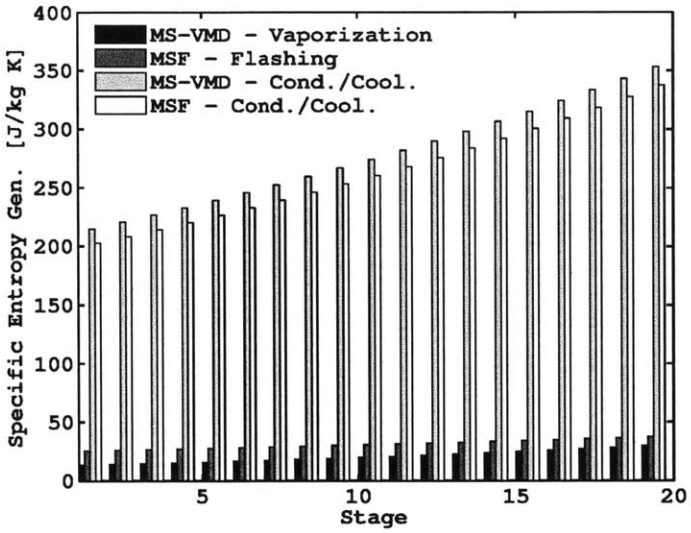

Figure 5-21: Irreversibility comparison between a conventional once-through MSF system and the MS-VMD process.

5.3.3 Conclusions

Analysis from both energy efficiency (GOR) and irreversibly (entropy generation) perspectives clearly demonstrates the viability of MS-VMD for scalable, and potentially reduced cost, water desalination. Using entropy generation analysis it can be shown MD modules produce vapor more efficiently. However, due to the production of slightly superheated vapor in an MS-VMD systems, the temperature gradient between the vapor and condenser is larger, leading to more irreversibly in the condensation and cooling steps. This balances out the more efficient production of vapor to produce a MS-VMD system that is overall very comparable in energy efficiency to MSF, with the benefits of a more scalable system, the use of inexpensive polymer materials, and the use of lower energy heat sources, such as solar energy.

Chapter 6

Conclusions

This thesis has presented mathematical models for the commonly used configurations of membrane distillation used in desalination: direct contact, air-gap and vacuum. These models have been validated with available experimental data published in literature. Air gap membrane distillation was selected for its potential for improvement and superior heat transfer qualities.

Several novel MD concepts aimed at enhancing the energy efficiency of the membrane distillation process, including the use of solar energy to directly heat the point of evaporation in an air gap MD system, and well as a multi-stage configuration to enhance energy recovery in vacuum membrane distillation. Measures to enhance the performance of an MD system were also evaluated; the use of an energy recovery heat exchanger on the hot brine discharge to enhance efficiency while preventing brine concentration, and reduction of pressure in the air gap to aid diffusion.

An experimental air gap membrane distillation apparatus was developed to test both solar heated and conventionally heated systems, and to test the novel concepts developed.

6.1 Modeling

The model provided a means of assessing the performance of a wide variety of systems. When applied to the design of MD systems the following conclusions can be reached:

- Single stage VMD, utilizing a permeate stream of pure vapor, is inherently limited by the low temperature of condensation which results from reducing the pressure. This makes it hard to heat the brine to a high temperature in the condenser, and to recover heat efficiently. As a result, the GOR of single stage VMD systems is limited to less than 1, even with ideal heat recovery/recirculation of the brine reject.

- AGMD and DCMD have the potential for high GOR if properly optimized. Local condensation of vapor allows for heat transfer at high temperatures improving heat recovery.

- In these systems, GOR is raised by long effective lengths, and low flux, which keep resistances to heat and mass transfer small.

- In AGMD, the gap width has the greatest impact on GOR. This demonstrates that diffusion across the gap is the limiting resistance that governs the performance of most AGMD systems.

- Reducing gap pressure can have a comparable effect to reducing gap size, and can significantly enhance the performance of systems with small air gaps (on the order of 1 mm)

Utilizing multi-staging in the style of an MSF system can overcome the performance limitation of VMD, and offer comparable performance to MSF in a far more compact size.

The model can be modified to guide the design of a solar-direct heated AGMD system, which is has the potential for superior energy efficiency when compared to current solar thermal heated desalination systems.

Given the superior heat delivery mechanism in a direct-heated system, a well designed direct-heated system will outperform a system heated with a separate solar collector array by over 1.25 times if the array has an efficiency as high as 42%, which represents the most efficient high-temperature solar heaters available today.

6.2 Experimentation

An experiment was used successfully to test the MD process over a variety of operating temperatures and flow rates. Experiments for both a conventionally heated and solar direct-heated AGMD system showed reasonable agreement with the model.

Relating the performance of systems with different membrane areas, operating temperatures, mass flow rates, and heat transfer coefficients is easily accomplished with a single non-dimensional parameter, Ψ, derived from a simplified form of the governing equations. A simple polynomial relationship relates performance with Ψ allowing a bench-scale experiment to predict the performance for a wide variety of systems, optimized or otherwise, provided that experiment is tested with the same membrane and gap size.

The experiment revealed important real-world limitations and features of the operation of an MD system.

Due to the sensitivity of the AGMD system to the gap size, the spacer design had a profound effect on performance. Spacers had a to support a membrane adequately under the hydraulic pressure of the feed pressure and any reduced gap pressure without tearing the membrane or causing it come into contact with the condenser surface. However, despite the selection of a gird spacer with only 50% open area, there was a slight amount of membrane deformation into the gap, which causes the model to under-predict the performance of the experiment, which, as a result of the deformation, has an effectively smaller gap size. Reducing the gap size in the model to account for this deformation leads it to more accurately predict performance of the experiment. This stretching could be a design feature; improving performance in other systems provided the membrane is sufficiently strong to stretch without tearing on the spacer.

Under reduced pressure membranes with an integrated support layer worked better, as they did not stretch into the openings in the gap spacer, and agreement with the model was generally better. Reduced gap pressure shows demonstrated superiority in permeate mass flow rate, and thus energy efficiency in an air gap system.

While reducing the pressure allows for the construction of larger gaps without sacrificing energy efficiency, it is more suited to improve the performance of a system with a small air gap. The additional cost of pressure reducing equipment has to be weighed against the performance improvement from a gap pressure reduction, depending on the overall design of the system.

Tests of the solar direct heated system proved the concept, and proved the use of a composite membrane to absorb solar energy where a hydrophillic membrane which absorbs solar radiation can be layered on top of a standard hydrophobic MD membrane. The experimental results generally agreed with the model, and demonstrated the importance of the novel element of absorbing solar energy at the membrane surface as opposed to an opaque absorber placed above the feed flow channel.

6.2.1 Challenges of Small-Scale Experiments

When the experiment is configured for using solar collection, a unique set of challenges arise. Since the system was designed to accept illumination from a solar simulator, which has a uniform input over a small area, the amount of energy collected by the device is limited. As a result mass flow rate must be lowered to increase the temperature rise, and resultant permeate flow rate. However, at low flow rates temperature polarization increases sharply, and the potential for high efficiency goes down, as shown with a scaling analysis in Chapter 4. Additionally low flow-rates are hard to maintain at a consistent operating condition. As flow rates increase, the low heat input quickly drives the temperature rise in the feed to close to zero, eliminating the potential for evaporation. Increasing the solar flux by moving the simulator aperture closer to the experiment results in high non-uniformity in solar irradiation.

However, in the acceptable operating range, the experimental results nominally match the model, and the model can be used to assess the performance of larger, production scale systems.

6.3 Future Work

While this thesis addresses important questions of energy efficiency in MD cycles, additional work should be done to improve the use of MD processes for desalination.

Questions of practical constructibility can be further investigated, particularly the effect of having a membrane that can intentionally stretch into the air gap under hydraulic pressure to decrease effective gap size and improve performance. Spacer designs optimized to take the greatest advantage of this effect without tearing the membrane could be developed. This could serve as a substitute for moderate pressure reduction in the gap, which would require additional expensive hardware.

Pilot plant design and testing of the solar direct-heated concept would provide additional energy efficiency data at the appropriate scale and better define the cost of a water from a production-scale system.

Further investigation into a pilot design and test of a multi-stage "MSF-type" VMD system would provide additional insight into the cost and scale of those systems as well.

Testing of the MD system with "challenge waters" or high-salinity, highly contaminated feeds would provide additional insight to niche applications for MD (such as a brine concentration step at the end of an reverse osmosis or multi-stage flash process, or use in treating water from unconventional oil and gas recovery). It would also provide insight into how energy efficiency performance degrades over time due to the scaling of the membrane or damage that leads to water breakthrough. Work with high salinity brines or brines at high temperatures would lead to a better understanding of the reliability of MD membranes in desalination, and help further assess the long term viability of MD as a production scale desalination process.

6.4 Contribution to Collaborative Works

The content of this thesis was used in collaborative works to model the performance of a solar-powered AGMD system as design parameters vary [20], to assess changes

in water cost as design parameters vary in DCMD, AGMD, and VMD systems [28], and to assess changes in system performance with varying membrane properties [58]. The model in Chapter 2 was used to evaluate the sources of irreversibility in a DCMD system [59].

Bibliography

[1] International Water Management Institute (Ed.), Water for Food, Water for Life: A Comprehensive Assessment of Water Management in Agriculture, Earthscan, London, 2006.

[2] T. Pankratz, IDA Desalination Yearbook 2012-2013, Media Analytics Ltd., Oxford, United Kingdom, 2012.

[3] M. Wilf, Membrane Desalination Technology, Balaban Desalination Publications, Hopkinton, MA, 2011.

[4] J. E. Miller, Review of Water Resources and Desalination Technologies, Technical Report SAND 2003-0800, Sandia National Laboratories, Albuquerque, NM, 2003.

[5] E. Guillen-Burrieza, J. Blanco, G. Zaragoza, D.-C. Alarcon, P. Palenzuela, M. Ibarra, W. Gernjak, Experimental analysis of an air gap membrane distillation solar desalination pilot system, Journal of Membrane Science 379 (2011) 386 – 396.

[6] H. E. Fath, S. M. Elsherbiny, A. A. Hassan, M. Rommel, M. Wieghaus, J. Koschikowski, M. Vatansever, PV and thermally driven small-scale, stand-alone solar desalination systems with very low maintenance needs, Desalination 225 (2008) 58 – 69.

[7] F. Banat, N. Jwaied, M. Rommel, J. Koschikowski, M. Wieghaus, Desalination by a "compact SMADES" autonomous solar-powered membrane distillation unit, Desalination 217 (2007) 29 – 37.

[8] K. W. Lawson, D. R. Lloyd, Membrane distillation, Journal of Membrane Science 124 (1997) 1 – 25.

[9] M. El-Bourawi, Z. Ding, R. Ma, M. Khayet, A framework for better understanding membrane distillation separation process, Journal of Membrane Science 285 (2006) 4 – 29.

[10] G. Zuo, R. Wang, R. Field, A. G. Fane, Energy efficiency evaluation and economic analyses of direct contact membrane distillation system using aspen plus, Desalination In Press, Corrected Proof (2011) –.

[11] H. Lee, F. He, L. Song, J. Gilron, K. K. Sirkar, Desalination with a cascade of cross-flow hollow fiber membrane distillation devices integrated with a heat exchanger, AIChE Journal 57 (2011) 1780–1795.

[12] G. Lange, G. van Gendt, F. Bollen, W. Heinzl, K. Zhao, T. G. Fane, Demonstrating solar-driven membrane distillation using Memsys vacuum-multi-effect-membrane distillation, in: Proceedings of the IDA World Congress on Desalination and Water Reuse, Perth, Australia, Sept. 5-9, 2011, International Desalination Association, Topsfield, MA, 2011.

[13] S. Cerneaux, I. Struzynska, W. M. Kujawski, M. Persin, A. Larbot, Comparison of various membrane distillation methods for desalination using hydrophobic ceramic membranes, Journal of Membrane Science 337 (2009) 55 – 60.

[14] A. Alklaibi, N. Lior, Transport analysis of air-gap membrane distillation, Journal of Membrane Science 255 (2005) 239 – 253.

[15] A. Alklaibi, N. Lior, Heat and mass transfer resistance analysis of membrane distillation, Journal of Membrane Science 282 (2006) 362 – 369.

[16] Z. Ding, L. Liu, Z. Li, R. Ma, Z. Yang, Experimental study of ammonia removal from water by membrane distillation (md): The comparison of three configurations, Journal of Membrane Science 286 (2006) 93 – 103.

[17] L. Martinez-Diez, M. I. Vazquez-Gonzalez, Temperature and concentration polarization in membrane distillation of aqueous salt solutions, Journal of Membrane Science 156 (1999) 265 – 273.

[18] S. Al-Obaidani, E. Curcio, F. Macedonio, G. D. Profio, H. Al-Hinai, E. Drioli, Potential of membrane distillation in seawater desalination: Thermal efficiency, sensitivity study and cost estimation, Journal of Membrane Science 323 (2008) 85 – 98.

[19] J. Rodriguez-Maroto, L. Martinez, Bulk and measured temperatures in direct contact membrane distillation, Journal of Membrane Science 250 (2005) 141 – 149.

[20] R. B. Saffarini, E. K. Summers, H. A. Arafat, J. H. Lienhard V, Technical evaluation of stand-alone solar powered membrane distillation systems, Desalination 286 (2011) 332–341. Submitted For Publication.

[21] B. Li, K. K. Sirkar, Novel membrane and device for vacuum membrane distillation-based desalination process, Journal of Membrane Science 257 (2005) 60 – 75.

[22] T. Y. Cath, V. D. Adams, A. E. Childress, Experimental study of desalination using direct contact membrane distillation: a new approach to flux enhancement, Journal of Membrane Science 228 (2004) 5 – 16.

[23] J. A. Duffie, W. A. Beckman, Solar Engineering of Thermal Processes, Wiley, Hoboken, NJ, 2006.

[24] M. Darwish, F. Al-Juwayhel, H. K. Abdulraheim, Multi-effect boiling systems from an energy viewpoint, Desalination 194 (2006) 22 – 39.

[25] A. Criscuoli, M. C. Carnevale, E. Drioli, Evaluation of energy requirements in membrane distillation, Chemical Engineering and Processing: Process Intensification 47 (2008) 1098 – 1105. Euromembrane 2006.

[26] X. Wang, L. Zhang, H. Yang, H. Chen, Feasibility research of potable water production via solar-heated hollow fiber membrane distillation system, Desalination 247 (2009) 403 – 411.

[27] S. Parekh, M. M. Farid, J. R. Selman, S. Al-hallaj, Solar desalination with a humidification-dehumidification technique — a comprehensive technical review, Desalination 160 (2004) 167–186.

[28] R. B. Saffarini, E. K. Summers, H. A. Arafat, J. H. Lienhard V, Economic evaluation of stand-alone solar powered membrane distillation systems, Desalination 299 (2012) 55–62. Accepted For Publication.

[29] W. A. Beckman, S. A. Klein, Engineering equation solver, Online., 2011.

[30] G. L. Liu, C. Zhu, C. S. Cheung, C. W. Leung, Theoretical and experimental studies on air gap membrane distillation, Heat and Mass Transfer 34 (1998) 329–335.

[31] A. S. Rattner, A. K. Nagavarapu, S. Garimella, T. F. Fuller, Modeling of a flat plate membrane-distillation system for liquid desiccant regeneration in air-conditioning applications, International Journal of Heat and Mass Transfer 54 (2011) 3650 – 3660.

[32] V. Bui, L. Vu, M. Nguyen, Modelling the simultaneous heat and mass transfer of direct contact membrane distillation in hollow fibre modules, Journal of Membrane Science 353 (2010) 85 – 93.

[33] J.-P. Mericq, S. Laborie, C. Cabassud, Vacuum membrane distillation for an integrated seawater desalination process, Desalination and Water Treatment 9 (2009) 287–296.

[34] M. Khayet, K. Khulbe, T. Matsuura, Characterization of membranes for membrane distillation by atomic force microscopy and estimation of their water vapor transfer coefficients in vacuum membrane distillation process, Journal of Membrane Science 238 (2004) 199 – 211.

[35] L. Martinez-Diez, F. J. Florido-Diaz, Desalination of brines by membrane distillation, Desalination 137 (2001) 267 – 273.

[36] M. I. Vazquez-Gonzalez, L. Martinez, Water distillation through poly(tetrafluoroethylene) hydrophobic membranes in a stirred cell, Journal of the Chemical Society, Faraday Transactions 90 (1994) 2043–2046.

[37] W. Wagner, A. Pruss, International equations for the saturation properties of ordinary water substance. revised according to the international temperature scale of 1990, Journal of Physical Chemistry Reference Data 22 (1993) 783–787.

[38] A. F. Mills, Heat and Mass Transfer, Irwin, Boston, MA, 1st edition, 1992.

[39] M. Sievers, Design and Optimization of a Dehumidier in a Humidication-Dehumidication (HDH) Desalination System, Master's thesis, Technische Universitat Hamburg-Harburg, 2010.

[40] J. H. Lienhard V, J. H. Lienhard IV, A Heat Transfer Textbook, Phlogiston Press, Cambridge, MA, 3rd edition, 2006.

[41] J. Koschikowski, M. Wieghaus, M. Rommel, Solar thermal-driven desalination plants based on membrane distillation, Desalination 156 (2003) 295 – 304. Joint EDS, WSTA and IWA conference on Desalination and the Environment Fresh Water for All UN International Year of Fresh Water 2003.

[42] J.-P. Mericq, S. Laborie, C. Cabassud, Vacuum membrane distillation of seawater reverse osmosis brines, Water Research 44 (2010) 5260–5273.

[43] M. H. Sharqawy, J. H. Lienhard V, S. M. Zubair, Thermophysical properties of seawater: A review of existing correlations and data, Desalination and Water Treatment 16 (2010) 354–380.

[44] M. Qtaishat, T. Matsuura, B. Kruczek, M. Khayet, Heat and mass transfer analysis in direct contact membrane distillation, Desalination 219 (2008) 272–292.

[45] N. Hengl, A. Mourgues, M. Belleville, D. Paolucci-Jeanjean, J. Sanchez, Membrane contactor with hydrophobic metallic membranes: 2. study of operating parameters in membrane evaporation, Journal of Membrane Science 355 (2010) 126 – 132.

[46] T.-C. Chen, C.-D. Ho, Immediate assisted solar direct contact membrane distillation in saline water desalination, Journal of Membrane Science 358 (2010) 122 – 130.

[47] E. K. Summers, J. H. Lienhard V, A novel solar-driven air gap membrane distillation system, Desalination and Water Treatment 51 (2013) 1344–1351.

[48] J. R. Howell, R. Siegel, M. P. Menguc, Thermal Radiation Heat Transfer, CRC Press, New York, fifth edition, 2011.

[49] Y. Touloukian, Y. Ho (Eds.), Thermophysical Properties of Matter, volume 8, Thermal Radiative Properties: Nonmetallic Solids, Plenum Press, New York, 1972.

[50] E. K. Summers, S. M. Zubair, J. H. Lienhard V, Air-heating solar collectors for humidication-dehumidication desalination systems, Journal of Solar Energy Engineering 133 (2011) 011016–1–6.

[51] Weather Underground, Weather History for Dhahran, Saudi Arabia, Online, 2011.

[52] E. K. Summers, H. A. Arafat, J. H. Lienhard V, Energy efficiency comparison of single-stage membrane distillation (MD) desalination cycles in different configurations, Desalination 290 (2012) 54–66.

[53] H. T. El-Dessouky, H. M. Ettouney, Y. Al-Roumi, Multi-stage flash desalination: present and future outlook, Chemical Engineering Journal 73 (1999) 173 – 190.

[54] T. Galal, A. Kalendar, A. Al-Saftawi, M. Zedan, Heat transfer performance of condenser tubes in an MSF desalination system, Journal of Mechanical Science and Technology 24 (2010) 2347–2355.

[55] M. Gryta, Desalination of thermally softened water by membrane distillation process, Desalination 257 (2010) 30 – 35.

[56] A. Cipollina, M. D. Sparti, A. Tamburini, G. Micale, Development of a membrane distillation module for solar energy seawater desalination, Chemical Engineering Research and Design 90 (2012) 21012121.

[57] Solar Rating and Certification Corporation, Directory of certified solar collector ratings, 2013.

[58] M. I. Ali, E. K. Summers, H. A. Arafat, J. H. Lienhard V, Effects of membrane properties on water production cost in small scale membrane distillation systems, Desalination 306 (2012) 60 – 71.

[59] K. H. Mistry, R. K. McGovern, G. P. Thiel, E. K. Summers, S. M. Zubair, J. H. Lienhard V, Entropy generation analysis of desalination technologies, Entropy 13 (2011) 1829–1864.